ALZHEIMER'S DISEASE DIAGNOSIS AND RISK PREDICTION USING ADVANCED MACHINE LEARNING MODELS

A Thesis Submitted to
UNIVERSITY OF CALICUT
in partial fulfilment of the requirements for the award of the degree of
DOCTOR OF PHILOSOPHY IN COMPUTER SCIENCE
Under the Faculty of Science

By

HAULATH K

Under the guidance of

Prof. (Dr.) MOHAMED BASHEER K.P
Principal and Professor,
Amal College of Advanced Studies, Nilambur

P.G & RESEARCH DEPARTMENT OF COMPUTER SCIENCE
Sullamussalam Science College, Areekode - 673639
(Affiliated to the University of Calicut)
Malappuram Dist., Kerala, India

OCTOBER 2025

DECLARATION

I, Haulath K, hereby declare that the work presented in the thesis entitled "**Alzheimer's Disease Diagnosis And Risk Prediction Using Advanced Machine Learning Models**" is based on the original work done by me under the guidance of **Prof. (Dr.) MOHAMED BASHEER K.P.**, Research Guide, PG & Research Department of Computer Science, Sullamussalam Science College, Areekode, Kerala, and has not been included in any other thesis submitted previously for the award of any degree. The contents of the thesis are undergone plagiarism check using iThenticate software at C.H.M.K. Library, University of Calicut, and the similarity index found within the permissible limit. I also declare that the thesis is free from AI generated contents.

Haulath K

Prof. (Dr.) MOHAMED BASHEER K.P
Research Guide
PG & Research Department of Computer Science
Sullamussalam Science College,
Areekode, Kerala, India

Areekode
Oct 2025

Prof. (Dr.) MOHAMED BASHEER K.P
PEN: 677975
Principal
Amal College of Advanced Studies
Eranhimangad P.O., Nilambur - 679329

SULLAMUSSALAM SCIENCE COLLEGE
AREACODE

Phone: 0483-2850700
Website: www.sscollege.ac.in
Email: mail@sscollege.ac.in

Aided College | Affiliated to the University of Calicut | Re-accredited by NAAC at A Grade

Ref:

Date:

CERTIFICATE

This is to certify that the thesis entitled **"Alzheimer's Disease Diagnosis And Risk Prediction Using Advanced Machine Learning Models"**, submitted to the University of Calicut, for the partial fulfillment of the requirements for the award of the degree of Doctor of Philosophy (Ph.D.) in Computer Science, is a bonafide research work done by Mrs. Haulath K under my supervision and guidance in the PG & Research Department of Computer Science, Sullamussalam Science College, Areekode, Malappuram, Kerala. The content embodied in this thesis, in full or in parts,has not been submitted to any other University or Institute for the award of any degree.

The thesis is revised as per the modifications and recommendations reported by the adjudicators. Soft copy attached is the same as that of the revised copy. The thesis is submitted as such to the University of Calicut with reference to the letter number No. 73907/RESEARCH-C-ASST-1/2025/Admn

Areekode
Oct 2025

Prof. (Dr.) Mohamed Basheer K.P
Research Guide
PG & Research Department of Computer Science
Sullamussalam Science College,
Areekode, Kerala, India

Prof. (Dr.) MOHAMED BASHEER K.P
PEN: 677975
Principal
Amal College of Advanced Studies
Eranhimangad P.O., Nilambur - 679329

ACKNOWLEDGMENTS

It is my great pleasure to acknowledge all those who have helped me with the successful completion of my research work

First and foremost, I thank **Lord Almighty** who blessed me to with this opportunity and blessed me with health, confidence and strength to complete my study successfully.

First and foremost, I express my deepest gratitude to my advisor Prof. (Dr.) Mohamed Basheer K.P, Research Guide in the P.G and Research Department of Computer Science at Sullamussalam Science College, Areekode whose unwavering support, guidance, and scholarly insights have been instrumental in shaping the direction of my research. Your mentorship has been invaluable, and I am truly fortunate to have had the privilege of working under your supervision. Dr. Basheer emerged not only as a mentor but as a beacon of support, the epitome of positivity, and a friendly guide whose confidence in my research pursuits infused me with a deep sense of assurance. His meticulous, thorough reviews were not just constructive but immensely contributive, shaping not only the research papers but also sculpting the very fabric of this comprehensive thesis. The profound understanding, inexhaustible patience, boundless kindness, and the freedom to explore under his mentorship transformed my research tenure into an indelibly memorable and intellectually enriching experience. Without his support, encouragement, moral and mental support the successful completion of my work would not be possible.

I extend my deepest gratitude to Dr. Muhamed Ilyas P, our esteemed principal, whose unwavering support, and encouragement have been the cornerstone of my academic journey. His visionary leadership has created a culture of academic excellence within our institution, inspiring me to strive for the highest standards in my pursuit of knowledge.

I extend my profound gratitude to the esteemed members of my research advisory committee for their invaluable contributions to my Ph.D. journey. Dr. Lajish VL, Associate Professor & Head, Dept. of Computer Science, University of Calicut, Dr. Shameem Kappan, Head, PG & Research Department of Computer Science, SS

College, Areekode for their thoughtful insights and constructive critiques. I recognize the profound impact they have had on my academic and intellectual development. Their contributions have been invaluable, and I am truly grateful for the privilege of having them as members of my research advisory committee.

I extend my heartfelt gratitude to my husband, Yoosuf K., for his invaluable collaboration throughout the course of this research endeavor. I am deeply thankful for his commitment to excellence and the positive impact he has had on this academic journey.

I extend my heartfelt gratitude to my beloved son, Muhammed Haani Nabhan, whose unwavering support and motivation have been a guiding light throughout my research journey. His encouragement has instilled in me the drive to persevere, even during the most challenging times. I also wish to thank my younger daughter, Aamilah Isha Hanan, whose delightful naughtiness and infectious laughter have brought moments of joy and relaxation, helping me maintain balance amidst the demands of this work

A special acknowledgment goes to my brother, Dr. Noufal Kandoth, Pool Scientist at IISER Kolkata and Marie Curie Fellow, whose guidance and inspiration have played a pivotal role in shaping my research path. My sincere thanks to my sister, Saleekath K, whose comforting presence has been a source of relief during difficult moments, always offering a listening ear. I am also grateful to my sister-in-law, Dr. Rositha Kuniyil, Assistant Professor at IIT Palakkad, for her encouragement and valuable insights along the way.

I extend my sincere gratitude to all my research colleagues and friends in my department and non-teaching staff and lab assistants for their support and help.

Finally, I would like to thank all my teachers, friends, cousins and well-wishers who have helped me throughout the course of my work.

Haulath K

Dedicated

To My Ever-Loving Father

&

My Ever-Loving Mother

[For their Unconditional Love, Support, Motivation, Endless Sacrifices, Understanding, and Resilience that have Shaped the Person I am Today.]

ABSTRACT

Alzheimer's Disease (AD), which impairs memory, cognition, and behavior, is a progressive Neurodegenerative Disorder (ND). Accounting for 60-80% of dementia cases, AD advances from mild memory loss to complete loss of interaction with the environment. As there is no cure for AD, early detection is vital to mitigate disease progression. Currently, Machine Learning (ML) and Deep Learning (DL) have exhibited promise in neuroimaging-based AD prediction by employing approaches, namely Lasso Regression (LR), Convolutional Neural Networks (CNN), Support Vector Machine (SVM), and Deep Neural Networks (DNN). Nevertheless, these models face limitations, comprising overfitting, high error rates, and limited small dataset performance.

To address these challenges, a two-part framework is introduced in this study. The AD Neuroimaging Initiative (ADNI) MRI dataset is used by the first implementation to enhance prediction and classification accuracy through the GELU Swish Radial Basis Function Network (GS-RBFN). MRI images undergo preprocessing steps, such as normalization, skull stripping, and spatial smoothing, followed by essential brain tissue segmentation with Brownian Log Scaling Archimedes Optimization-centric Watershed Segmentation (BLSAOWS) and Feature Selection (FS) using the Base Switch Rule Infimum and Supremum-based Rock Hyrax Swarm Optimization (BSRISRHSO) approach. AD classification is further performed by the GS-RBFN classifier. GS-RBFN (Gaussian–Swish Radial Basis Function Network) and TT Self-Weighted Deep-AD3-Net—for early detection and staging of AD. The proposed models employ novel optimization algorithms (BLSAOWS and BSRISRHSO) for improved segmentation and feature selection from MRI datasets.

The performance analysis of GS-RBFN model learns the features efficiently, it achieves superior accuracy (98.45%), precision (98.44%), F-measure (98.44%), Sensitivity (98.44%), Recall (98.45%), and specificity (98.45%).

In the second implementation, AD risk scoring and stage prediction are focused on using The AD Prediction Of Longitudinal Evolution (TADPOLE) dataset. This methodology involves ranking critical variables, Risk Score (RS) calculation, and brain shrinkage analysis. Essential variables are selected by the Recursive Hypothesis-Creation Algorithm (RHCA), with the True True Self-Weighting

Mechanism (TT-SWM) calculating RS. By using the Queue-Boltzmann-Constant-Sphere (QBCS) technique, brain shrinkage in the hippocampus is measured, whereas Gray-Level Co-occurrence Matrix (GLCM) features facilitate staging through the Deep-AD3-Net classifier. Experimental evaluation using the TADPOLE dataset achieved an accuracy of 98.45%, sensitivity of 97.82%, and AUC of 0.981, outperforming recent state-of-the-art models.

The frameworks demonstrate robustness and clinical potential for early intervention and treatment planning. The study advances existing AD diagnostic approaches by improving interpretability, computational efficiency, and predictive reliability.

Keywords: Alzheimer's disease, Data augmentation, Brownian Log Scaling Archimedes Optimization-based Watershed Segmentation (BLSAOWS), Base Switch Rule Infmum and Supremum-based Rock Hyrax Swarm Optimization (BSRISRHSO), GELU and SWISH-based Radial Basis Function Network (GS-RBFN), Recursive Hypothesis-Creation Algorithm (RHCA), Phylogenetic Method (PM), one Gray-Level Co-occurrence Matrix (GLCM), Gray-Level Co-occurrence Matrix (GLCM Genetic Algorithm (GA), Deep-AD3-Net classifier.

സംഗ്രഹം

ഓർമശക്തി, അറിവ്, പെരുമാറ്റം എന്നിവയെ തകരാറിലാക്കുന്ന അൽഷിമേഴ്സ് രോഗം (എഡി) ഒരു പുരോഗമന ന്യൂറോ ഡിജനറേറ്റീവ് ഡിസോർഡർ (എൻഡി) ആണ്. 60-80% ഡിമെൻഷ്യ കേസുകൾ കണക്കിലെടുക്കുമ്പോൾ, എഡി നേരിയ മെമ്മറി നഷ്ടത്തിൽ നിന്ന് പരിസ്ഥിതിയുമായുള്ള ഇടപെടൽ പൂർണ്ണമായ നഷ്ടത്തിലേക്ക് മുന്നേറുന്നു. എഡിക്ക് ചികിത്സയില്ലാത്തതിനാൽ, രോഗത്തിൻ്റെ പുരോഗതി ലഘൂകരിക്കുന്നതിന് നേരത്തെയുള്ള കണ്ടെത്തൽ അത്യന്താപേക്ഷിതമാണ്. നിലവിൽ, മെഷീൻ ലേണിംഗും (എംഎൽ) ഡീപ്പ് ലേണിംഗും (ഡിഎൽ) ന്യൂറോ ഇമേജിംഗ് അടിസ്ഥാനമാക്കിയുള്ള എഡി പ്രവചനത്തിൽ ലാസ്സോ റിഗ്രെസിയോ എന്ന സമീപനത്തിലൂടെ വാഗ്ദാനങ്ങൾ പ്രദർശിപ്പിച്ചിട്ടുണ്ട്.

ഈ വെല്ലുവിളികളെ നേരിടാൻ, ഈ പഠനത്തിൽ രണ്ട് ഭാഗങ്ങളുള്ള ചട്ടക്കൂട് അവതരിപ്പിക്കുന്നു. GELU സ്പിഷ് റേഡിയൽ ബേസിസ് ഫംഗ്ഷൻ നെറ്റ്വർക്ക് (GS-RBFN) മുഖേന പ്രവചനവും വർഗ്ഗീകരണ കൃത്യതയും വർദ്ധിപ്പിക്കുന്നതിന് AD ന്യൂറോഇമേജിംഗ് ഇനിഷ്യേറ്റീവ് (ADNI) MRI ഡാറ്റാസെറ്റ് ആദ്യമായി നടപ്പിലാക്കുന്നു. എംആർഐ ചിത്രങ്ങൾ നോർമലൈസേഷൻ, തലയോട്ടി നീക്കം ചെയ്യൽ, സ്പേഷ്യൽ മിനുസപ്പെടുത്തൽ തുടങ്ങിയ പ്രീപ്രോസസിംഗ് ഘട്ടങ്ങൾക്ക് വിധേയമാകുന്നു, തുടർന്ന് ബ്രൗണിയൻ ലോഗ് സ്കെയിലിംഗ് ആർക്കിമിഡീസ് ഒപ്റ്റിമൈസേഷൻ കേന്ദ്രീകൃത വാട്ടർഷെഡ് സെ ഉപയോഗിച്ച് അത്യാവശ്യ മസ്തിഷ്ക കോശ വിഭജനം നടത്തുന്നു.

രണ്ടാം നടപ്പാക്കലിൽ, AD (Alzheimer's Disease) അപകടസാധ്യതാ സ്കോറിംഗ് ഘട്ട പ്രവചനം TADPOLE (The AD Prediction Of Longitudinal Evolution) ഡാറ്റസെറ്റ് ഉപയോഗിച്ചാണ് കേന്ദ്രീകരിക്കുന്നത്. ഈ രീതിയിൽ പ്രധാന ഘടകങ്ങളെ റാങ്ക് ചെയ്യുക, റിസ്ക് സ്കോർ കണക്കാക്കുക, ബ്രെയിൻ ശ്രിങ്കേജിനെ വിശകലനം ചെയ്യുക എന്നിവ ഉൾപ്പെടുന്നു. പ്രധാന ഘടകങ്ങൾ Recursive Hypothesis-Creation Algorithm (RHCA) ഉപയോഗിച്ച് തിരഞ്ഞെടുക്കപ്പെടുന്നു, True True Self-Weighting Mechanism (TT-SWM) റിസ്ക് സ്കോർ കണക്കാക്കുന്നു. Queue-Boltzmann-Constant-Sphere (QBCS) സാങ്കേതിക വിദ്യ ഉപയോഗിച്ച് ഹിപ്പോകാംപസിലെ ബ്രെയിൻ ശ്രിങ്കേജം അളക്കുമ്പോൾ, Gray-Level Co-occurrence Matrix (GLCM) ഫീച്ചറുകൾ Deep-AD3-Net ക്ലാസിഫയർ ഉപയോഗിച്ച് ഘട്ടനിർണയം സുഗമമാക്കുന്നു.

സൂചകപദങ്ങൾ: അൽഷിമേഴ്സ് രോഗം • ഡാറ്റാ വർദ്ധനവ് • ബ്രൗണിയൻ ലോഗ് സ്കെയിലിംഗ് ആർക്കിമിഡീസ് ഒപ്റ്റിമൈസേഷൻ അടിസ്ഥാനമാക്കിയുള്ള വാട്ടർഷെഡ് സെഗ്മെന്റേഷൻ (BLSAOWS) • ബേസ് സ്വിച്ച് റൂൾ ഇൻഫ്ലം ആൻഡ് സുപ്രീമം അടിസ്ഥാനമാക്കിയുള്ള റോക്ക് ഹൈറാക്സ് സ്വാം ഒപ്റ്റിമൈസേഷൻ (BSRISRHSO) • GELU, SWISH അടിസ്ഥാനമാക്കിയുള്ള റേഡിയൽ ബേസിസ് ഫംഗ്ഷൻ നെറ്റ്വർക്ക് (GS-RBFN), റിക്കർസീവ് ഹൈപ്പോതെസിസ്-ക്രിയേഷൻ അൽഗോരിതം (RHCA), ഫൈലോജെനെറ്റിക് രീതി (PM), ഗ്രേ-ലെവൽ കോ-ഒക്കുറൻസ് മാട്രിക്സ് (GLCM), ജനിതക അൽഗോരിതം (GA), ഡീപ്-AD3-നെറ്റ് ക്ലാസിഫയർ.

CONTENTS

LIST OF TABLES

LIST OF FIGURES

LIST OF SYMBOLS AND ABBREVIATIONS

$\Im^{MRI}{}_{N}$	:	Collected brain MRI images
n	:	Total number of collected MRI images
v	:	Total number of intensity values
τ^{th}	:	Threshold value
T	:	Total number of threshold values
$\partial^{nor}\left(\xi^{I}\right)$	:	Normalized intensity value
$\Re^{MRI}$	:	Re-constructed brain MRI images
R	:	Total number of reconstructed MRI brain images
σ^{bf}	:	Bias field across the original and reconstructed image
$\aleph^{N3}$	:	Normalized MRI brain images after intensity normalization
$A\left(\aleph^{N3}\right)_{p,q}$	:	Array matrix of a normalized image
$\delta^{tm}{}_{\max}$	:	Calculated tournament maximum values
$\delta^{tm}{}_{\min}$	:	Calculated tournament minimum values
μ^{tm}	:	Mean value of the tournament maximum and minimum values
$\left(\delta^{\aleph}\right)$	:	Skull-stripped images
S	:	Total number of skull-stripped MRI brain images
ζ^{PP}	:	Pre-processed image MRI brain images
$Gr(a,b)$	:	The gradients of the pixel coordinates
$\wp_{low}$	:	Lower bound of the search space
$\wp_{upp}$	:	Upper bound of the search space
d	:	D dimensional vector
ς_{den}	:	Density of the population
ς_{vol}	:	Volume of the population
ξ^{fit}	:	Fitness
Y_{seg}	:	Segmentation efficiency
υ^{ran}	:	Randomly selected numbers
con_1 and con_2	:	Constants
B_{t}^{mot}	:	Brownian motion

$i_{\max}$	:	Maximum iteration
$\aleph^{TF}$	:	Transfer operator
$\varsigma_{acc}^{j}[i+1]$	:	Updated acceleration of an object
ς_{den}^{ran}	:	Random material of density
ς_{vol}^{ran}	:	Random material of volume
ς_{acc}^{ran}	:	Random material of acceleration
ς_{den}^{BEST}	:	Best density of an object
ς_{vol}^{BEST}	:	Best volume of an object
ς_{acc}^{BEST}	:	Best acceleration of an object
$\Im\varsigma_{acc}^{j}[i+1]$	:	Normalized acceleration of an object
$\max\lvert\varsigma_{acc}\rvert$	:	Maximum acceleration
$\min\lvert\varsigma_{acc}\rvert$	:	Minimum acceleration
$IP^{j}[i]$	:	Individual position
con_3	:	Constant value
IP_{ran}	:	Random material of an object
Γ_{fdm}	:	Flag for changing the direction of motion
τ^{th}	:	Threshold value
M^{mar}	:	Marker
N^{M}	:	Total number of selected markers
$\Re_{reg}$	:	Regional marker
r^{r}	:	Maximum number of regional markers
$\varphi^{dis}\left[\mathrm{M}_{n^m}^{mar},\ \Re_{reg}^{r^r}\right]$	:	Distance between the selected maximum markers and the regional markers
X^{ζ}	:	Segmented image
s^{s}	:	Total number of segmented images
Θ^{DO}	:	Dilation operation
ϑ_{SE}	:	Structuring element
po	:	Points
Θ^{EO}	:	Erosion
Θ^{OO}	:	Opening operation
Θ^{CO}	:	Closing operation

$\chi_{X^{\zeta}}$: Final enhanced segmented images

EE : Maximum number of enhanced segmented images

$\partial^{\chi_{X^{\zeta}}}$: Rotated image

$\ell^{\chi_{X^{\zeta}}}$: Final flipped image

h : Horizontal flipping operations

v : Vertical flipping operation

$\hbar^{\chi_{X^{\zeta}}}$: Deformed images

υ_{dcp} : Displaced control points

υ_{INT} : Interpolation technique

$\delta^{\chi_{X^{\zeta}}}$: Scaled images

$\varepsilon^{\chi_{X^{\zeta}}}$: Cropped image

A^{χ_X} : Final augmented images

γ_{afp} : Extracted feature patches

υ_1, υ_2 and υ_3 : Anatomical landmarks

$P^{PCC}\left[\gamma_{afp}^{1}, \gamma_{afp}^{2}\right]$: Pearson correlation between the feature patches

ϖ^{cov} : Covariance

σ^{sd} : Standard deviation

λ_{FP} : Concatenated feature patches

F_f : Total number of feature patches

$P_O\left|\lambda_{FP}\right|$: Population of the feature patches or the Rock Hyrax

Ψ^{FF} : Fitness function

τ_{CA} : Classification accuracy

O^{tot} : Total number of observations

$\hat{\lambda}_{\aleph}$: Current position of the leader

ran : Random number

τ_{CA}^{mem+1} : Updated position of every member of the rock hyrax group

τ_{CA}^{mem} : Current position of every member of the rock hyrax group

Δ^{CM} : Circular movement of the population

ran_r : Radius of the circular portion

Ξ_{low} : Lower bound of the variables

Ξ_{upp}	:	Upper bound of the variables
NL and MU	:	Maximum number of low bound variables and upper bound variables
${}^{s}\Xi_{low}$	:	Selected lower bound from the set of variables
${}^{s}\Xi_{upp}$	:	Selected upper bound variable from the set of upper bound variables by using the supremum
φ_{+1}	:	Updated position of the angle
ξ_{Ψ}	:	Selected or extracted best features
B^{F}	:	Maximum number of extracted features for the accurate classification of AD
Ω_{IL}	:	Input layer
Ω_{HL}	:	Hidden layer
Φ^{GELU}	:	GELU activation function
Φ^{SWISH}	:	SWISH activation function
K	:	Learnable parameter
Ω_{HL}^{out}	:	Output obtained from the hidden layer
ω	:	Weight values
O_{values}	:	Output values
Ω_{OL}^{out}	:	Classified output of the output layer
∂^{ATD}	:	Data from the given ADNI TADPOLE dataset
A	:	Maximum number of data
ℓ_{var}	:	Extracted variable
B	:	Maximum number of extracted variables
$\wp^{\ell_{\text{var}}}$	:	Noise-removed variables for the accurate evaluation of risk scores
C	:	Maximum number of noise-removed variables
σ^{cov}	:	Covariance of two variables
ω^{sd}	:	Standard deviation of two variables
ℓ^{re}	:	Calculated relationships
atr_1 and atr_2	:	Required strong attributes
H^{0} and $H^{\propto}$	:	Null and alternative hypothesis
$\sigma^{VAR}(wg)$	:	Within-group variance
$\sigma^{VAR}(bg)$	:	Between-group variance

ζ_{PV}	:	Prediction value using a statistical test
ζ_{low}^{PV}	:	Low prediction value
ζ_{high}^{PV}	:	High prediction value
ζ^{CM}	:	Correlation matrix
$\hbar_{SV}$	:	Selected variables
D	:	Maximum number of selected variables
M^{mc}	:	Markov chain
P_{INI}	:	Initial probability distribution matrix
int	:	Maximum number of probability distribution elements
λ^{RV}	:	Ranked variables
E	:	Maximum number of ranked variables
g	:	Number of chromosomes or ranked features
Γ_{fit}	:	Fitness function
P^{s}	:	Selection probability
ω_{wf}	:	Weight factor
g^{g}	:	Chromosome pair
ξ	:	Selection process
$\min\left\|\Gamma_{fit}\left(\lambda^{RV}\right)\right\|$	:	Minimum probability of selection
g_{sle}	:	Selected chromosomes
G^{G}	:	Maximum number of selected chromosomes
ξ^{new}	:	New string
ς_{CO}	:	Crossover operator
ς_{Mop}	:	Mutation producer
ϑ_{EF}	:	Extracted features
H	:	Maximum number of extracted features
ω^{WAF_I}	:	Weight-assigned features
ω_{WV}	:	Weight values
F_I	:	Maximum number of features from the given dataset
σ^{SD}	:	Standard deviation
μ_{mean}	:	Weighted mean value

$\wp^{Z-S}$	:	Z-score
m	:	Maximum number of the features from the given dataset
η_{AS}	:	Selected features
N	:	Maximum number of selected features for the accurate risk score prediction of AD
Y_{VWV}	:	Assigned ventricle volume weight
$\Re^{PR}$	:	Predicted score
ω^{other}	:	Weight values
t	:	Time
den	:	Density
S	:	Strength
f^{pre}	:	Fluid pressure
υ^{qbc}	:	Queue absorption coefficient
λ^{wl}	:	Wavelength
E_{RDE}	:	Rosseland diffusion approximation
B_{con}	:	Boltzmann constant
β^{FC}	:	The local skin friction coefficient
β^{NUS}	:	Nusselt
β^{SHE}	:	Sherwood number
$\aleph_{RN}$	:	Reynolds number
$\Re_{SF}$	:	Shear factor
$\Re^{BSF}$	:	Calculated brain shrinkage
τ_{int}	:	Total hours of internal shrinkage
τ_{ext}	:	Total hours of external shrinkage
T	:	Available hours
χ^{PWD}	:	Pairwise distance between the neurons
$\propto$	:	Neurons present in the brain
M_{dist}	:	Distance matrix
ε_{RFM}	:	Radiomic feature measur
$tree$	:	Constructed tree
p_p	:	Maximum number of evaluated radiomic feature measurements

Q	:	Maximum number of obtained bilateral hippocampus features through the construction of GLCM
∂^{BFE}	:	Extracted features
R	:	Maximum number of extracted features
ϑ_{EF}	:	Ranking phase
∂^{BFE}	:	Brain shrinkage measurement phase
$\Im_{\vartheta\partial\Re}$	:	Features
Ψ_{atten}	:	Attention layer
θ^{acc}	:	Accuracy
φ_{Ct}	:	Computation time of each feature
Ψ_{extra}	:	Extraction layer
δ^{ARF}	:	Extracted area-related features
Ψ_{Pheno}	:	Phenotype-assistant layer
∞^{VD}	:	Volume of data with microstructure-oriented results
Ω^{IN}	:	Input layer
ω^{weight}	:	Weights
σ^{bias}	:	Biases of the neurons in the input layer
Ψ_{AD_3}	:	Output of the AD_3 layer
$\Omega^{\mathrm{Re}LU}$	:	Output of the relu activation function layer
$\Phi_{\mathrm{Re}LU}$	:	Relu activation function
Ω^{CON}	:	Output of the convolutional layer
ω_{CON}^{weight}	:	Weight values of the convolutional layer
σ_{CON}^{bias}	:	Bias values of the convolutional layer
X_{fil}	:	Filters
Ω^{POO}	:	Output of the pooling layer
$\xi\kappa^{DR}$	:	Dimensionality reduced data
Ω^{FCL}	:	Output of the fully connected layer
ω_{FCL}^{weight}	:	Weight values of the fully connected layer
σ_{FCL}^{bias}	:	Bias values of the fully connected layer
Ω^{MSE}	:	Mean square error
Ξ^{AO}	:	Actual output
Ω^{OUT}	:	Output layer
∂_{Ψ}	:	Collected time series-based f-MRI images from the ADNI dataset

A^a	:	Maximum number of collected time series-based fmri images
MC	:	Motion correction operation
ℓ_Ψ	:	Motion-corrected images
AD	:	Alzheimer's disease
2D	:	Two-Dimensional
3D	:	Three-Dimensional
ABIDE	:	Autism Brain Image Data Exchange
ADAS-Cog	:	Alzheimer's Disease Assessment Scale Cognitive Subscale
ADDTLA	:	Alzheimer's Disease Detection empowered with Transfer Learning Algorithm
ADNI	:	Alzheimer's Disease Neuroimaging Initiative
ADPM	:	AD Prediction Model
ADReSS	:	Alzheimer's Dementia Recognition through Spontaneous Speech
AI	:	Artificial Intelligence
AIBL	:	ADNI and Australian Imaging, Biomarker and Lifestyle Flagship Study of Ageing
ANN	:	Artificial Neural Network
AOA	:	Archimedes Optimization Algorithm
ASD	:	Autism Spectrum Disorder
AUC	:	Area Under Curve
BiLSTM	:	Bidirectional LSTM
BLSAOWS	:	Brownian Log Scaling Archimedes Optimization-based Watershed Segmentation
BOA	:	Butterfly Optimization Algorithm
BSRIS	:	Base Switch Rule Infimum and Supremum
BSRISRHSO	:	Base Switch Rule Infimum and Supremum based Rock Hyrax Swarm Optimization
CAE	:	Convolutional Auto Encoder
CN	:	Control Normal
CNN	:	Convolutional Neural Network
COA	:	Coyote Optimization Algorithm
CSF	:	Cerebro Spinal Fluid
CT	:	Computed Tomography
DA-MIDL	:	Dual Attention Multi-Instance Deep Learning Network
DBN	:	Deep Belief Network
DCA	:	Discriminant Correlation Analysis

DL	:	Deep Learning
DNA	:	Deoxyribonucleic Acid
DNN	:	Deep Neural Networks
DPM	:	Disease Progression Modeling
DRIAD	:	Drug Repurposing In AD
DT	:	Decision Tree
DTI	:	Diffusion Tensor Imaging
EL	:	Ensemble Learning
EMCI	:	Early Mild Cognitive Impairment
EPO	:	Emperor Penguin Optimizer
FCL	:	Fully Connected Layer
FDG-PET	:	Fluorodeoxyglucose Positron Emission Tomography
FSO	:	Firebug Swarm Optimization
GA	:	Genetic Algorithm
GCN	:	Graph Convolutional Network
GLCM	:	Gray-Level Co-occurrence Matrix
GM	:	Grey Matter
GOA	:	Grasshopper Optimization Algorithm
GRU	:	Gated Recurrent Units
GS-RBFNs	:	GELU Swish Radial Basis Function Networks
HC	:	Healthy Control
H-FCN	:	Hierarchical Fully Convolutional Network
HHO	:	Harris Hawks Optimization
ICV	:	Intracranial Volume
kNN	:	k-Nearest Neighbor
LESSO	:	Least Absolute Shrinkage and Selection Operator
LMCI	:	Late MCI
LR	:	Lasso Regression
LRP	:	Layer-Wise Relevance Propagation
LSTM	:	Long Short Term Memory
LSTSVM	:	Least Squares TSVM
MAE	:	Mean Absolute Error
MAPE	:	Mean Absolute Percentage Error
MCI	:	Mild Cognitive Impairment
MITs	:	Medical imaging techniques
ML	:	Machine Learning

MMSE	:	Mini-Mental State Exam
MRI	:	Magnetic Resonance Imaging
MRMR	:	Minimal Redundancy Maximal Relevance
MTDL	:	Multi-Task Deep Learning
N3	:	Nonparametric Non-uniform intensity Normalization
NC	:	Normal Control
NCA	:	Neighborhood Component Analysis
ND	:	Normal Dementia
NINCDS	:	National Institute of Neurological and Communicative Disorders and Stroke
NN	:	Neural Network
OASIS	:	Open Access Series of Imaging Studies
OT	:	Otsu Threshold
PCA	:	Principal Component Analysis
PET	:	Positron Emission Tomography
PM	:	Phylogenetic Method
PSNR	:	Peak Signal-to-Noise Ratio
QBCS	:	Queue-Boltsman-Constant-Sphere
RBFNs	:	Radial Basis Function Networks
RCAB	:	Residual Channel Attention Blocks
RELSTSVM	:	Robust Energy-based LS-TSVM
RF	:	Random Forest
RFE	:	Recursive Feature Elimination
RGS	:	Region Growing Segmentation
RHCA	:	Recursive Hypothesis-Creation Algorithm
RHSO	:	Rock Hyrax Swarm Optimization
RHSW	:	Rock Hyraxes Swarm Optimization
RMSE	:	Root Mean Squared Error
RNN	:	Recurrent Neural Network
ROI	:	Region Of Interest
rs-fMRI	:	resting-state functional Magnetic Resonance Imaging
SCNN	:	Siamese Convolutional Neural Network
SFC	:	Sequential Feature Collection
SMC	:	Significant Memory Concern
SMRI	:	Structural MRI
SPECT	:	Single Photon Emission Computed Tomography
SSIM	:	Structural Similarity Index

SVM	:	Support Vector Machine
SVM-RFE	:	SVM-based Recursive Feature Elimination
SWM	:	Self-Weighting Mechanism
TADPOLE	:	The Alzheimer's Disease Prediction Of Longitudinal Evolution
TCN	:	Temporal Convolutional Network
TGT	:	Tournament Global Thresholding
TL	:	Transfer Learning
TMTL-GB	:	Tensor Multi-Task ensemble learning with Gradient Boosting
TSVM	:	Twin Support Vector Machine
TT	:	True True
TT-SWM	:	True True Self-Weighting Mechanism
VGG	:	Visual Geometry Group
WM	:	White Matter
WOA	:	Whale Optimization Algorithm
WSA	:	Watershed Segmentation Algorithm

UNIVERSITY OF CALICUT

CERTIFICATE ON PLAGIARISM CHECK

1.	Name of the Research Scholar	HAULATH K	
2.	Title of thesis / dissertation	ALZHEIMER'S DISEASE DIAGNOSIS AND RISK PREDICTION USING ADVANCED MACHINE LEARNING MODELS	
3.	Name of the Supervisor	PROF. (DR.) MOHAMED BASHEER K.P	
4.	Department/Institution	PG& RESEARCH DEPARTMENT OF COMPUTER SCIENCE, SULLAMUSSALAM SCIENCE COLLEGE, AREEKODE,673639	
5.	Similar content (%) identified	Non Core **Introduction/ Theoretical overview/Review of literature/ Materials & Methods/ Methodology**	Core **Analysis/Result/Discussion/ Summary/Conclusion/ Recommendations**
		2	1
	Acceptable maximum limit (%)	10	10
6.	Software used	Ithenticate	
7.	Date of verification	10.03.25	

**Report on plagiarism check, specifying included/excluded items with % of similarity to beattached.*

Checked by (with name , designation & signature) Dr. Nasirudheen. T Assistant Librarian University of Calicut, Kerala

Name and signature of the Researcher HAULATH · K

Name and signature of the Supervisor Prof. (Dr.) MOHAMED BASHEER K.P PEN: 677975 Principal Amal College of Advanced Studies Nilambur-679329

The Doctoral Committee* has verified the report on plagiarism check with the contents of the thesis, as summarized above and appropriate measures have been taken to ensure originality of the Research accomplished herein.

Name & Signature of the HoD/HoI (Chairperson of the Doctoral Committee) Dr.MUHAMED ILYAS.P PRINCIPAL SULLAMUSSALAM SCIENCE COLLEGE AREEKODE,UGRAPURAM (PO) MALAPPURAM(Dt),Pin-673639

**In case of languages like Malayalam, Tamil etc..on which no software is available for plagiarismcheck, a manual check shall be made by the Doctoral Committee, for which an additional certificate has to be attached.*

Haulath K. Alzheimer's disease diagnosis and risk prediction using advanced machine learning models. Thesis.2025. Sullamussalam Science College, University of Calicut.

CONTENTS

ABSTRACT

Alzheimer's Disease (AD), which impairs memory, cognition, and behavior, is a progressive Neurodegenerative Disorder (ND). Accounting for 60-80% of dementia cases, AD advances from mild memory loss to complete loss of interaction with the environment. As there is no cure for AD, early detection is vital to mitigate disease progression. Currently, Machine Learning (ML) and Deep Learning (DL) have exhibited promise in neuroimaging-based AD prediction by employing approaches, namely Lasso Regression (LR), Convolutional Neural Networks (CNN), Support Vector Machine (SVM), and Deep Neural Networks (DNN). Nevertheless, these models face limitations, comprising overfitting, high error rates, and limited small dataset performance.

To address these challenges, a two-part framework is introduced in this study. The AD Neuroimaging Initiative (ADNI) MRI dataset is used by the first implementation to enhance prediction and classification accuracy through the GELU Swish Radial Basis Function Network (GS-RBFN). MRI images undergo preprocessing steps, such as normalization, skull stripping, and spatial smoothing, followed by essential brain tissue segmentation with Brownian Log Scaling Archimedes Optimization-centric Watershed Segmentation (BLSAOWS) and Feature Selection (FS) using the Base Switch Rule Infimum and Supremum-based Rock Hyrax Swarm Optimization (BSRISRHSO) approach. AD classification is further performed by the GS-RBFN classifier. GS-RBFN (Gaussian–Swish Radial Basis Function Network) and TT Self-Weighted Deep-AD3-Net—for early detection and staging of AD. The proposed models employ novel optimization algorithms (BLSAOWS and BSRISRHSO) for improved segmentation and feature selection from MRI datasets.

The performance analysis of GS-RBFN model learns the features efficiently, it achieves superior accuracy (98.45%), precision (98.44%), F-measure (98.44%), Sensitivity (98.44%), Recall (98.45%), and specificity (98.45%).

Prof. (Dr.) MOHAMED BASHEER K.P
PEN: 677975
Principal
Amal College of Advanced Studies
Eranhimangad P.O., Nilambur - 679329

Haulath K. Alzheimer's disease diagnosis and risk prediction using advanced machine learning models. Thesis.2025. Sullamussalam Science College, University of Calicut.

In the second implementation, AD risk scoring and stage prediction are focused on using The AD Prediction Of Longitudinal Evolution (TADPOLE) dataset. This methodology involves ranking critical variables, Risk Score (RS) calculation, and brain shrinkage analysis. Essential variables are selected by the Recursive Hypothesis-Creation Algorithm (RHCA), with the True True Self-Weighting Mechanism (TT-SWM) calculating RS. By using the Queue-Boltzmann-Constant-Sphere (QBCS) technique, brain shrinkage in the hippocampus is measured, whereas Gray-Level Co-occurrence Matrix (GLCM) features facilitate staging through the Deep-AD3-Net classifier. Experimental evaluation using the TADPOLE dataset achieved an accuracy of 98.45%, sensitivity of 97.82%, and AUC of 0.981, outperforming recent state-of-the-art models.

The frameworks demonstrate robustness and clinical potential for early intervention and treatment planning. The study advances existing AD diagnostic approaches by improving interpretability, computational efficiency, and predictive reliability.

Keywords: Alzheimer's disease, Data augmentation, Brownian Log Scaling Archimedes Optimization-based Watershed Segmentation (BLSAOWS), Base Switch Rule Infmum and Supremum-based Rock Hyrax Swarm Optimization (BSRISRHSO), GELU and SWISH-based Radial Basis Function Network (GS-RBFN), Recursive Hypothesis-Creation Algorithm (RHCA), Phylogenetic Method (PM), one Gray-Level Co-occurrence Matrix (GLCM), Gray-Level Co-occurrence Matrix (GLCM Genetic Algorithm (GA), Deep-AD3-Net classifier.

Prof. (Dr.) MOHAMED BASHEER K.P
PEN: 677975
Principal
Amal College of Advanced Studies
Eranhimangad P.O., Nilambur - 679329

സംഗ്രഹം

ഓർമശക്തി, അറിവ്, പെരുമാറ്റം എന്നിവയെ തകരാറിലാക്കുന്ന അൽഷിമേഴ്സ് രോഗം (എഡി) ഒരു പുരോഗമന ന്യൂറോ ഡിജനറേറ്റീവ് ഡിസോർഡർ (എൻഡി) ആണ്. 60-80% ഡിമെൻഷ്യ കേസുകൾ കണക്കിലെടുക്കുമ്പോൾ, എഡി നേരിയ മെമ്മറി നഷ്ടത്തിൽ നിന്ന് പരിസ്ഥിതിയുമായുള്ള ഇടപെടൽ പൂർണ്ണമായ നഷ്ടത്തിലേക്ക് മുന്നേറുന്നു. എഡിക്ക് ചികിത്സയില്ലാത്തതിനാൽ, രോഗത്തിന്റെ പുരോഗതി ലഘൂകരിക്കുന്നതിന് നേരത്തെയുള്ള കണ്ടെത്തൽ അത്യന്താപേക്ഷിതമാണ്. നിലവിൽ, മെഷീൻ ലേണിംഗും (എംഎൽ) ഡീപ്പ് ലേണിംഗും (ഡിഎൽ) ന്യൂറോ ഇമേജിംഗ് അടിസ്ഥാനമാക്കിയുള്ള എഡി പ്രവചനത്തിൽ ലാസ്സോ റിഗ്രെസിയോ എന്ന സമീപനത്തിലൂടെ വാഗ്ദാനങ്ങൾ പ്രദർശിപ്പിച്ചിട്ടുണ്ട്.

ഈ വെല്ലുവിളികളെ നേരിടാൻ, ഈ പഠനത്തിൽ രണ്ട് ഭാഗങ്ങളുള്ള ചട്ടക്കൂട് അവതരിപ്പിക്കുന്നു. GELU സ്പ്രിഷ് റേഡിയൽ ബേസിസ് ഫംഗ്ഷൻ നെറ്റ്വർക്ക് (GS-RBFN) മുഖേന പ്രവചനവും വർഗ്ഗീകരണ കൃത്യതയും വർദ്ധിപ്പിക്കുന്നതിന് AD ന്യൂറോഇമേജിംഗ് ഇനിഷ്യേറ്റീവ് (ADNI) MRI ഡാറ്റാസെറ്റ് ആദ്യമായി നടപ്പിലാക്കുന്നു. എംആർഐ ചിത്രങ്ങൾ നോർമലൈസേഷൻ, തലയോട്ടി നീക്കം ചെയ്യൽ, സ്പേഷ്യൽ മിനുസപ്പെടുത്തൽ തുടങ്ങിയ പ്രീപ്രോസസിംഗ് ഘട്ടങ്ങൾക്ക് വിധേയമാകുന്നു, തുടർന്ന് ബ്രൗണിയൻ ലോഗ് സ്കെയിലിംഗ് ആർക്കിമിഡീസ് ഒപ്റ്റിമൈസേഷൻ കേന്ദ്രീകൃത വാട്ടർഷെഡ് സെ ഉപയോഗിച്ച് അത്യാവശ്യ മസ്തിഷ്ക കോശ വിഭജനം നടത്തുന്നു.

രണ്ടാം നടപ്പാക്കലിൽ, AD (Alzheimer's Disease) അപകടസാധ്യതാ സ്കോറിംഗ് ഘട്ട പ്രവചനം TADPOLE (The AD Prediction Of Longitudinal Evolution) ഡാറ്റസെറ്റ് ഉപയോഗിച്ചാണ് കേന്ദ്രീകരിക്കുന്നത്. ഈ രീതിയിൽ പ്രധാന ഘടകങ്ങളെ റാങ്ക് ചെയ്യുക, റിസ്ക് സ്കോർ കണക്കാക്കുക, ബ്രെയിൻ ശ്രിങ്കേജിനെ വിശകലനം ചെയ്യുക എന്നിവ ഉൾപ്പെടുന്നു. പ്രധാന ഘടകങ്ങൾ Recursive Hypothesis-Creation Algorithm (RHCA) ഉപയോഗിച്ച് തിരഞ്ഞെടുക്കപ്പെടുന്നു, True True Self-Weighting Mechanism (TT-SWM) റിസ്ക് സ്കോർ കണക്കാക്കുന്നു. Queue-Boltzmann-Constant-Sphere (QBCS) സാങ്കേതിക വിദ്യ ഉപയോഗിച്ച് ഹിപ്പോകാംപസിലെ ബ്രെയിൻ ശ്രിങ്കേജം അളക്കുമ്പോൾ, Gray-Level Co-occurrence Matrix (GLCM) ഫീച്ചറുകൾ Deep-AD3-Net ക്ലാസിഫയർ ഉപയോഗിച്ച് ഘട്ടനിർണയം സുഗമമാക്കുന്നു.

Prof. (Dr.) MOHAMED BASHEER K.P
PEN: 677975
Principal
Amal College of Advanced Studies
Eranhimangad P.O., Nilambur - 679329

സൂചകപദങ്ങൾ: അൽഷിമേഴ്സ് രോഗം • ഡാറ്റാ വർദ്ധനവ് • ബ്രൗണിയൻ ലോഗ് സ്കെയിലിംഗ് ആർക്കിമിഡീസ് ഒപ്റ്റിമൈസേഷൻ അടിസ്ഥാനമാക്കിയുള്ള വാട്ടർഷെഡ് സെഗ്മെന്റേഷൻ (BLSAOWS) • ബേസ് സ്വിച്ച് റൂൾ ഇൻഫ്ലം ആൻഡ് സുപ്രീമം അടിസ്ഥാനമാക്കിയുള്ള റോക്ക് ഹൈറാക്സ് സ്വാം ഒപ്റ്റിമൈസേഷൻ (BSRISRHSO) • GELU, SWISH അടിസ്ഥാനമാക്കിയുള്ള റേഡിയൽ ബേസിസ് ഫംഗ്ഷൻ നെറ്റ്വർക്ക് (GS-RBFN), റിക്കർസീവ് ഹൈപ്പോതെസിസ്-ക്രിയേഷൻ അൽഗോരിതം (RHCA), ഫൈലോജെനെറ്റിക് രീതി (PM), ഗ്രേ-ലെവൽ കോ-ഒക്കുറൻസ് മാട്രിക്സ് (GLCM), ജനിതക അൽഗോരിതം (GA), ഡീപ്-AD3-നെറ്റ് ക്ലാസിഫയർ.

Prof. (Dr.) MOHAMED BASHEER K.P
PEN: 677975
Principal
Amal College of Advanced Studies
Eranhimangad P.O., Nilambur - 679329

CHAPTER 1
INTRODUCTION

1.1 Overview

A progressive neurological disorder characterized by gradual memory loss, behavioural changes, and cognitive decline is termed Alzheimer's (AD). As the chief common form of dementia, AD significantly impacts the lives of millions of people all over the globe. Dementia, which is severe enough to affect social interactions and daily functioning, is a considerable loss of cognitive abilities. Several illnesses can result in dementia by harming brain cells, and one of the primary causes of this condition is AD.

1.1.1 Growing Impact of Data and Technology

With the accessibility of massive amounts of data and rapidly evolving technology, researchers across the globe are utilizing the synergistic combination of these resources to make substantial impacts on society. These advancements have opened new avenues for disease detection and diagnosis in the medical field, particularly in medical image processing (Kumar et al., 2021). Exploiting radiological images to extract clinical information that can provide faster and more accurate results for medical professionals is the objective, thereby enhancing the diagnosis and management of diseases like Alzheimer's.

1.1.2 Understanding Dementia and Its Forms

Dementia comes in numerous forms, each with its etiology and set of symptoms. For instance, vascular dementia results from decreased blood supply to brain areas, often caused by a stroke. The most basic and common form of dementia, marked by memory loss and psychological deterioration due to damage to brain cells is AD (Fuchs et al., 2020). WHO delineates dementia as a chronic brain disease categorized by a progressive decline in cognitive ability, which severely impairs social functioning?

1.1.3 Role of Imaging in Disease Detection

The detection and identification of diseases like AD have been significantly improved by tremendous advancements in nuclear imaging techniques. Methodologies, namely Magnetic Resonance Imaging (MRI) and Functional MRI (fMRI) permit for comprehensive investigation of brain functions and structures, helping in early AD detection (Rashid et al., 2020). Supplementary data could be rendered by combining various imaging modalities, improving diagnostic precision. By integrating radiological images from multiple sources, the challenge of representing different features and extracting information from each modality is addressed.

1.2 Alzheimer's Disease Overview and Progression

A gradually developing ND, which slowly erodes a person's capability of remembering, thinking, and eventually carrying out the simplest regular tasks, is AD. As the disease progresses, it becomes one of the important causes of mortality, especially amongst the elderly, ranking just behind cancer and heart-related diseases (Varsesi et al., 2022).

In the AD's early stages, people may experience difficulty recalling names, recognizing new people, or organizing daily tasks. As the disease progresses, symptoms become more severe, resulting in important impairments in daily functioning and eventually requiring 24/7 assistance.

Some of the early symptoms of AD include:

- Difficulty recalling the right words or recognizing new people.
- Challenges in social interactions or workplace settings.
- Misplacing objects or struggling to find items.
- Increasing difficulty in planning, organizing, and completing tasks.

As the disease advances, individuals may lose the potential to understand their environment, communicate effectively, or perform basic physical functions. At this

stage, continuous support is required; also, the risk of developing other health conditions, such as lung infections, increases.

Dementia, which results from brain cell damage, is an extensive medical term referring to the loss of cognitive abilities, namely comprehension, thinking, and memory (Aggarwal et al., 2022). AD is the most common cause of dementia, which accounts for the major dementia cases globally. The amassing of 2 abnormal protein fragments in the brain, namely beta-Amyloid Plaques (APs) and tau tangles is the hallmark of AD. The brain cells' normal functioning is disrupted by those proteins, leading to death.

Neurons produce irregular bundles of fibers and abnormal clumps in an individual with AD's brain. These plaques and tangles interfere with the capability of neurons for communicating with each other, disrupting vital processes, and eventually leading to the death of brain cells. As the disease advances, this process of neurodegeneration is evident in the significant shrinkage of the brain. The stark difference betwixt a healthy brain and one severely affected by AD is indicated in Figure 1.1

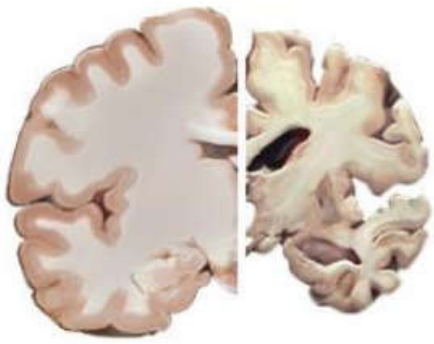

Figure 1.1 : A healthy brain (Left) compared with a brain severely affected by Alzheimer's Disease (Right).

The damage to brain cells is irretrievable in AD, causing a progressive decline in cognitive abilities. The affected individual's memory and thinking abilities deteriorate as the brain shrinks, thus severely influencing their quality of life (Sharma et al., 2021). Currently, AD is the 6th leading cause of mortality in the US. With the number of people affected by AD projected to double by 2050, the

disease's impact is expected to grow considerably. On average, a person diagnosed with AD has a life expectancy of only eight years after the initial symptoms appear (Lulita et al., 2022).

1.2.1 Causes of AD

AD is caused by an amalgamation of hereditary, age-related, and lifestyle factors. The disease begins with the amassing of beta-APs and tau tangles in the brain, disrupting neuron function and resulting in cognitive decline (Breijeh & Karaman, 2020). The most important risk factor is age, with the possibility of developing AD doubling every 5 years subsequent to age 65. Genetics also play a significant role in people with a family history of AD, particularly those carrying the APOE-e4 gene are at high risk. The risk of developing AD is further influenced by lifestyle factors, namely diet, physical activities, and chronic conditions like cardiovascular disease.

1.2.2 Symptoms of AD

The AD's earliest symptom is usually short-term memory loss, followed by disorientation in time, place, and events. Patients experience severe mood swings, confusion, and behavioral changes as the disease progresses, often resulting in suspicion of family and caregivers. Further, communication abilities deteriorate, thereby making speaking, swallowing, and walking difficult (Cummings, 2021). The degeneration spreads to brain areas controlling logical thinking and emotional regulation, thus leading to paranoia, hallucinations, and erratic mood changes. Deep memories are lost, and vital functions like heart rate and breathing are compromised in advanced stages, ultimately leading to death.

1.2.3 Diagnosis of AD

Both clinical and neuropathophysiological approaches are involved in the diagnosis of AD. Criteria that classify AD into three levels (Carlgren et al., 2020): Possible, Probable, and Definite have been set by the National Institute of Neurological and Communicative Disorders and Stroke (NINCDS). Neuropathophysiological diagnosis concentrates on biomarkers like beta-APs and tau levels in Cerebrospinal Fluid (CSF), and neuroimaging techniques, namely MRI and PET scans, which

assess brain structure and function (Hameed et al., 2020). Nevertheless, these approaches are still under research and lack standardized values for definitive diagnosis. AD is clinically diagnosed through neurological and mental status exams, cognitive assessments like the Mini-Mental State Exam (MMSE), and a review of the patient's lifestyle, medical history, and other risk factors. These approaches assist in differentiating AD from other similar conditions, namely frontotemporal dementia and vascular dementia. In Figure 1.2, the different types of AD Diagnosis are shown.

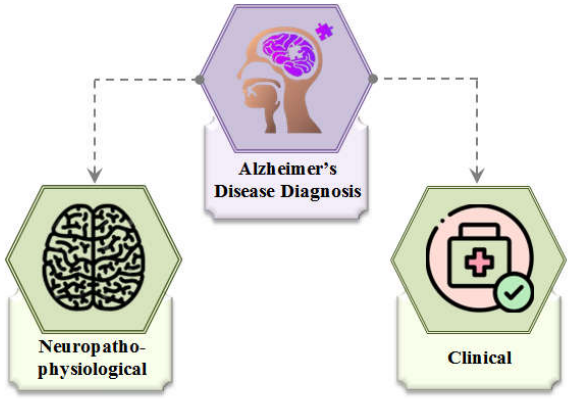

Figure 1.2 Types of Alzheimer's Disease Diagnosis

1.2.4 Stages of AD

AD progresses through various stages, each varying in severity and symptoms. Primarily, if a person shows no cognitive decline or memory loss, then it is categorized as Normal Control (NC). The disease further progresses to Mild Cognitive Impairment (MCI), which is partitioned into Early MCI (EMCI) and Late MCI (LMCI). Memory loss begins in the EMCI stage but may not be noticeable to the individual (Dubois et al., 2021). As memory decline worsens, the condition progresses to LMCI in which cognitive issues become apparent to family and friends. AD is the final and most severe stage, where all symptoms, comprising significant cognitive impairment and memory loss, are fully established.

1.2.5 Clinical Tests for AD Diagnosis

It is significant to diagnose AD early to manage its progression, though it remains challenging due to the disease's gradual onset. While age and genetic history are significant risk factors, definitive diagnosis depends on detecting beta-APs and tau proteins in tissues in the brain, often through invasive procedures. A combination of patient histories, mental state examinations like the MMSE, and non-invasive imaging approaches, namely MRI and PET scans are involved in the clinical diagnosis. AD diagnosis has been revolutionized by these imaging studies through the detection of structural changes, such as cerebral shrinkage and enlarged brain ventricles, which are indicative of the disease (T). Ultimately, although advances in medical imaging continue to improve early detection, a conclusive diagnosis often requires microscopic analysis of brain tissue after death.

1.2.6 Brain Changes Associated with Alzheimer's Disease

The brain, containing around a hundred billion neurons in an adult who is healthy, is an incredibly complex organ. Every neuron comprises longer, branching extensions that form relations with other neurons at points termed synapses. These synapses facilitate the rapid transmission of information through bursts of chemicals, numbering around 100 trillion in the brain. This communication network supports the cellular basis of thoughts, memories, sensations, movements, emotions, and skills (Trejo-lopez et al., 2023).

Several changes occur within the brain in AD, disrupting its normal function. The amassing of beta-APs outside neurons and tau tangles inside neurons are the 2 most important changes.

1.2.6.1 Beta-Amyloid Plaques

Protein fragments accumulating outside neurons are termed Beta-APs. These plaques, along with smaller clusters known as oligomers, are believed to contribute to neuron damage and eventual death (a process referred to as neurodegeneration) (Luo et al., 2021). APs interfere with neuron-to-neuron communication at synapses, disrupting the brain's signaling pathways.

1.2.6.2 Tau Tangles

An abnormal form of the protein tau accumulates inside neurons, forming tau tangles. The transportation of essential nutrients and other molecules within neurons is obstructed by the tangles, compromising cell function (Horie et al., 2021). As per the research, beta-APs start amassing prior to the formation of tau tangles, with increased beta-amyloid levels leading to subsequent increases in tau.

1.2.6.3 Inflammation and Atrophy

Along with plaques and tangles, inflammation and atrophy are the other brain changes related to Alzheimer's. Immune system cells in the brain, referred to as microglia, are activated by the occurrence of toxic beta-APs and tau proteins (Penkie et al., 2020). These cells clear the toxic debris and proteins from dying and dead cells. Nevertheless, when microglia cannot carry on with the clearing process, chronic inflammation sets in, thereby exacerbating the damage.

When neurons die and are not replaced, atrophy or brain shrinkage occurs. This cell loss causes a significant reduction in brain volume, further impairing normal brain function. Compounding these issues, AD also impairs the brain's capability of metabolizing glucose, which is its key fuel source. The brain's energy supply dwindles as glucose metabolism decreases, contributing to the decline in cognitive and physical functions.

1.2.7 Early Indicators of Alzheimer's

According to prominent research on individuals with rare hereditary mutations causing AD, changes in the brain begin long before symptoms appear. Beta-AP levels in the brain increased considerably, which started twenty-twenty years prior to symptoms were expected. Glucose metabolism was initiated to reduce eighteen years prior to symptoms, and Brain Atrophy (BA) was observed starting thirteen years prior to symptoms were anticipated to manifest (Rossini et al., 2020). The importance of early detection and intervention in AD is highlighted by these findings as the underlying brain changes begin decades before clinical symptoms are noticeable.

Although important progress has been made in understanding the brain changes related to AD, acknowledging that the majority of the research hasn't encompassed adequate representation of diverse populations is pivotal. Despite being integral parts of the US population, Hispanics/Latinos, Black/African Americans, Asian Americans/Pacific Islanders, and Native Americans are often underrepresented in Alzheimer's research. In future research, ensuring that including a range of participants is essential for developing effective treatments across different demographic groups.

1.2.8 Global Burden of Alzheimer's Disease

A primary cause of death all over the globe is AD. A study from 2018 revealed that mortalities attributed to AD increased by more than 16% while mortalities due to heart disease were mitigated by 11% betwixt 2000 and 2015. Globally, AD directly or indirectly affects one out of every ten people. 5.1 million people are impacted by AD in the United States alone, and to address the growing demand for AD treatment, there is no sufficient Healthcare (HC) infrastructure (Nandi et al., 2022).

The global burden of the disease is further exacerbated by the lack of targeted medications and effective treatment options for AD. A time-consuming and expensive process that requires collecting and analyzing large amounts of data is detecting AD in its early stages. Yet, promising solutions to improve AD diagnosis and risk prediction accuracy and efficiency are offered by technological innovations, especially in AI and ML.

1.3 Medical Imaging

To diagnose and treat numerous diseases, medical imaging plays an essential role by permitting HC experts for visualizing the human body's internal structures (Shamshad et al., 2023). It involves utilizing different techniques and technologies for creating images of the organs and tissues of the body, which can further be investigated for clinical diagnosis.

To identify and analyze specific human tissue structures, Medical Image Segmentation (MIS) divides an image into multiple non-overlapping regions. This

segmentation is vital for improving clinical diagnosis by allowing more accessible analysis of medical images (Panayides et al., 2020). For instance, image segmentation is utilized for detecting brain tumors from CT or MR images, serving as a critical first step in image analysis and interpretation. Partitioning digital images into meaningful segments that facilitate the treatment and diagnosis of diseases is the objective.

Over the past decade, the medical imaging field has undergone important advancements, resulting in the growth of less invasive and more accurate diagnostic tools (Varoquaux & Cheplygina, 2022). Medical Imaging Techniques (MITs), combining engineering knowledge with medical physics and biomedical engineering, are used to study human behavior and neurobiology. Key imaging modalities are:

- X-ray Radiography
- X-ray Computed Tomography (CT)
- MRI
- Ultrasonography
- Elastography
- Optical Imaging
- Single Photon Emission CT (SPECT)
- Positron Emission Tomography (PET)
- Thermography
- Terahertz Imaging

Each technique penetrates the human body with a specific energy source, creating signals detected and converted into images. Essential information about the internal structures of the patient is revealed by these images, permitting HC providers to effectively monitor and diagnose numerous conditions.

Enhancing, restoring, and analyzing medical images are involved in medical image processing to improve their quality and usefulness for diagnosis. However, several challenges persist, including:

- Enhancement and restoration of images
- Accurate and automated segmentation of features of interest
- Automated and precise registration of multimodal images
- Ordering and dimensioning of image features
- Integration of systems for clinical applications

These challenges arise from the complexity of biological variations along with the limitations of imaging modalities, including X-ray, MRI, and CT. Image segmentation is specifically challenging as it typically involves manually locating objects of interest and boundaries within volumetric images, necessitating expert knowledge and significant time.

For detecting abnormalities and monitoring recovery and treatment progress, especially post-surgery, medical imaging is vital, which integrates expertise from various fields, including medicine, radiography, biomedical engineering, and medical physics. MIS has turned out to be a standard approach recently to visualize brain structures and perform volumetric and shape comparisons (Willemink et al., 2020). Fully automatic approaches don’t permit human intervention while manual segmentation is labor-intensive and requires training. Thus, semi-automatic methods, which allow some degree of user input, have turned into the preferred approach in MIS.

1.4 Techniques for Alzheimer's Disease Prediction

To predict AD, various techniques are employed, from traditional methods to modern Artificial Intelligence (AI) approaches (Shastry et al., 2022). To analyze patient data and predict the likelihood of developing Alzheimer's, data mining and statistical methods have been used traditionally. More recently, prominence in

predicting AD has been gained by advancements in AI and its subsets, such as ML and DL (Kavitha et al., 2022). Due to these AI techniques' abilities to handle large datasets, recognize complex patterns, and improve the accuracy of early diagnosis, they are increasingly preferred.

Machine Learning: For predicting the risk of developing AD, ML algorithms, such as SVM, Decision Trees (DTs), and Random Forests (RFs), are wielded to analyze various features from patient data, including genetic, cognitive, and neuroimaging data (Shahbaz et al., 2019). These models learn from prevailing data to enhance their predictions over time, making them valuable tools for early detection.

Deep Learning: It is a more advanced subset of ML that wields Neural Networks (NNs) with multi-layers for processing complicated datasets (Saratxaga et al., 2021). For detecting subtle changes in brain structure related to AD, techniques like CNNs and Recurrent NNs (RNNs) are especially efficient in investigating medical images like MRI and PET scans (Salehi et al., 2020). To identify early signs of AD, DL models have shown superior performance, often outperforming traditional ML methods.

Figure 1.3 displays that AI and its subset techniques are utilized for predicting AD.

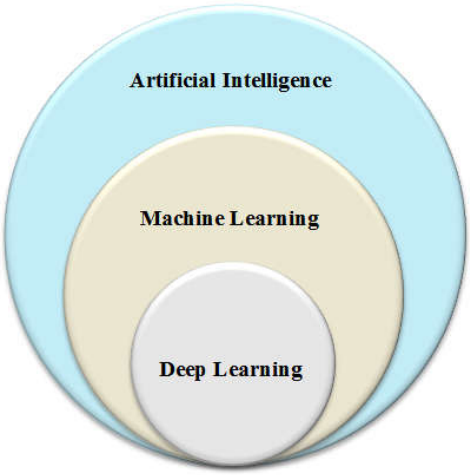

Figure 1.3: Techniques for prediction of AD

1.5 Motivation for the Study

The AD's manual diagnosis is a challenging and onerous process, often requiring an amalgamation of cognitive testing and neuroimaging to conclude. Given the subtle differences between normal aging and early-stage AD, difficulties are experienced by clinicians in making accurate diagnoses based solely on cognitive assessments. This issue is compounded by the subjective nature of these tests and the time required to manually analyze neuroimaging results. Many ML binary classification techniques have been applied by earlier studies in Dementia classification, which also utilized multiple biomarkers from MRI, PET, SPECT, or Neuropsychological data. To improve classification accuracy, few studies have attempted to integrate biomarkers, and very seldom have a multiclass grouping of normal controls, moderate cognitive impairment, and Alzheimer's Dementia. Owing to the small structural changes in the brain occurring during the AD's early stages, early biomarkers for MCI are hard to obtain.

To enhance improving the AD diagnosis's accuracy, the integration of biomarkers, mainly those identified in brain cells through neuroimaging, offers a promising avenue. Nevertheless, conventional image processing and analysis techniques often struggle with the complexity and variability of brain structures. This has resulted in a growing interest in applying advanced AI and ML techniques to this problem.

Impacting the power of ML, particularly DL, for improving the early detection and classification of AD is this research's aim. This research seeks to provide tools to support clinicians in making more precise and timely diagnoses by developing models that can automatically analyze neuroimaging data and identify subtle patterns indicative of AD.

1.6 Problem Statement

A decline in mental abilities and memory is caused by the progressive deterioration of the brain caused by AD, eventually leading to functional impairment termed dementia. The most widespread cause of dementia is AD. Despite extensive research, the AD's exact etiology remains unknown, with genetic, environmental,

and behavioral factors contributing to its development. The AD's initial symptoms are typically mild, characterized by memory loss and trouble in carrying out daily tasks. Yet, the condition can advance to personality changes, severe memory impairment, and a complete loss of communication and self-care abilities. The emotional and financial strain imposed on individuals and their loved ones by this illness is substantial. Therapies and lifestyle modifications can assist in managing symptoms and slowing the disease's progression though there is recently no treatment for AD. Still, the disease's fundamental causes are being investigated, and ongoing research focuses on developing more effective treatments.

The proposed research has two sections that address different challenges and objectives related to AD diagnosis and classification.

1. In the first proposal, limitations in current methodologies are identified for analyzing brain MR images in the context of AD diagnosis. Challenges comprise handling variations in cytoarchitecture, segmenting images with noisy backgrounds, and addressing non-brain tissues in MRI scans. Addressing these challenges using techniques, namely data augmentation, image pre-processing, skull stripping, and classification using a GS-Radial Basis Function Networks **(**GS-RBFNs) model is the proposed approach's aim.

2. In the 2nd proposal, the challenges in AD risk prediction, including overfitting, variability in Intra Cranial-Volume (ICV), limitations of ADAS-Cog 13 as a primary endpoint, and the need for texture analysis in assessing brain volume changes are focused. To improve risk prediction accuracy and address these issues, the proposed solution involves the development of a TT Self-Weighted Deep-AD3NET model using the Tadpole dataset.

To advance AD diagnosis and classification, each proposal identifies specific challenges and proposes targeted solutions, demonstrating a comprehensive approach to addressing the various aspects of the disease.

1.7 Research Objective

Developing innovative methodologies for early diagnosis and accurate classification of AD using advanced neuroimaging techniques and AI algorithms is the aim of the research.

Objectives

1. To propose a novel approach for early prediction and classification of AD utilizing a GS-RBFN.
2. To improve methods for predicting AD risk by addressing issues, such as overfitting, variability in ICV, and limitations of existing cognitive assessment tools. To develop a novel prediction model using the TT-SW Deep-AD_3NET approach to enhance accuracy and reliability.

Key contributions

- When compared to baseline techniques, the proposed model achieves superior accuracy in classifying AD stages, addressing challenges in accurate and early AD prediction.
- The model offers improved performance in predicting AD stages and assessing the risk of AD development by including a metric ranking technique and DL classifier.

1.8 Significance of the Study

This research is important due to its capability of revolutionizing the early diagnosis and treatment of AD. This research aims to offer more precise and early AD predictions by developing a robust framework that integrates multiple data sources and leverages advanced ML techniques, which could result in earlier interventions and better patient results. The findings of this research significantly contribute to medical imaging, ML, and neurological disease management, offering new tools and methodologies for clinicians and researchers.

1.9 Scope and Limitations

- **Scope:** To early diagnose and classify AD utilizing neuroimaging data, this research focuses on developing ML models. The research will primarily utilize MRI and fMRI data from publicly available datasets, namely the ADNI. For enhancing diagnostic accuracy, the study will analyze the combination of multimodal data sources and apply advanced machine-learning techniques.
- **Limitations:** The study is limited by the availability and quality of neuroimaging data, which may affect the findings' generalizability. Moreover, the study will concentrate on the development and validation of ML models, and while interpretability is a key consideration, implementing these models in clinical settings will require further validation and testing.

1.10 Thesis Structure

Chapter 1: Introduction

- In this chapter, AD is introduced, discussing its impact on patients and the HC system. This chapter outlines the motivation behind the research, emphasizing the significance of early diagnosis and precise classification of AD. Along with that, the problem statement, research objectives, the study's significance, and the scope of the research are detailed in this chapter.

Chapter 2: Literature Survey

- This chapter renders a comprehensive review of conventional research on AD diagnosis and classification. Traditional methods, data mining, statistical techniques, and modern advancements in ML, DL, and neuroimaging technologies are covered in this chapter. This survey recognizes gaps in recent methodologies and sets the stage for the proposed research.

Chapter 3: An Efficient GS-RBFN Framework for Early Prediction and Classification of AD

- In the first methodology chapter, a novel framework is presented using a GS-RBFN to early predict and classify AD. The steps involved in the

methodology, including image pre-processing, segmentation using the BLSAOWS technique, data augmentation, Feature Extraction (FE), and classification are discussed in this chapter. Also, the GS-RBFN framework's effectiveness in accurately categorizing AD into MCI, AD, and Cognitively Normal (CN) stages is evaluated.

Chapter 4: TT Self-Weighted Deep-AD3Net: An AD Stage and Risk Prediction

- In this chapter, the second proposed methodology, which focuses on predicting AD stages and associated risks using the TT Self-Weighted Deep-AD3Net model, is introduced. The process of ranking variables using the RHCA, FE using Genetic Algorithms (GAs), and RS prediction using the TT-SWM are outlined in the chapter. The methodology comprises brain shrinkage measurement using the QBCS approach and classification using the Deep-AD3Net model.

Chapter 5: Results and Discussion

- The outcomes acquired from applying the 2 proposed methodologies are presented in this chapter. Also, a comparative analysis of each method's performance, including accuracy, sensitivity, and specificity, is discussed. Insights into the strengths and limitations of every methodology and how they contribute to improving early diagnosis and classification of AD are provided in the chapter.

Chapter 6: Conclusion and Future Scope

- The research's key findings are summarized in the final chapter, emphasizing the contributions of the proposed methodologies to the field of AD diagnosis. In this chapter, the implications of these findings for clinical practice are discussed. This chapter summarizes potential areas for future research, namely extending the models to other NDs and incorporating additional data modalities to further improve diagnostic accuracy.

CHAPTER 2
LITERATURE SURVEY

2.1 Introduction

AD, which is the chief contributor to the cause of dementia globally, is a progressive ND. Generally, because of AD's neurodegenerative condition, the prediction of AD and identification of risk factors are prominent for early intervention and effective management. Furthermore, it is significant to comprehend the intricate interaction among risk factors for enacting precise interventions and tailored prevention approaches. Also, in this thesis, exploring an efficient prediction of AD and the identification of risk factors is mainly focused. In addition, the overview of the classification of AD using MRI is represented in Section 2.2, a comprehensive review of preprocessing approaches in AD detection is indicated in Section 2.3, the impact of FS strategies in predicting AD is examined in Section 2.4, the performance analysis of standard available datasets in the assessment of AD detection is presented in Section 2.5, the general contribution of AI in the prediction of AD is illustrated in Section 2.6, and the significance of identifying the risk factor for AD is represented in final section.op

2.2 Overview of the Classification of AD Using MRI

MRI emerges as a potent tool in the domain of neuroimaging for predicting AD, which captures detailed images of brain structures and abnormalities. Moreover, MRI-based classification can improve AD progression and develop personalized treatment tactics. In addition, MRI serves as a powerful tool for recognizing persons at risk of developing AD and facilitates timely interventions.

(Chaddad et al., 2018) analyzed the structure called the deep radiomic analysis for AD based on MRI. Effective features were implemented by this method centered on the CNN feature maps' entropy to improve AD classification and healthy control subjects. Moreover, this technique achieved the highest Area Under Curve (AUC) of 92.58% for the integrated radiomic features of alliu subcortical. Nevertheless, due to inadequate texture information, this apiuproach faced inherent challenges.

(Islam & Zhang, 2018) exemplified an architecture called the MRI-based AD diagnosis utilizing an ensemble system of deep CNN. Deep CNN was implemented by this framework to diagnose AD utilizing brain MRI data analysis. Additionally, in this scheme, the different stages of AD were identified. Also, it achieved precision of 94%, recall of 93%, and f1-score of 92%. Therefore, due to an inadequate training dataset, this framework had poor performance.

(Jain et al., 2019) assessed the method called the AD classification based on CNN using brain MRI. This structure implemented a mathematical model, which was represented as Data Preprocessing utilizing Freesurfer and Selection centered on Entropy, followed by further Classification utilizing TL. In addition, this scheme utilized data from the ADNI database. Moreover, for 3-way classification, this framework achieved 95.73% accuracy. Yet, due to the lack of available resources, this model had more complexity.

(Lian et al., 2020) displayed the framework called the structural MRI (sMRI)-based Hierarchical Fully Convolutional Network (H-FCN) for AD diagnosis and joint atrophy localization. This methodology implemented H-FCN for the automatic identification of the discriminative local patches and regions from the entire brain sMRI. Also, this model was evaluated with 2 independent datasets, namely ADNI-1 and ADNI-2 on a large cohort of subjects. Additionally, concerning automatic discriminative localization and brain disease diagnosis, this methodology achieved good results. However, due to supplementary information, this framework was more aggressive.

(Pan et al., 2020) introduced an effective early detection of AD for MRI utilizing CNN and Ensemble Learning (EL). This framework implemented a classifier by combining CNN and EL, which was represented as CNN-EL, for identifying subjects with MCI or AD utilizing MRI. Also, an accuracy rate of 0.05 was gained by this architecture to predict AD utilizing MRI. Nevertheless, owing to a lack of scalability, this framework had low classification accuracy.

(Ebrahimi & Luo, 2021) established a method called the detection of AD based on MRI images using CNN. For the accurate prediction of AD based on MRI, this technique employed 2-dimensional (2D) and 3-dimensional (3D) CNNs and RNNs. Additionally, this approach attained 96.88% accuracy, 100% sensitivity, and 94.12%

specificity by utilizing 3D voxel-based methods, respectively. However, owing to the massive number of learnable parameters, this methodology took more time to train.

(Ebrahimi et al., 2021) recommended an approach called AD detection from MRI using deep sequence modeling. To accurately detect AD, this technique implemented sequence-based Temporal Convolutional Network (TCN) and numerous kinds of RNNs. Also, this model applied ResNet-18 pre-trained on an ImageNet dataset. In addition, this scheme achieved 91.78% accuracy, 91.56% sensitivity, and 92% specificity in the classification of AD, respectively. Thus, due to inadequate features, this model suffered from irrelevant information.

(Guan et al., 2021) employed the system called the MRI-based AD prediction through distilling the multi-modal data knowledge. This model employed a multi-modal multi-instance distillation approach for distilling the knowledge learned as of the multimodal data to an MRI-centric network to predict MCI conversion. Furthermore, concerning AUC, this architecture achieved better accuracy. However, because of ineffective multimodalities, this model had an insignificant performance.

(Mehmood et al., 2021) described the methodology called the early AD diagnosis using a Transfer Learning (TL) approach centered on MRI. For the early AD diagnosis, this framework employed the Visual Geometry Group (VGG) architecture family with per-trained weights. Furthermore, for the diagnosis of AD, this architecture applied the ADNI database. In addition, this method achieved the highest rate of 98.73% regarding classification accuracy. However, due to insufficient training data, this framework had insignificant performance.

(Saratxaga et al., 2021) indicated the model called AD prediction utilizing DL-based solutions using MRI. To predict AD from MRI, this method implemented effective DL and image processing methods. Along with that, this framework obtained up to 0.93 balance accuracy for image-centric automated disease diagnosis. However, owing to the usage of a large number of data, this methodology had complex problems.

(EL-Geneedy et al., 2023) defined the system called the accurate detection of AD utilizing a DL technique centered on MRI. This model developed a DL-centric

pipeline to accurately diagnose and predict AD. Along with that, low CNN architecture and 2D T1-weighted MRI were wielded by this model to accurately predict and diagnose AD. In addition, this methodology acquired a high accuracy (99.68%) in terms of testing. Nevertheless, due to a massive amount of data augmentation techniques, this system had computational complexity.

2.3 Detailed Review on Pre-Processing Approaches in Ad Prediction

Pre-processing plays a pivotal part in detecting AD by refining raw data to enhance the predictive models' accuracy and effectiveness. Along with that, several issues, such as noise reduction, FE, and normalization through various techniques are represented in pre-processing, laying the foundation for robust and reliable predictions.

(Bhagwat et al., 2018) assessed an architecture called the prediction and modeling of clinical symptom trajectories in AD utilizing longitudinal data. In this approach, a computational framework was implemented with ML techniques to model symptom trajectories and predict symptom trajectories utilizing longitudinal and multimodal data. In addition, for the predictive tasks, this framework achieved a highly accurate performance (0.847). However, due to the utilization of multiple hidden layers, this technique took high computational time.

(Wang et al., 2018) presented an approach called the predictive modeling of the AD progression with RNN. For disease progression, this approach employed deep RNN with Long Short Term Memory (LSTM) cells. Furthermore, for supporting the shift of time steps, this scheme was believed to enhance "many-to-one" RNN architecture. In addition, regarding AD progressions, this methodology achieved 99% accuracy and outperformed classic baseline methods. Nevertheless, due to the lack of available predictive tools, this model showed incorrect prediction.

(Bohle et al., 2019) demonstrated the methodology called the MRI-based classification of AD using Layer-Wise Relevance Propagation (LRP) for explaining DNN decisions. In this approach, LRP was implemented for visualizing CNN decisions of AD centered on MRI data. In addition to that, this framework was utilized for a case-by-case assessment in a clinical setting. Hence, owing to insufficient ground truth in the heatmap, this model had poor accuracy.

(Hong et al., 2019) developed the technique called the prediction of AD using LSTM. A prediction model centered on LSTM was implemented in this method to predict the disease development from the temporal data of a patient. Additionally, for different data sizes, this framework was stable and achieved better performance. Yet, because this scheme accepted only a certain range of data sizes, it had a misclassification problem.

(Lorenzi et al., 2019) validated an approach called the probabilistic Disease Progression Modeling (DPM) for the prediction of AD. In this system, a reformulated DPM was implemented within a probabilistic setting for quantifying the diagnostic uncertainty of individual disease severity in a hypothetical clinical situation. Moreover, to assess diagnostic value and uncertainty related to various biomarkers, this model represented a valuable instrument. However, this framework failed to quantify the morphological brain changes precise quantification, leading to poor performance.

(El-Sappagh et al., 2020) analyzed the system called the detection of AD progression using a multimodal multitask DL model centered on time series data. To predict AD progression, this methodology employed a robust ensemble DL model centered on stacked CNN and a Bidirectional LSTM (BiLSTM) network. Together with that, this scheme was applied to an ADNI dataset, demonstrating this system's effectiveness. However, due to the lack of critical modalities, this method had poor accuracy.

(Nakagawa et al., 2020) employed the framework called the prediction of conversion for AD using deep survival analysis of MRI. This technique was implemented with MCI and CN subjects. Moreover, this approach utilized the grey matter volumes of brain regions in these subjects as a predictive feature. In addition, this model achieved a high rate (0.835) regarding the maximum concordance index. Nevertheless, due to the lack of available data, this framework failed to account for the competing risks.

Furthermore, in the following Table 2.1, the comprehensive review on pre-processing in the prediction of AD is represented.

Table 2.1: Comprehensive review on pre-processing in the AD prediction.

Author's Name	Algorithm	Precision	Sensitivity	Limitation
Altaf et al., (2018)	Hybrid FE approach, Gradwarp, B1 non-uniformity, and N3 bias field correction	-	92.11%	Due to the massive number of sample resources, this architecture consumed more time.
Maqsood et al., (2019)	TL classification model and Linear contrast stretching	74.27%	92.85%	This system failed to segment images, leading to poor performance in accuracy.
Parmar et al., (2020)	Motion Correlation, Intensity Normalization, and 3D-CNN	0.96805	0.9675	Due to the lack of functional data, this methodology struggled to generate unbalanced classes.
An et al., (2020)	Deep EL and Normalization	87.5%	-	Due to the unbiased labels, this system was not suitable for practical use and was more expensive.
Liu et al., (2020)	Multimodal DL based on CNN and Nonparametric Non-uniform intensity Normalization (N3)	-	83.05%	Owing to the lack of available features, this method did not predict brain abnormalities.
Khan et al., (2021)	Twin SVM (TSVM), Least Squares TSVM (LSTSVM), Robust Energy-centric LS-TSVM (RELS-TSVM), and Normalization	-	89.44%	Owing to the amalgamation of a large number of features, this model had irrelevant information.
Ghazal et al., (2022)	AD Detection empowered with TL Algorithm (ADDTLA) and Image Resizing	93.7%	91.5%	Due to the lack of hand-crafted features, this framework struggled for extraction.

2.4 Review on the Impact of Feature Selection in AD Prediction

FS plays a major part in AD prediction by assisting in the identification of relevant biomarkers and the reduction of dimensionality for complex data. Furthermore, for enhancing the AD prediction models' accuracy and efficiency, FS strategies are being explored rapidly by researchers with the recent development in ML and medical imaging technology.

(Mirzaei et al., 2018) executed the system called the 2-stage FS of voice parameters for the early AD prediction. A two-stage FS was implemented in this approach for extracting the pertinent features from speech in pathology groups. Along with that, for testing the three feature sets, this model applied three classification approaches, namely SVM, k-Nearest Neighbor (kNN), and DT. In addition, this framework achieved a relative gain of 70%, 88%, and 59% for kNN, SVM, and DT, correspondingly. However, due to insufficient samples, this architecture had poor classification.

(Parisot et al., 2018) validated the approach called the prediction of AD utilizing Graph Convolutional Network (GCN). This system employed a comprehensive assessment of a generic model, which leveraged both non-imaging and imaging information. Moreover, this framework was tested on two larger datasets, such as Autism Brain Image Data Exchange (ABIDE) and ADNI to predict Autism Spectrum Disorder (ASD) and conversion to AD. Moreover, this scheme achieved 70.4% and 80% classification accuracy in ABIDE and ADNI, respectively. Hence, due to the choice of node descriptors, this framework did not effectively capture the complex patterns.

(Xu et al., 2018) propounded a model called an efficient classifier to identify AD genes. To predict AD, the model employed an SVM centered on gene-coding protein sequence information. Moreover, concerning AD identification, this scheme achieved 85.7% accuracy. Along with that, for AD classification, this system worked under a synchronized dataset. Nevertheless, this approach had poor sensitivity concerning irregularized parameters.

(Jin & Deng, 2018) developed the framework called the prediction of various stages of AD utilizing Neighborhood Component Analysis (NCA) and ensemble DT. In this scheme, NCA was applied to selecting the most potent features to predict and develop an ensemble DT for predicting the group of subjects. Additionally,

regarding prediction on 160 test subjects, this system achieved 56.25% accuracy. Hence, due to the usage of unavailable subjects, this framework attained lackluster prediction performance.

(Lei et al., 2020) articulated the technique called AD prediction utilizing DL and joint learning of longitudinal data. This method developed a model centered on longitudinal multiple time points data for predicting the clinical scores. Moreover, in this approach, the public database of ADNI was utilized, which revealed the relation betwixt the clinical score and MRI data. In addition, this method presented a superior performance on the ADNI dataset. Nevertheless, owing to the usage of multiple modalities, this methodology had a computational burden.

(Hong et al., 2020) illustrated the system called the prediction of AD for time series neuroimage investigation. An effective time-series AD Prediction Model (ADPM), encompassing RF, Region Of Interest (ROI) selection, and Gated Recurrent Units (GRU) prediction was implemented in this framework. Furthermore, high classification accuracy was achieved by this methodology, which also facilitated the prediction of early-onset AD. Nevertheless, due to the high level of transparency, this technique experienced challenges with information overload.

(Zhang et al., 2021) recommended an approach called the AD multiclass diagnosis through multimodal neuroimaging embedding FS and feature fusion. In this technique, an effective AD multiclass classification methodology with embedding FS and feature fusion was implemented based on multimodal neuroimaging. Additionally, this structure applied the data from the public dataset ADNI; also, it consumed less time. However, for storing a kernel matrix, a larger amount of space was required by the method.

(El-Sappagh et al., 2021) demonstrated an architecture called multilayer multimodal detection along with prediction centered on explainable AI for AD. An interpretable and accurate AD diagnosis and progression detection framework was developed in this scheme. Additionally, this system achieved 90.51% cross-validation accuracy and 90.5% f1-score. Also, to predict and detect AD, this model worked on the ADNI dataset. Nevertheless, due to the consideration of baseline data, this method faced a challenge in analyzing the time series data.

Furthermore, Table 2.2 exemplifies the FS's performance analysis for the classification of AD.

Table 2.2: Performance analysis of feature selection for the prediction of AD.

Author's Name	Technique	Specificity (%)	Sensitivity (%)	Challenge
Zhou et al., (2018)	TrAdaboost Algorithm and Entropy-based FS	-	80	This approach had high computation complexity due to the utilization of larger sample sizes.
Gupta et al., (2019)	ML-based framework and Truncated Singular Value Decomposition (SVD) dimensionality reduction	96.44	95.47	This model displayed poor performance because of its limited capability to differentiate similar brain structures.
Hojjati et al., (2019)	3 and 4-group classification centered on the Sequential Feature Collection (SFC), Discriminant Correlation Analysis (DCA) FS algorithm, and Minimal Redundancy Maximal Relevance (MRMR).	72	62	Due to the presence of a massive number of hub nodes, this method exhibited abnormalities in large-scale network connectivity.
Duc et al., (2020)	SVM-centric RFE (SVM-RFE) and Least Absolute Shrinkage and Selection Operator (LESSO)	98.21	67.23	Due to the mandatory verification process for regression, this system did not generalize well for large datasets.
Divya & Kumari, (2021)	Recursive Feature Elimination (RFE) and GA	92.32	85.85	This framework experienced overfitting due to the imbalance in data sizes.

2.5 Performance Analysis of Standard Available Datasets in the Assessment of AD Detection

Datasets play an essential part in the prediction of AD. Also, they facilitate research endeavors for early detection, prognosis, and treatment development. Moreover,

invaluable insights into the multifaceted nature of AD are offered by comprehensive datasets, encompassing diverse patient demographics, clinical assessments, neuroimaging scans, genetic profiles, and biomarker data.

(Liu et al., 2018) recognized the method called the classification of AD by integrating CNN and RNN using Fluorodeoxyglucose PET (FDG-PET) images. This framework implemented an efficient classification approach centered on combining 2D CNN and RNN that learned the intra- and inter-slice features to classify AD. Moreover, to classify AD and MCIs in the ADNI dataset, this model achieved promising performance. Nevertheless, due to the utilization of PET images as input, this model struggled in dynamic prediction.

(Khan et al., 2019) introduced a technique called the prediction of AD using TL with intelligent training data selection. This system employed VGG architecture with pre-trained weights as of larger benchmark datasets comprising natural images. Additionally, this approach utilized the ADNI dataset and achieved a 4% and a 7% increase in accuracy. However, due to this framework's reliance on extensive training sets, it was not suitable for practical purposes.

(Iddi et al., 2019) signified the course of AD progression for detection. A two-stage approach was implemented in this methodology to model and predict measures of function, cognition, brain imaging, fluid biomarkers, along with diagnosis of individuals utilizing multiple domains concurrently. Moreover, this model achieved 80% accuracy from the ADNI dataset. However, due to the complexity of joint models, this technique required more computational time.

(Basaia et al., 2019) described the automated classification to predict AD and MIC utilizing a single MRI and DNNs. To predict the individual AD diagnosis and the MIC conversion to AD, this framework implemented a DL algorithm. Furthermore, this model obtained a higher accuracy for ADNI (99%) and the combined version of the ADNI and non-ADNI datasets (98%). However, this framework failed to address the atypical AD presentations owing to ineffective diagnostic tools.

(Bringas et al., 2020) described the DL model to identify AD. For recognizing the patterns, this scheme was employed with a processed time series and a CNN model. Moreover, this technique achieved 90.91% accuracy and 0.897 f1-score for the

CNN-based method. Hence, this approach struggled to generate the daily data sequence owing to inadequate available sequences.

(Park et al., 2020) employed a system called the AD prediction centered on DNN through the integration of gene expression and the Deoxyribonucleic Acid (DNA) methylation dataset. By utilizing larger-scale gene expression and DNA methylation datasets, this model employed a DL-based model for predicting AD. Also, an effective simple approach was implemented in this framework for reducing the number of features centered on a differentially expressed gene and a differentially methylated position in the multi-omics dataset. Additionally, as per this methodology, the integration of gene expression with DNA methylation data improved the prediction accuracy. Nevertheless, due to the integration of two molecular layers, this model had an overfitting problem.

(Basheer et al., 2021) illustrated the DNN approach for the computational modeling of dementia prediction by analyzing the Open Access Series of Imaging Studies (OASIS) dataset. This structure implemented an effective system by presenting alterations in the capsule network design for optimal prediction outcomes. Besides, the OASIS dataset was used in this framework for diagnosing the label into 2 categories, such as demented and non-demented. Along with that, this framework achieved 92.39% accuracy. Nevertheless, due to the utilization of a capsule network, this method was computationally more expensive.

(AbdulAzeem, et al., 2021) validated the method called CNN-centric end-to-end model for classifying AD. In this methodology, a CNN-based framework was employed to classify AD. Furthermore, for the binary classification of AD and CN, this model utilized the ADNI dataset. This model achieved a higher classification accuracy (97.5%). This system was affected by difficulties in achieving convergence in the NN due to the vanishing gradient problem.

(Hernandez-Lorenzo et al., 2022) showed the framework called the early diagnosis of AD using the limits of GNN. To tackle the challenges faced by the Genotype-based prediction of the phenotype, this system implemented ML techniques. Additionally, this method outperformed other ML techniques and achieved superior results by using protein-protein interactions. However, this methodology had improper interpretability analysis owing to the inability to export trained models.

(Kavitha et al., 2022) implemented the early-stage AD prediction using ML models. To identify the best parameters of AD prediction, this methodology employed seven ML models. As well, this method wielded the OASIS dataset and obtained 83% accuracy on the test data. Hence, due to the diverse source of data, this framework exhibited sensitivity to outliers.

Also, the comparative analysis of datasets in AD prediction is specified in the following Table 2.3.

Table 2.3: Comparative analysis of datasets in AD prediction.

Author's Name	Method	Dataset	Subjects	Accuracy	Limitation
Bi et al., (2020)	Un-supervised CNN	ADNI	1075	92.5%	Due to the utilization of 3D data as input, this methodology had complex and intense resources.
Zhu et al., (2021)	Dual Attention Multi-Instance DL Network (DA-MIDL)	ADNI and Australian Imaging, Biomarker and Lifestyle Flagship Study of Ageing (AIBL)	1689	0.863	This framework was unable to represent various local features due to the fixed size of input patches.
Zhao et al., (2021)	Multi-information Generative Adversarial Network (mi-GAN)	ADNI	201	78.45%	This system showed ineffective performance because it did not predict short-term brain images.
Zhang et al., (2023)	Tensor Multi-Task EL with Gradient Boosting (TMTL-GB)	ADNI	313	-	Due to the interference from the training data, this model experienced an overfitting problem.
Venkatasubramanian et al., (2023)	Multi-Task DL (MTDL)	ADNI-standardized MRI dataset.	449	94.5%	Due to the unavailability of resources, this system failed to validate real-time data.

2.6 General Contribution of AI in the Prediction of AD

To predict AD, AI arose as a powerful tool. AI comprises ML and DL methodologies. Furthermore, AI techniques can enhance the accuracy and early detection of AD. They also facilitate proactive interventions by analyzing diverse datasets, including neuroimaging, genetic, and clinical data. This emerging domain can transmute AD prediction and create a way for a novel age of precision medicine and better patient results.

(Lee et al., 2019) implemented a multi-modal DL technique for predicting AD progression. To predict the conversion from MCI to probable AD, this framework employed a multi-modal RNN. In addition, this structure incorporated longitudinal multi-domain data and obtained 81% accuracy. Also, this model achieved 75% accuracy in predicting the conversion from MCI to AD. Yet, due to the combined features in its parameters, this framework exhibited prediction errors.

(Li et al., 2019) executed a DL framework to early predict AD dementia centered on hippocampal MRI. A DL method was implemented in this method, which was also validated based on MRI scans of 2146 subjects for predicting MCI subject's progression to AD dementia in a time-to-event investigation setting. Moreover, this model rendered an economical and accurate means to prognosis and facilitated enrollment in clinical trials potentially. Hence, this technique exhibited incomplete and inaccurate predictions due to insufficient available data.

(Oh et al., 2019) exemplified the system called the classification and visualization of AD using Volumetric CNN and TL. In this framework, a convolutional autoencoder (CAE) was implemented, which was centered on unsupervised learning for performing the two various tasks. Moreover, this framework was validated on the ADNI database. Also, it achieved a high accuracy (80.27%) for the prediction of AD. However, this methodology had insignificant performance owing to the limited number of subjects.

(Fan et al., 2020) examined the AD classification centered on brain MRI and ML. In this methodology, the SVM model was implemented to classify and predict numerous disease processes of AD, which was centered on sMRI data. Additionally, for 317, 688, and 1203 sample training sets, this structure achieved classification accuracy of 65.49%, 68.07%, and 73.97%, respectively. However, due to the high noise and irrelevant data, this framework had a long execution process.

(Nguyen et al., 2020) analyzed the prediction of AD progression utilizing deep RNNs. A minimal RNN from the TADPOLE was implemented in this methodology. Also, from the ADNI dataset, this model utilized 1677 participants of longitudinal data. By using these participants, better accuracy was achieved by this system for the prediction of AD. Therefore, this framework struggled to detect the constant prediction due to the lack of stable subjects.

(Zhao et al., 2020) articulated the imaging of nonlinear and dynamic functional brain connectivity with the AD diagnosis application centered on EEG recordings. This approach implemented an effective brain functional connectivity imaging approach, which targeted the contribution of nonlinear dynamics of functional connectivity. Moreover, this method was generic and utilized as a powerful tool for investigating brain networks. However, owing to insufficient measuring tools, this system struggled to capture the complex network interaction.

(Liu et al., 2021) developed the model called AD detection using depthwise separable CNN. For improving the efficiency of the DL algorithm and classification of AD, this method employed a deep separable CNN model. Along with that, this approach was trained with two complicated networks, such as AlexNet and GoogLeNet, which were utilized for TL. Also, for AlexNet and GoogLeNet, the 2 trained frameworks achieved average classification rates of 91.40% and 93.02% and consumed less power. Nevertheless, owing to inefficient convolutional modules, this architecture had network complexity.

(Rodriguez et al., 2021) explained the framework called ML identifying candidates for drug repurposing in AD. Drug Repurposing In AD (DRIAD) was employed in this architecture, which quantified potential relations among the pathology of AD

severity and molecular mechanisms as encoded in lists of gene names. Also, in terms of logistic regression models, this system achieved the highest accuracy. Yet, this methodology did not examine the impacts on the key features due to inadequate available resources.

(Tian et al., 2021) recommended the method called modular ML to classify AD from retinal vasculature. In this approach, highly modular ML methodologies were employed for evaluating the retina. Moreover, this technique utilized data from the UK Biobank, and 82.44% average classification accuracy was achieved by the pipeline. Yet, because of limited data analysis techniques, this model hindered its clinical translation.

(Zhang et al., 2021) presented the methodology called the 3D densely connected CNN with a connection-wise attention mechanism for AD classification. To classify AD, this framework implemented a densely connected CNN for learning the brain MR images' multi-level features. Furthermore, this model achieved high accuracies of 97.35%, 87.82%, and 78.79% for healthy control, MCI converters against healthy control, and MCI converters against non-converters, respectively. Hence, due to the size of the input data, this approach struggled with network convergence.

(Chui et al., 2022) assessed MRI scans-centric AD detection through CNN and TL. In this technique, Generative Adversarial Network, CNN, and TL were employed, which were also represented as GAN-CNN-TL for enhancing the fine-tuning of hyper-parameters and detection accuracy. Additionally, this framework utilized OASIS-series datasets and achieved high accuracy. Yet, owing to the variation in the ground truth data, this system struggled for detection among different classes.

(Hajamohideen et al., 2023) explored the 4-way AD classification using DL with triplet-loss function. In this system, a Siamese CNN (SCNN) was implemented with a triplet-loss function to represent input MRI images as k-dimensional embeddings. Furthermore, by using ADNI and OASIS datasets, this architecture was tested and achieved a high accuracy (93.85%). However, owing to the high fraction of invalid data, this system had limited data problems.

Furthermore, Table 2.4 depicts the performance assessment of ML and DL in the prediction of AD.

Table 2.4: Performance evaluation of ML and DL in AD detection.

Author's Name	Method	Validation	F1-score	Precision	Limitation
Beheshti et al., (2017)	Automatic Computer-Aided Diagnosis (CAD) system	10 fold cross-validation	-	75.08	This architecture had computational complexity owing to the large size of data samples.
Liu et al., (2020)	Ensemble ML	k-fold cross validation	0.7806	0.8166	Due to the development of complex models, this method obtained poor performance.
Ljubic et al., (2020)	DL-based models	-	-	0.975	This approach struggled with predicting outcomes from input data due to its irregular temporal nature.
Lella et al., (2020)	Ensemble ML	10 fold cross-validation	0.145	-	Due to the lack of significant resources, this methodology exhibited poor performance in terms of various metrics.
Ni et al., (2021)	Two-stage TL	-	80.6%	85%	Because of the lack of consistent features, this system had slow convergence.
Li et al., (2022)	Regional Brain Fusion-Graph Convolutional Network (RBF-GCN)	10 fold cross-validation	-	-	This model consumed more execution time owing to the massive number of biomarker information.
Kang & Kang, (2023)	ML-based models	-	0.875	-	Owing to insufficient data quality, this model failed to clinically validate the input data.

2.7 Significant Identification of Risk Factor in AD

The identification of risk factors in AD is important for early detection and intervention strategies. Also, genetic factors, lifestyle choices, environmental influences, and medical background are investigated to understand the intricate causes of AD. Moreover, diagnostic accuracy is enhanced and also proactive interventions are enabled to reduce the influence of AD on people and HC systems.

(Tansey et al., 2018) developed the genetic risk for AD in specific macrophage and microglial transcriptional networks. This technique evaluated the overlap's significance among genome-wide important AD risk variants and sites of open chromatin from datasets. Moreover, this system provided evidence for the microglia's causal part in AD pathogenesis. Therefore, owing to the utilization of thousands of variants, this framework had an overfitting problem.

(McCartney et al., 2018) analyzed the relation betwixt DNA methylation age acceleration and risk factors for AD. To assess the relation betwixt age acceleration and AD risk factors, this technique implemented a multilevel model. Furthermore, the significant association betwixt epigenetic age acceleration and lifestyle-associated risk factors was identified by this model. This framework was unable to access the longitudinal changes because of its cross-sectional design.

(Zhang et al., 2020) depicted the method called the risk prediction of Late-Onset AD (LOAD). To predict LOAD, this framework employed the optimal P-threshold (Poptimal) of a Genetic RS (GRS). Additionally, in this approach, three independent datasets were applied and a GRS of 75% was obtained. Yet, because of the omission of non-additive genetic effects, this technique was incomplete in modeling.

(Wang et al., 2021) employed the system called the Genome-wide epistasis analysis for AD and genetic risk prediction. For compiling the epistasis risk factors into an Epistasis RS (EFS), this framework established an effective approach based on the multifactor dimensionality reduction. Moreover, for evaluating the ERS's feasibility in AD risk prediction, this methodology utilized two independent datasets. Together with that, in terms of identifying high-risk individuals, this system achieved better

performance. Nevertheless, due to the large number of search spaces, this model had scalability issues.

(Roshanzamir et al., 2021) indicated an approach called the transformer-centric DNN language models for AD risk evaluation from targeted speech. Centered on natural language processing, this methodology implemented DL models for AD's early risk evaluation from the picture description test. Also, 88.08% accuracy was achieved by this system in classification and enhanced the top-notch by 2.48%. This model exhibited misclassification results due to the massive amount of model parameters.

(W. Liu et al., 2023) analyzed the risk prediction of AD conversion in the MCI population centered on Brain Age Estimation (BAE). In this approach, an AD Conversion Risk Estimation System (CRES), comprising an automated MRI feature extractor, BAE module, and AD conversion risk estimation module, was implemented. Along with that, this methodology achieved important AG patterns of various clinical groups. Nevertheless, this technique struggled with underlying factors due to its lack of interpretability.

(Zhou et al., 2023) exemplified the framework called the DL-centric polygenic risk analysis to predict AD. To model AD polygenic risk, this methodology implemented NN models. Along with that, this method achieved the best performance by investigating the AD polygenic risk. Nevertheless, due to the integration of multiple genetic variations, this model increased the complexity.

(Gao et al., 2023) assessed the method called ML-based polygenic RSs and electronic health records for AD prediction. For the prediction of AD, this technique employed ML models. Moreover, in this method, data were utilized from the Alzheimer Disease Genetics Consortium and effective feature patterns were identified. This framework exhibited low prediction accuracy owing to the lack of available data.

2.8 Summary of the Literature Survey

AD prediction and risk factor identification are essential in early intervention. Moreover, ML techniques hold considerable information in predicting disease onset and identifying at-risk individuals. Furthermore, the key factors are explored through comprehensive research, genetic predispositions, lifestyle habits, and medical history. Furthermore, for early detection and targeted interventions in AD management, continuous advancements in predictive models offer promising avenues. Along with that, the existing work had the potential to lack comprehensive data regarding diverse demographic groups, thereby hindering the generalizability of the findings. Hence, in this chapter, the performance of numerous approaches for detecting AD is evaluated and the risk factors are analyzed. Furthermore, an overview of MRI-based AD detection, which predicted AD by using MRI as input, is indicated in section 2.2. Also, the performance of various prevailing techniques is evaluated in section 2.2 for the classification of AD from MRI. Moreover, in section 2.3, the pre-processing approaches for AD prediction, which explains various pre-processing approaches for evaluating the performance in terms of AD classification, are illustrated. Also, this section analogizes various information regarding preprocessing approaches, precision, sensitivity, and drawbacks from various existing works. Furthermore, the impact of FS on AD detection, which contains different FS techniques, is assessed in Section 2.4. Moreover, this section contrasts FS approaches, specificity, sensitivity, and challenges of different prevailing works for evaluating the performance of AD prediction. In the meantime, the performance analysis of standard available datasets to assess AD detection, which analyzes the performance of various datasets in the field of predicting AD, is explained in Section 2.5. Additionally, in Section 2.6, the general contribution of ML and DL approaches to classify AD, which analyzed the performance of a number of traditional techniques using ML and DL approaches, is represented. Lastly, the risk factors of AD, which mainly focus on the identification of various risk factors, are evaluated in Section 2.7. This literature survey's main objective is based on an in-depth understanding of various AD prediction and risk factor identification methods.

CHAPTER 3

EFFECTIVE GS-RBFNs CLASSIFIER FOR EARLY PREDICTION AND CLASSIFICATION OF ALZHEIMER'S DISEASE USING ADNI BRAIN MRI IMAGES

3.1 Introduction

AD is the most common type and the predominant form of dementia, which is also represented as a progressive ND. It begins with mild memory loss and results in subtle memory difficulties in effective communication and response (Patil & Borkar, 2023). This neurological condition targets the brain areas, thus responsible for cognition, memory retention, and linguistic abilities. In addition, its consequences affect daily tasks and compromise independent living through increasingly damaging cognitive functions, namely memory, decision-making, and problem-solving (Prabha & Sakkarapani, 2022). Also, the 2 main types of abnormal protein aggregates categorized by the amassing of AD are beta-APs and tau tangles (Sahoo, 2021). Beta-APs accumulate from the outside neurons, while the inside neurons are responsible for tau tangles (Tu et al., 2021). These pathological changes can cause damage to the neurons, inflammation, and BA and affect the hippocampus and cerebral cortex (Sheela & Suganthi, 2024).

Furthermore, AD has several clinical stages, such as the preclinical stage and MCI for reflecting various cognitive declines with AD. Alzheimer's begins in the preclinical stage by appearing the neurodegenerative lesions in the brain and ends by showing the first clinical symptoms (Anantapur & Patil, 2021). In the meantime, MCI starts with detectable symptoms without disturbing regular activities. It also results in dementia owing to AD. The stage betwixt normal aging and the onset of AD, which is also responsible for diagnosing AD, is MCI (Veeraiah et al., 2021). The AD diagnosis is based on history-taking, clinical presentation, and MCI behavior observation, which are vital to identifying patients during the MCI stage. Furthermore, based on recent research in 2020, approximately 5.8 million Americans were affected by AD, where above 65 aged peoples lived with AD.

Furthermore, this number doubles every 5 years, signifying that approximately 14 million Americans will be affected by AD in 2060. Hence, early detection and diagnosis of AD are very significant (Rani et al., 2022). Thus, by using numerous techniques, recent advancements in the early prediction and classification of AD are carried out. These techniques comprise numerous neuroimaging modalities, namely PET, Diffusion Tensor Imaging (DTI), and MRI that are applied to detect and diagnose AD (Bondada et al., 2021). Among these, MRI plays a key role in AD prediction and diagnosis by offering comprehensive structural and functional insights. Also, by using the MRI, the challenges like overlapping symptoms and limited diagnostic resources are overcome. Furthermore, for diagnosis, disease monitoring, and treatment evaluation, the structural and functional modalities serve as biomarkers (Raja Rao & Yesu Babu, 2020).

In contrast, the ADNI is referred to as the longitudinal multicenter study. It is tailored to establish clinical, imaging, genetic, and biochemical biomarkers to early detect and diagnose AD (Sangeetha & Sathappan, 2023). For identifying the biomarkers and improving the diagnostic approaches, ADNI has thousands of data collected from individuals with AD, MCI, and healthy controls (Dhende & Shirbahadurkar, 2022). Also, ADNI is applied to study disease trajectories and validate imaging biomarkers by collecting MRI data from the participants (Hai et al., 2023). For the accurate early prediction and classification of AD, several ADNI brain MRI-centric ML and DL approaches are utilized. To accurately detect AD, ML-based approaches like SVM and LR are applied; however, these models are affected by interpretability issues (Srilakshmi et al., 2022). In the meantime, DL approaches like CNN and DNN face challenges in accurate AD classification due to the large statistical errors. Also, these techniques required high computational resources and a larger dataset for robust classification of AD owing to the higher dimensionality of the brain MRI data (Srilakshmi et al., 2021). To overcome the abovementioned issues in the computer-aided diagnosis of AD, an efficient framework is proposed in this paper to accurately predict and classify AD using GS-RBFNs.

3.2 Proposed Methodology for the Accurate Prediction and Classification of AD Based on ADNI Brain MRI Using GS-RBFNS

An efficient technique called GS-RBFNs is applied in the proposed methodology to early predict and classify AD centered on analyzing the ADNI brain MRI. This framework effectively predicts and classifies the AD with robust results by applying a DL-based multi-model approach, improving the result parameters, including accuracy, precision, recall, etc. Several steps, such as preprocessing, image segmentation, morphological operation, data augmentation, image representation extraction, FS, and classification are included in the research methodology. Primarily, to accurately detect and classify AD, the data from the ADNI brain images are collected. Further, the collected data is given as input to the preprocessing, which includes intensity normalization, skull stripping, and spatial smoothing. Here, by using the proposed Tournament Global Thresholding (TGT) approach, the skull stripping process is done. After that, using BLSAOWS, the preprocessed image is segmented. Subsequently, for image reconstruction, the morphological operation, such as erosion, reconstruction, closing, and dilation process is performed on a segmented MRI image. Further, the reconstructed MRI image is applied to the data augmentation process, which contains deformation, flipping, scaling, cropping, and rotation of images. Next, the images from the data augmentation process are gathered and given to the image representation extraction phase, which includes segmented image-based patches, feature patches selection, and patches concatenation. Subsequently, from the image representation, features are extracted. By utilizing the BSRISRHSO algorithm, images are selected. Lastly, efficient classification is carried out centered on the features selected by using the GS-RBFNs approach, which classifies the features into AD, MCI, and Control Normal. Figure 3.1 depicts the structural representation of the proposed methodology.

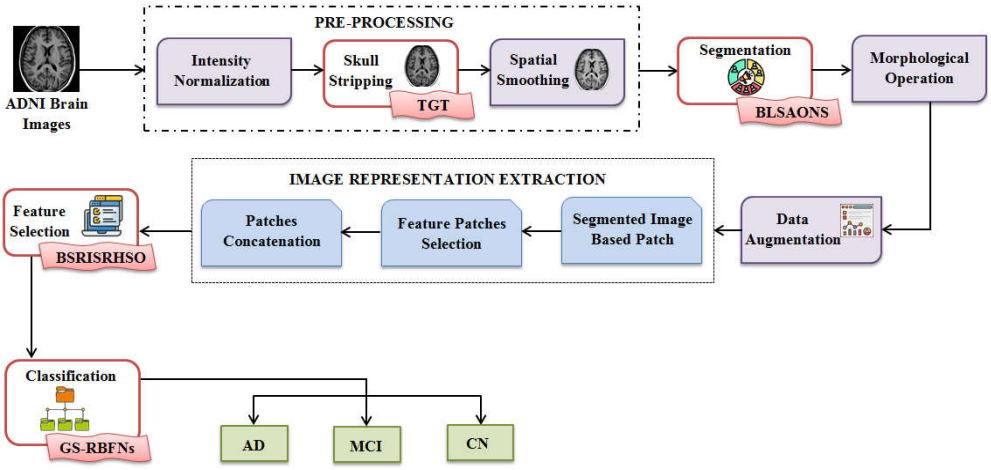

Figure 3.1: Structural representation of the proposed system

3.2.1 Data Acquisition

Primarily, from the publicly available dataset, the input brain MRI images are gathered to perform further processes to early detect AD. Here, the ADNI dataset is utilized by the proposed framework to gather brain MRI images, which assess AD biomarkers for clinical trials. Also, from the ADNI dataset, 80% and 20% of the data are utilized for training and testing, correspondingly. Hence, the collected input brain MRI images are illustrated as,

$$\Im^{MRI}{}_{N} = \left\{ \Im^{MRI}{}_{1}, \Im^{MRI}{}_{2}, \Im^{MRI}{}_{3}, \cdots, \Im^{MRI}{}_{n} \right\} \tag{3.1}$$

Where, $N = 1 \rightarrow n$, the collected brain MRI images are indicated as $\Im^{MRI}{}_{N}$, and the total number of collected MRI images is represented as n.

3.2.2 Pre-processing

$\Im^{MRI}{}_{N}$ is processed after the collection of brain MRI images from ADNI to perform pre-processing. Here, the raw MRI images display various variations, such as intensity variation, resolution, and noise, which cover the subtle pathological changes important for accurate AD prediction and classification. Therefore, to improve the MRI brain images' quality, this proposed system includes three pre-processing stages, comprising Intensity Normalization, Skull Stripping, and Spatial

Smoothing. For getting a consistent range of intensities, Intensity Normalization changes the range of voxel as well as pixel intensity values to a referenced scale. Thereafter, for isolating and analyzing the brain tissue accurately, the Skull Stripping process is implemented, which also separates the non-brain structures like the skull and scalp for detecting the changes in the brain, thus causing AD. Finally, a Spatial Smoothing operation is performed for reducing the noise and enhancing the MRI images' Signal-to-Noise-Ratio to identify the structural changes related to AD. Thus, the comprehensive explanation of pre-processing is depicted as follows,

(a) Intensity Normalization

Primarily, the collected brain MRI images $\Im^{MRI}{}_{N}$ are given as input to the intensity normalization process. Here, the N3 technique is applied to change the voxel as well as pixel intensity values to get the referenced scale images. To detect the structural changes related to AD, this technique improves the image consistency and enhances the quantitative analysis accuracy by correcting the non-uniform intensity variations effectively. Also, by capturing the smooth intensity distortions, this standardization enhanced the image consistency based on exhibiting the bias field across the image. Therefore, the steps included in the N3 technique are exemplified as,

Step 1: Primarily, the intensity values from each MRI image in $\Im^{MRI}$ are represented as ξ^{I} to normalize the intensity, which is depicted as,

$$\xi_{V}^{I}\left(\Im^{MRI}\right)=\left\{\xi_{1}^{I},\ \xi_{2}^{I},\ \xi_{3}^{I},\ \cdots,\ \xi_{v}^{I}\right\} \tag{3.2}$$

Where, $V=1\rightarrow v$, the total number of intensity values is depicted as v.

Step 2: Once the intensity values are represented, the threshold intensity value is set as a threshold for intensity normalization. Therefore, the threshold intensity value is explained as,

$$\tau^{th}{}_{t}=\left\{\tau^{th}{}_{1},\ \tau^{th}{}_{2},\ \tau^{th}{}_{3},\ \cdots,\ \tau^{th}{}_{T}\right\} \tag{3.3}$$

Here, $t = 1$ *to* T, the Threshold Value (TV) is represented as τ^{th}, and the total number of TVs is signified as T.

Step 3: Now, for attaining a normalized intensity value, each intensity value ξ^I is divided by the TV τ^{th}, which is mathematically represented as,

$$\partial^{nor}\left(\xi^I\right) = \frac{\xi_V^I}{\tau^{th}_t} \tag{3.4}$$

Where, the normalized intensity value is indicated as $\partial^{nor}\left(\xi^I\right)$.

Step 4: In terms of normalized intensity values $\partial^{nor}\left(\xi^I\right)$, the brain MRI images are reconstructed after normalization, which is elaborated as,

$$\Im^{MRI}{}_N \xrightarrow{\partial^{nor}\left(\xi^I\right)} \Re^{MRI} \tag{3.5}$$

Here, the reconstructed brain MRI images are represented as $\Re^{MRI}$. Further, the detailed illustration of a re-constructed MRI brain image is depicted as,

$$\Re^{MRI}{}_r = \left\{\Re^{MRI}{}_1, \Re^{MRI}{}_2, \Re^{MRI}{}_3, \cdots, \Re^{MRI}{}_R\right\} \tag{3.6}$$

Where, $r = 1 \to R$, and the total number of reconstructed MRI brain images is indicated as R.

Step 5: Now, the N3 technique is applied for addressing the non-uniformity intensity variations in the normalized images by estimating the bias fields, which are represented as,

$$\sigma^{bf} = \frac{\Im^{MRI}{}_N}{\Re^{MRI}{}_R} \tag{3.7}$$

Here, the bias field across the original and reconstructed image is notated as σ^{bf}.

Step 6: The final normalized image is evaluated after the estimation of the bias field by dividing the intensity values with the estimated bias field σ^{bf}, which is elaborated as,

$$\aleph^{N3} = \frac{\xi^{I}}{\sigma^{bf}} \tag{3.8}$$

Where, the normalized MRI brain images after intensity normalization are specified as $\aleph^{N3}$, which is elaborately depicted as,

$$\aleph^{N3}{}_{\mathrm{I}} = \left\{ \aleph^{N3}{}_{1}, \aleph^{N3}{}_{2}, \aleph^{N3}{}_{3}, \cdots, \aleph^{N3}{}_{i} \right\} \tag{3.9}$$

Here, $\mathrm{I} = 1$ *to* i, the total number of normalized MRI brain images after intensity normalization is denoted as i. Now, $\aleph^{N3}$ are transmitted to the next phase of pre-processing called Skull Stripping.

Skull Stripping

The skull stripping step is performed in this phase to remove the non-brain tissue signal, detect abnormalities, and remove the extra tissues from $\aleph^{N3}$. Here, to accurately separate and analyze the brain tissues associated with AD, the TGT technique is applied. The existing global thresholding technique is referred to as a computationally efficient method in image processing for separating objects from the background by choosing a TV. However, the noise in the noisy image changes the shape of the histogram and degrades the distinct valleys between the peaks of the bimodal histogram, affecting the global thresholding technique. Thus, to overcome these limitations, each normalized image $\aleph^{N3}$ is analyzed in this proposed methodology for calculating the tournament maximum and the minimum of the whole array. By dynamically adjusting to local intensity variations, this proposed approach offers high accuracy. Therefore, the step-by-step process of TGT is illustrated as,

- Primarily, the normalized image $\aleph^{N3}$ is represented as a 2D array, which is illustrated as,

$$A\left(\aleph^{N3}\right)_{p,q}=\begin{bmatrix} A_{1.1} & A_{1,2} & \cdots & A_{1,q} \\ A_{2,1} & A_{2,2} & \cdots & A_{2,q} \\ \vdots & \vdots & \ddots & \vdots \\ A_{p,1} & A_{p,2} & \cdots & A_{p,q} \end{bmatrix} \tag{3.10}$$

Where, a normalized image's array matrix is exemplified as $A\left(\aleph^{N3}\right)_{p,q}$, p and q depicts the row as well as column of an array matrix.

- Further, from the array matrix $A\left(\aleph^{N3}\right)_{p,q}$, the tournament maximum value is calculated, which is determined by comparing every pixel intensity with the other pixel intensity. Hence, the tournament maximum calculation is done by using the following expression,

$$\delta^{tm}{}_{\max}=MAX\left[A_{p,q}\right] \tag{3.11}$$

Here, the calculated tournament maximum values are represented as $\delta^{tm}{}_{\max}$. This tournament maximum value renders the global maximum by representing the highest intensity values across the normalized image.

- Likewise, the tournament minimum value is computed by utilizing the following mathematical representation,

$$\delta^{tm}{}_{\min}=MIN\left[A_{p,q}\right] \tag{3.12}$$

Where, the calculated tournament minimum values, which also provide global minimum, are depicted as $\delta^{tm}{}_{\min}$.

- Now, for removing the skull from an image, the optimal TV is determined, which is computed by calculating the mean of the tournament's maximal and minimal values. This can be depicted as,

$$\mu^{tm}=\frac{\delta^{tn}{}_{\max}}{2}+\frac{\delta^{tn}{}_{\min}}{2} \tag{3.13}$$

Here, the mean of the tournament's maximal and minimal values is indicated as μ^{tm}. The optimal TV is selected based on the mean value and is represented by τ^{op}.

- According to the selected TV, the intensity of the pixels above and below the TVs is considered as a part of the brain tissue and non-brain tissues, respectively.

$$\delta^{\aleph} = \begin{cases} \xi^{I} > \tau^{op} & ; brain\, tissues \\ \xi^{I} < \tau^{op} & ; skull\, region \end{cases} \tag{3.14}$$

- Finally, the skull-stripped images $\left(\delta^{\aleph}\right)$ are obtained based on the above condition by removing the skull effectively from the normalized image. The skull-stripped images can be illustrated as,

$$\vartheta^{\aleph}{}_{s} = \left\{\vartheta^{\aleph}{}_{1}, \vartheta^{\aleph}{}_{2}, \vartheta^{\aleph}{}_{3}, \cdots, \vartheta^{\aleph}{}_{S}\right\} \tag{3.15}$$

Where, $s = 1 \rightarrow S$, the total number of skull-stripped MRI brain images is signified as S. These skull-stripped images are given to the next process of pre-processing termed spatial smoothing.

(b) Spatial Smoothing

In this phase, spatial smoothing is achieved for each skull-stripped image $\vartheta^{\aleph}{}_{s}$ for reducing the noise in the image and enhancing the image's quality. Here, the spatial smoothing is carried out by utilizing the neighborhood averaging method that replaces every pixel value with its neighboring pixels' average value. This averaging technique provides the image with blurred sharp transitions. Also, it eliminates the impact of random noise. Moreover, for blurring and noise reduction, the spatial smoothing is applied. This blurring process offers a uniform appearance with little intensity variations, thus attaining robust and reliable image representations. Thus, spatial smoothing is applied to each skull-stripped image for getting pre-processed images concerning removing the noises. Then, the obtained pre-processed image is represented as,

$$\mathcal{G}^{N}{}_{s} \xrightarrow{Neighborhood\ Averaging} \zeta^{PP} \tag{3.16}$$

Where, the pre-processed image is illustrated as ζ^{PP}. When compared to the original skull-stripped images, these images contain low noise levels and high smoothness. Afterward, for further processing, the pre-processed images ζ^{PP} are fed to the next step to accurately detect and classify AD.

3.2.3 Segmentation

The segmentation process starts with the pre-processed MRI brain images ζ^{PP} to segment those images based on the intensity ranges of the objects. Here, utilizing the BLSAOWS approach, the pre-processed images are segmented, which segments the images into three important brain tissues, namely White Matter (WM), Grey Matter (GM), and CSF. Now, by using the BLSAO algorithm, the optimal TVs are selected, minimizing the segmentation errors by balancing the intra-class and inter-class variances. The effective method for identifying the object boundaries by watershed ridgelines with intensity gradients in an image is referred to as the conventional Watershed Transform (WT). Nevertheless, the major drawback of this model is that it produces over-segmentation. This limitation often occurs owing to the high sensitivity to minor variations in intensity, thus resulting in the division of regions into smaller segments, which do not resemble distinct objects. To overcome the above issue, the BLSAO algorithm is used by this proposed algorithm, which selects the optimal TVs based on the characteristics of images to ensure the segmentation boundaries. In addition, this approach diminishes the over-segmentation problem by minimizing the unnecessary partitions. Moreover, to select the optimal TVs, the prevailing Archimedes Optimization Algorithm (AOA) is also employed, which also offers significant benefits in fine-tuning segmentation parameters. Yet, due to the lack of tuning the parameters carefully, AOA has convergence issues. Hence, to conquer this limitation, the WT approach is incorporated with the AOA technique, which aids in improving segmentation outcomes by offering the ability to adjust TVs based on image characteristics. Also, these techniques assist in enhancing the accuracy and clinical relevance of brain image segmentation tasks to detect and

classify AD. Further, the steps involved in the WT-based segmentation process are examined as follows,

♣ Primarily, each pre-processed image's gradient is calculated to highlight the edges and transitions in intensity, which can be illustrated as,

$$Gr(a,b)=\left[\left(\zeta^{PP}\right)_a+\left(\zeta^{PP}\right)_b\right]^{1/2} \tag{3.17}$$

Where, the gradients of the pixel coordinates (a,b) are indicated as $Gr(a,b)$.

♣ After that, the markers are created centered on the calculated gradient using the optimal TV. This optimal TV is determined utilizing the BLASO technique. The threshold selection is optimized by this algorithm using the histogram intensity variations from the gradient image. The pre-processed image is initialized as the populace and is signified in the following representation,

$$\Re^j=\wp_{low}^j+d*\wp_{upp}^j-d*\wp_{low}^j \tag{3.18}$$

Here, $j=1\ to\ PP$, the PP population's j_{th} object is specified as $\Re^j$, the lower along with upper bounds of the search space are shown as $\wp_{low}$ and $\wp_{upp}$, and the D dimensional vector is signified as d.

♣ Now, by using a random vector, the population's density and volume are initialized and is illustrated by the following expression,

$$\varsigma_{den}=d=\varsigma_{vol} \tag{3.19}$$

Where, the density of the population is indicated as ς_{den} and the volume of the population is notated as ς_{vol}. Further, the acceleration of the objects is initialized by the following mathematical depiction,

$$\varsigma_{acc}^j=\wp_{low}^j+\left|d*\wp_{upp}^j-d*\wp_{low}^j\right| \tag{3.20}$$

Here, the j^{th} object's acceleration is represented as ς_{acc}^{j} .

→ Once the parameters are initialized, the fitness is computed centered on the segmentation efficacy for updating the density's position and the population's volume. The maximum segmentation efficiency is referred to as the fitness, and the fitness can be calculated by using the following mathematical formulation,

$$\xi^{fit} = \max\left|\mathrm{Y}_{seg}\right| \tag{3.21}$$

Where, the fitness is signified as ξ^{fit} , and the segmentation efficiency is depicted as Y_{seg} .

→ Then, the density along with the volume of the markers are updated based on the obtained fitness values, which include a Brownian Motion (BM) term to introduce randomness and prevent premature convergences. Here, the optimal fitness values are analyzed and allocated as the optimal position, optimal acceleration, optimal density, and optimal volumes. Then, based on the optimal density values, the density is updated, which is depicted by the following expression,

$$\varsigma_{den}^{j}[i+1] = \varsigma_{den}^{j}[i] + \left(\upsilon^{ran} * \varsigma_{den}^{BEST}\right) - \left(\upsilon^{ran} * \varsigma_{den}^{j}[i]\right) \tag{3.22}$$

Here, the updated density of the j^{th} object in the iteration $i+1$ is illustrated as $\varsigma_{den}^{j}[i+1]$, and the updated volume of the j^{th} object is expressed by using the following equation,

$$\varsigma_{vol}^{j}[i+1] = \varsigma_{vol}^{j}[i] + \left(\upsilon^{ran} * \varsigma_{vol}^{BEST}\right) - \left(\upsilon^{ran} * \varsigma_{vol}^{j}[i]\right) \tag{3.23}$$

Where, the updated volume of the j^{th} object in the iteration $[i+1]$ is displayed as $\varsigma_{vol}^{j}[i+1]$, and the randomly selected numbers determined using the BM is indicated

as υ^{ran}. Here, to reduce the convergence problem, the random numbers are selected based on the BM. Then, the BM can be depicted as follows,

$$d\upsilon_t^{ran} = con_1 \cdot \upsilon_t^{ran} + con_2 \cdot \mathrm{B}_t^{mot} \tag{3.24}$$

Here, the constants are demonstrated as con_1 and con_2, and the BM is notated as B_t^{mot}.

→ The transfer operator and density factor are applied after updating the population's density and volume. The transfer operator is utilized for facilitating the transformation of the search space from an exploratory to an exploitative phase. It is also applied to the object for reaching the equilibrium state, and the transfer operator can be represented by the following expression,

$$\aleph^{TF} = \exp\left[\frac{i}{i_{\max}} - 1\right] \tag{3.25}$$

Where, the maximum iteration is indicated as $i_{\max}$, and the transfer operator, which increased exponentially with time until a value of 1 is reached, is demonstrated as $\aleph^{TF}$.

→ Now, to search the space as of the global to the local search, the density factor is estimated. The density factor also decreases with time and can converge in previously identified regions.

$$\aleph^{DF}[i+1] = \exp\left[\frac{i}{i_{\max}} - 1\right] - \exp\left[\frac{i}{i_{\max}}\right] \tag{3.26}$$

Here, the density decreasing factor with time is exemplified as $\aleph^{DF}[i+1]$. Next, the occurrence of collision is analyzed to perform exploration and exploitation phases, which is represented by the following expression,

$$\aleph^{TF} = \begin{cases} \aleph^{TF} \le 0.5 & ; colision occurs \\ \aleph^{TF} > 0.5 & ; no colision occurs \end{cases} \tag{3.27}$$

→ The exploration phase is performed based on the utilization of the transfer operator and density factor to update the acceleration of an object in iterations by analyzing the collisions. Based on the values obtained from the transfer order, the occurrence of the collision is analyzed. Here, the collision happens betwixt objects when $\aleph^{TF} \le 0.5$, thus updating an object's acceleration. This updated acceleration aids in selecting the random materials of volume, density, and acceleration. Hence, the mathematical expression for updating the object's acceleration is illustrated as,

$$\varsigma_{acc}^{j}[i+1] = \frac{1}{\varsigma_{den}^{j}[i+1]} * \frac{1}{\varsigma_{vol}^{j}[i+1]} \left| \sum \varsigma_{den}^{ran} \cdot \varsigma_{vol}^{ran} \cdot \varsigma_{acc}^{ran} \right| \tag{3.28}$$

Where, the updated acceleration of an object is specified as $\varsigma_{acc}^{j}[i+1]$, and the random material of density, volume, and acceleration are depicted as ς_{den}^{ran}, ς_{vol}^{ran}, and ς_{acc}^{ran}, respectively. Thereafter, the exploration is ensured up to $\Gamma \le 0.5$ with $\frac{1}{3}^{rd}$ of iteration other than 0.5, thus altering the exploration to the exploitation phase.

→ Now, based on the transfer operator value, no collision occurs if $\Gamma > 0.5$. Therefore, the object's acceleration is updated by including the best density, volume, and acceleration values. It can be articulated by the following expression,

$$\varsigma_{acc}^{j}[i+1] = \frac{\varsigma_{vol}^{j}[i+1]}{\left(\varsigma_{den}^{j}[i+1]\right)^2} * \frac{\varsigma_{den}^{j}[i+1]}{\left(\varsigma_{vol}^{j}[i+1]\right)^2} \left[\sum \varsigma_{den}^{BEST}, \varsigma_{vol}^{BEST}, \varsigma_{acc}^{BEST} \right] \tag{3.29}$$

Here, the best density, volume, and acceleration of an object are represented as ς_{den}^{BEST}, ς_{vol}^{BEST}, and ς_{acc}^{BEST}, respectively.

→ The normalization process is carried out after updating the acceleration of an object to compute the percentage of changes in an object's acceleration. This process can be performed by computing the portion of variations centered on assessing the minimum acceleration and maximum acceleration of an object using log functions, which is illustrated by using the following representation,

$$\Im\varsigma_{acc}^{j}[i+1]=\log\left(\frac{\varsigma_{acc}^{j}[i+1]}{\min|\varsigma_{acc}|}\right)-\log\left(\frac{\max|\varsigma_{acc}|}{\min|\varsigma_{acc}|}\right) \tag{3.30}$$

Where, the normalized acceleration of an object is notated as $\Im\varsigma_{acc}^{j}[i+1]$, the maximum acceleration is illustrated as $\max|\varsigma_{acc}|$, and the minimum acceleration is exhibited as $\min|\varsigma_{acc}|$.

→ Now, if $\Gamma > 0.5$, then every single position of the j^{th} object in $i+1$ is updated by analyzing the normalized acceleration of an object. This can be illustrated by the following formulation,

$$IP^{j}[i+1]=IP^{j}[i]\left\{1+con_3 * \upsilon^{ran}\times\Im\varsigma_{acc}^{j}[i+1]\cdot\aleph^{DF}\times\left|\frac{IP_{ran}}{IP^{j}[i]}-1\right|\right\} \tag{3.31}$$

Here, the individual position is signified as $IP^{j}[i]$, the constant value is depicted as con_3, and the random material of an object is illustrated as IP_{ran}.

→ Further, the individual position based on the best position is updated by utilizing the following mathematical depiction,

$$IP^{j}[i+1]=IP^{BEST}[i+1]+\Gamma_{fdm}+con_4\times\upsilon^{ran} * \Im\varsigma_{acc}^{j}[i+1]\cdot\aleph^{DF}\times IP^{BEST}[i]\left|t-\frac{IP^{j}[i]}{IP^{BEST}[i]}\right| \tag{3.32}$$

Where, the flag for changing the direction of motion is signified as Γ_{fdm}.

→ Finally, for accurate brain image segmentation, each object's objective function is calculated, and the best threshold is obtained. Further, the obtained TVs are considered as markers, which is elaborated by the following expression,

$$\tau^{th} \Leftrightarrow \mathrm{M}_{n^m}^{mar} = \left\{ \mathrm{M}_1^{mar}, \mathrm{M}_2^{mar}, \mathrm{M}_3^{mar}, \cdots, \mathrm{M}_{N^M}^{mar} \right\} \tag{3.33}$$

Here, $n^m = 1 \; to \; N^M$, the TV is signified as τ^{th}, the marker is illustrated as M^{mar}, and the total number of selected markers is depicted as N^M.

♣ The regional markers are labeled centered on the chosen markers. Subsequently, the regional markers' labeling is expressed by the following expression,

$$\Re_{reg}^{r} = \left\langle \Re_{reg}^{1}, \Re_{reg}^{2}, \Re_{reg}^{3}, \cdots, \Re_{reg}^{r^r} \right\rangle \tag{3.34}$$

Where, $r = 1 \; to \; r^r$, the regional marker is represented as $\Re_{reg}$, and the maximal number of regional markers is indicated as r^r.

♣ Subsequently, the distance betwixt the selected maximal markers and regional markers is calculated, and the closest pixels are flooded up to the obtained maximal marker value. Then, the distance is computed as shown below,

$$\varphi^{dis}\left[\mathrm{M}_{n^m}^{mar}, \Re_{reg}^{r^r}\right] = \left\langle \sum \left| \max\left(\mathrm{M}_{n^m}^{mar}\right) - \Re_{reg}^{r^r} \right|^2 \right\rangle^{1/2} \tag{3.35}$$

Here, the distance betwixt the selected maximal markers and the regional markers is notated as $\varphi^{dis}\left[\mathrm{M}_{n^m}^{mar}, \Re_{reg}^{r^r}\right]$.

♣ Lastly, all pixels have a distance value and each pixel is positioned by the close regional marker. After locating the pixel, the pixels' similar value is merged. Thereafter, the WM, GM, and CSF tissues are partitioned centered

on identical pixels. Then, the partitioned images are represented by the following expression,

$$X_{ss}^{\zeta} = \left| X_{1}^{\zeta}, X_{2}^{\zeta}, X_{3}^{\zeta}, \cdots, X_{z^{\xi}}^{\zeta} \right| \tag{3.36}$$

Where, $ss = 1$ *to* s^{s}, the segmented image is represented as X^{ζ}, and the total number of segmented images is illustrated as s^{s}. Figure 3.2 depicts the pseudo-code for the proposed BLSAOWS technique.

Input: Pre-processed images ζ^{PP}

Output: Segmented images X^{ζ}

Begin

Initialize $Gr(a,b), \Re^{j}, \xi^{fit}$, iteration (ϕ), and maximum iteration $(\phi_{\max})$,

Set $(\phi = 1)$

While $(\phi_{\max} \le \phi)$

For each ζ^{PP} do

Calculate the gradients

Initialize the population

$$\Re^{j} = \wp_{low}^{j} + d * \wp_{upp}^{j} - d * \wp_{low}^{j}$$

Estimate the fitness function

$$\xi^{fit} = \max\left| Y_{seg} \right|$$

Update the density and volume

Apply transfer operator and density factor

$$\aleph^{TF} = \exp\left[\frac{i}{i_{\max}} - 1\right] \qquad \text{\#transfer operator}$$

$$\aleph^{DF}[i+1] = \exp\left[\frac{i}{i_{\max}} - 1\right] - \exp\left[\frac{i}{i_{\max}}\right] \qquad \text{\#density factor}$$

If $\left(\aleph^{TF} \le 0.5\right)$

{

Update the acceleration value

{

$$\varsigma_{acc}^{j}[i+1] = \frac{1}{\varsigma_{den}^{j}[i+1]} * \frac{1}{\varsigma_{vol}^{j}[i+1]} \left| \sum \varsigma_{den}^{ran} \cdot \varsigma_{vol}^{ran} \cdot \varsigma_{acc}^{ran} \right|$$

}

Normalized the acceleration values

{

$$\Im\varsigma_{acc}^{j}[i+1] = \log\left(\frac{\varsigma_{acc}^{j}[i+1]}{\min|\varsigma_{acc}|}\right) - \log\left(\frac{\max|\varsigma_{acc}|}{\min|\varsigma_{acc}|}\right)$$

}

}

Else If $\left(\aleph^{TF} > 0.5\right)$

{

Update the acceleration value

{

#No collision occurs

$$\varsigma_{acc}^{j}[i+1]=\frac{\varsigma_{vol}^{j}[i+1]}{\left(\varsigma_{den}^{j}[i+1]\right)^{2}}*\frac{\varsigma_{den}^{j}[i+1]}{\left(\varsigma_{vol}^{j}[i+1]\right)^{2}}\left[\sum\varsigma_{den}^{BEST},\varsigma_{vol}^{BEST},\varsigma_{acc}^{BEST}\right]$$

}

Update the position based on IP_{ran}

$$IP^{j}[i+1]=IP^{j}[i]\left\{1+con_{3}*\upsilon^{ran}\times\Im\varsigma_{acc}^{j}[i+1]\cdot\aleph^{DF}\times\left|\frac{IP_{ran}}{IP^{j}[i]}-1\right|\right\}$$

Estimate the position in terms of IP^{BEST}

$$IP^{j}[i+1]=IP^{BEST}[i+1]+\Gamma_{fdm}+con_{4}\times\upsilon^{ran}*\Im\varsigma_{acc}^{j}[i+1]\cdot\aleph^{DF}\times IP^{BEST}[i]\left|t-\frac{IP^{j}[i]}{IP^{BEST}[i]}\right|$$ **End If**

Calculate the distance between M^{mar} and $\Re_{reg}$

$$\varphi^{dis}\left[\mathrm{M}_{n^{m}}^{mar},\Re_{reg}^{r^{r}}\right]=\left\langle\sum\left|\max\left(\mathrm{M}_{n^{m}}^{mar}\right)-\Re_{reg}^{r^{r}}\right|^{2}\right\rangle^{1/2}$$

End For

End While

Return: $\mathrm{X}_{ss}^{\zeta}=\left|\mathrm{X}_{1}^{\zeta},\mathrm{X}_{2}^{\zeta},\mathrm{X}_{3}^{\zeta},\cdots,\mathrm{X}_{z^{z}}^{\zeta}\right|$

End

Figure 3.2: Pseudo-code for the proposed BLSAOWS technique

Afterward, the total segmented images are given to the next phase of AD classification.

3.2.4 Morphological Operation

Here, the segmented images X^{ζ} are processed for morphological operation to remove the imperfection present in those images. A wide set of image processing operations processing the images centered on the shapes through the application of a

structuring element to an input image and the creation of an output image of the same size is referred to as morphology. The morphological operation is carried out in the proposed framework through dilation, erosion, opening, and closing operations based on 2 main parts, such as input image as well as a structuring element.

* **Dilation**

Initially, the dilation process is carried out on each segmented image X^{ζ} to improve visibility and fill the minor gaps within them. The pixels are added to the boundaries depending on the structuring elements' size and shape, thereby aiding in enhancing visibility. The output pixel value is based on the neighborhood pixels' maximal value. Thereafter, the dilation process can be articulated by the following expression,

$$\left|X^{\zeta}\Theta^{DO}\vartheta_{SE}\right| = \max\left(X^{\zeta}\left(po_1 + po_2\right); X^{\zeta}\left(po_3 + po_4\right) \middle| \left[po_2, po_4\right] \in \vartheta_{SE}\right) \tag{3.37}$$

Where, the dilation operation is indicated as Θ^{DO}, the structuring element is illustrated as ϑ_{SE}, and the points are depicted as po.

* **Erosion**

An erosion step takes place after the dilation process to eliminate the small objects by leaving behind only important objects. This process filters out an image's pixels based on the structuring element. Here, the output pixel is grounded on the minimal value of all closest pixels. The erosion process is explained by using the following expression,

$$X^{\zeta}\Theta^{EO}\vartheta_{SE} = \min\left(X^{\zeta}\left(po_1 + po_2\right); X^{\zeta}\left(po_3 + po_4\right) \middle| \vartheta_{SE}\right) \tag{3.38}$$

Here, erosion is shown as Θ^{EO}.

* **Opening**

The small objects from the images are removed in this operation to preserve the size and shape of the larger objects. This process initially starts by eroding the image, followed by dilating the image for enhancing the quality of an image. Then, the process of opening is done and is illustrated by the following expression,

$$\Theta^{OO} = \left[\mathrm{X}^{\zeta} \Theta^{EO} \vartheta_{SE} \right] \Theta^{DO} \vartheta_{SE} \tag{3.39}$$

Where, the opening operation can be notated as Θ^{OO}.

* **Closing**

This operation is applied for filling the objects' holes to preserve the objects' size along with shape. Here, the morphological closing operation process is to dilate the image and further dilate the eroded image. Then, the closing operation is depicted by the following mathematical depiction,

$$\Theta^{CO} = \left[\mathrm{X}^{\zeta} \Theta^{DO} \vartheta_{SE} \right] \Theta^{EO} \vartheta_{SE} \tag{3.40}$$

Here, the closing operation is indicated as Θ^{CO}.

The enhanced segmented image is obtained based on applying the above-mentioned four morphological operations, which is illustrated by the following expression,

$$\mathrm{X}^{\zeta} \xrightarrow{\Theta^{DO}, \Theta^{EO}, \Theta^{OO}, \Theta^{CO}} \chi_{\mathrm{X}^{\zeta}} \tag{3.41}$$

Where, the final enhanced segmented images are signified as $\chi_{\mathrm{X}^{\zeta}}$. After that, the comprehensive explanation of the final enhanced image is expressed as,

$$\chi_{\mathrm{X}^{\zeta}}^{ee} = \left\langle \chi_{\mathrm{X}^{\zeta}}^{1}, \chi_{\mathrm{X}^{\zeta}}^{2}, \chi_{\mathrm{X}^{\zeta}}^{3}, \cdots, \chi_{\mathrm{X}^{\zeta}}^{EE} \right\rangle \tag{3.42}$$

Here, $ee = 1 \; to \; EE$, the maximum number of optimized segmented images is exemplified as EE. Then, after performing morphological operations, the enhanced segmented images are given as input to the next phase named data augmentation.

3.2.5 Data Augmentation

Here, the optimized segmented images $\chi_{X^{\zeta}}$ are provided as input, which learns numerous features with minimum data to generate new transmuted versions of images. The process of generating new, transformed versions of images for enhancing the dataset's diversity and robustness is termed data augmentation. This technique aids in rendering more information regarding the input data through the implementation of several augmentation methods, namely deformation, rotation, flipping, scaling, and cropping. Further, for the accurate classification of AD, the comprehensive explanation of every single data augmentation technique is illustrated below,

Rotation

The technique that provides valuable information with diverse orientation information by introducing angular variations to the image is referred to as rotation. This technique also permits the model to learn the image from various perspectives by rotating images to specific angles. Here, the enhanced segmented image $\chi_{X^{\zeta}}$ is rotated with the angle of 180°,90°, and 60°. Hence, the rotated images are represented by the following representation,

$$\chi_{X^{\zeta}} \Rightarrow \partial^{\chi_{X^{\zeta}}} = \begin{cases} 180^{\circ}\left(\chi_{X^{\zeta}}\right) \\ 90^{\circ}\left(\chi_{X^{\zeta}}\right) \\ 60^{\circ}\left(\chi_{X^{\zeta}}\right) \end{cases} \tag{3.43}$$

Where, the rotated image is specified as $\partial^{\chi_{X^{\zeta}}}$. Then, the rotated image is inputted to the next phase of the data augmentation procedure termed flipping.

Flipping

The extension of the rotation technique that is applied for flipping the images in horizontal and vertical directions to introduce symmetry into the dataset is known as flipping. Also, horizontal and vertical flipping reflect the image across a vertical and

horizontal axis, respectively. Then, the flipped image is obtained by using the following expressions,

$$\ell^{\chi_{X\zeta}} = \left\langle h\left[\chi_{X^{\zeta}}\right], v\left[\chi_{X^{\zeta}}\right]\right\rangle \tag{3.44}$$

Here, the final flipped image is represented as $\ell^{\chi_{X\zeta}}$, the horizontal flipping operations are indicated as h, and the vertical flipping operation is given as v.

Deformation

The process of applying symmetric changes to simulate real-world transformations like stretching and compressing is called deformation. This process involves random displacement of control points in the image and assists in handling the non-linear transformation and geometric distortions, thus improving the quality of an image under varying physical conditions. In addition, this technique starts to process the image by random displacement of the control points in the image. Then, based on those displacements, the interpolation technique is applied to warping the image. Thus, according to those steps, the resulting deformed images are obtained, and the obtained deformed images are represented as,

$$\chi_{X^{\zeta}} \xrightarrow[\upsilon_{dcp};\,\upsilon_{INT}]{} \hbar^{\chi_{X\zeta}} \tag{3.45}$$

Where, the deformed images are denoted as $\hbar^{\chi_{X\zeta}}$, the displaced control points are illustrated as υ_{dcp}, and the interpolation technique is signified as υ_{INT}.

Scaling

This technique, which permits the framework to learn the scale invariance and recognize the objects at different sizes, is the procedure of adjusting the image's size. Here, the images are resized by the scaling factor of $400\times 400\mathrm{T}$. Then, the scaled image is indicated by using the following equation,

$$\chi_{X^{\zeta}} \rightarrow 400\times 400\mathrm{T}\left(\chi_{X^{\zeta}}\right) = \delta^{\chi_{X\zeta}} \tag{3.46}$$

Where, the scaled images are signified as $\delta^{\chi_{X^\zeta}}$.

Cropping

The cropping technique is the process of creating new images by focusing on specific parts and cropping the image's particular portion. This technique assists in providing important regions and features within the image, which are important to classify AD. Thereafter, the cropped image is illustrated by using the following mathematical depiction,

$$\chi_{X^\zeta} \xrightarrow{cropping} \varepsilon^{\chi_{X^\zeta}} \tag{3.47}$$

Here, the cropped image is specified as $\varepsilon^{\chi_{X^\zeta}}$.

Lastly, to form a set of augmented or final augmented images, the output obtained from the data augmentation techniques, such as rotation, flipping, deforming, scaling, and cropping are combined. This can be illustrated by the following expression,

$$A^{\chi_X} = \begin{bmatrix} \partial^{\chi_{X^\zeta}} \\ \ell^{\chi_{X^\zeta}} \\ \hbar^{\chi_{X^\zeta}} \\ \delta^{\chi_{X^\zeta}} \\ \varepsilon^{\chi_{X^\zeta}} \end{bmatrix} \tag{3.48}$$

Where, the final augmented images are represented as A^{χ_X} . Then, for the accurate classification of AD, the augmented images are inputted into the image representation extraction process.

3.2.6 Image Representation Extraction

The augmented images are processed in this step for the extraction of image representation based on segmented image-based patch extraction, feature patch selection, and patch concatenation. This process aids in extracting the information about images for the accurate classification of AD. For extracting the regions with

rich feature information for feature learning, this process starts by extracting the anatomical feature patches of 15 × 15 × 15 as of the augmented image with every anatomical landmark as the center. This can be represented by using the following representation,

$$\gamma_{afp} = \mathrm{A}^{\chi_{\mathrm{X}}} \left| \upsilon_1, \upsilon_2, \upsilon_3 \right| \tag{3.49}$$

Here, the extracted feature patches are specified as γ_{afp}, and the anatomical landmarks are exemplified as υ_1, υ_2 and υ_3 .

Now, the Pearson correlation matrix betwixt the feature patches is computed after the extraction of feature patches. It is noted that patches that have less correlation with the patches in other clusters are excluded for ensuring the diversity of the features and avoiding a large number of redundant features. Further, the Pearson correlation between the feature patches is calculated by utilizing the following formula,

$$\mathrm{P}^{PCC}\left[\gamma_{afp}^{1}, \gamma_{afp}^{2}\right] = \left(\frac{\varpi^{\mathrm{cov}} \left| \gamma_{afp}^{1}, \gamma_{afp}^{2} \right|}{\sigma^{sd} \left| \gamma_{afp}^{1} \right|^{2} * \sigma^{sd} \left| \gamma_{afp}^{2} \right|^{2}} \right) \times \left[\sigma^{sd} \left| \gamma_{afp}^{1} \right| * \sigma^{sd} \left| \gamma_{afp}^{2} \right| \right] \tag{3.50}$$

Where, the Pearson correlation betwixt the feature patches is indicated as $\mathrm{P}^{PCC}\left[\gamma_{afp}^{1}, \gamma_{afp}^{2}\right]$, the covariance is notated as ϖ^{cov}, and the standard deviation is shown as σ^{sd} .

In the meantime, to avoid the larger area overlap betwixt adjacent patches, the patches with large p-value landmarks are excluded. 22 patches are extracted based on the landmarks. Lastly, the structural changes of numerous regions in the brain are interconnected. Thus, for obtaining the feature landmarks, the correlated patches are chosen and concatenated and are signified as,

$$\lambda_{FP}^{f_f} = \left| \lambda_{FP}^{1}, \lambda_{FP}^{2}, \lambda_{FP}^{3}, \cdots, \lambda_{FP}^{F_f} \right| \tag{3.51}$$

Here, $f^{f} = 1, 2, 3, \cdots, F_{f}$, the concatenated feature patches are indicated as λ_{FP}, and the total number of feature patches is illustrated as F_{f}. The features are extracted centered on the analysis of these concatenated feature patches, which are elaborated as follows,

3.2.7 Feature Extraction

Once the image representations λ_{FP} are extracted, the features are extracted to accurately classify AD. Here, using the proposed BSRISRHSO technique, the FE process is conducted by combining the two approaches to identify the best features to accurately classify AD. For the selection of optimal features with minimum iterations, the prevailing Rock Hyraxes Swarm Optimization (RHSW) technique is applied. Nevertheless, this approach suffers from local optimum problems, causing premature convergence and suboptimal FS. Hence, to resolve this limitation, the Base Switch Rule Infimum and Supremum (BSRIS) approach is integrated for selecting the optimum boundary values. Thus, the proposed BSRISRHSO technique assists in selecting the best features for improving the performance of the classifier centered on the selected optimum boundary values. Then, the process of extracting the best feature from the feature patches is illustrated as follows,

$\Leftrightarrow$ Primarily, the Rock Hyrax populace is initialized. Here, the feature patches are considered as the Rock Hyrax. Then, the initialization of feature patches is illustrated by using the following equation,

$$\mathrm{P_O}\left|\lambda_{FP}\right| = \left\{\lambda_{FP}^{1}, \lambda_{FP}^{2}, \lambda_{FP}^{3}, \cdots, \lambda_{FP}^{F_f}\right\} \tag{3.52}$$

Here, the population of the feature patches or the Rock Hyrax is indicated as $\mathrm{P_O}\left|\lambda_{FP}\right|$.

$\Leftrightarrow$ Now, to identify the best fitness as a leader, the fitness value is calculated by analyzing the classification accuracy. Thereafter, the fitness is computed by partitioning the sum of errors by the total number of observations, which is depicted by using the following mathematical expression,

$$\Psi^{FF}[\tau_{CA}] = \frac{1}{\mathrm{O}^{tot}} \cdot \sum_{\tau_{CA}=0}^{\mathrm{O}^{tot}} error(\tau_{CA}) \tag{3.53}$$

Here, the fitness function is signified as Ψ^{FF}, the classification accuracy is represented as τ_{CA}, and the total number of observations is provided as O^{tot}.

⇔ Next, the identified best fitness value is represented as a leader. Then, based on the prior position, the leader's position is updated. Thus, the following equation represents the updated position of the leader.

$$\lambda_{\aleph} = ran \times \tau_{CA} \left| \lambda_{\aleph-1} ; f_f \right| \tag{3.54}$$

Where, the current position of the leader is notated as $\lambda_{\aleph}$, the random number that ranges from 0 to 1 is depicted as ran, and the previous position of the leader is illustrated as $\lambda_{\aleph-1}$.

⇔ Now, the Rock Hyrax group's every member updates the position based on the position of the leader to effectively explore the search space more. Then, the updated position of every member of the rock hyrax group is expressed as follows,

$$\tau_{CA}^{mem+1} = \left| \tau_{CA}^{mem} - \Delta^{CM} \right| \times \left| \tau_{CA}^{mem} + \lambda_{\aleph} \right| \tag{3.55}$$

Here, the updated position of every member of the rock hyrax group is signified as τ_{CA}^{mem+1}, the current position of every member of the rock hyrax group is signified as τ_{CA}^{mem}, and the population's circular movement is illustrated as Δ^{CM}.

⇔ The circular movement around the leader aids in balancing exploration and exploitation, thus allowing for the selection of optimal solutions. Then, by using the trigonometric function, the movement in a circular manner is calculated, which is illustrated by the following equation,

$$\Delta^{CM} = \left\langle \eta_1^2 + \eta_2^2 \right\rangle^{1/2} \tag{3.56}$$

⇔ Now, based on calculating the radius and the angles around the leader, the circulatory system is repeated. Moreover, the population matrix's circular movement is also depicted as,

$$\Delta^{CM} = \left\langle \left| ran_r \cdot \cos(\varphi) \right|^2 + \left| ran_r \cdot \sin(\varphi) \right|^2 \right\rangle^{1/2} \tag{3.57}$$

$$\eta_1 = ran_r \cdot \cos(\varphi) \tag{3.58}$$

$$\eta_2 = ran_r \cdot \sin(\varphi) \tag{3.59}$$

Where, the radius of the circular portion, which is a random number, is illustrated as ran_r , and the angle that ranges from 0 to 360 degrees is exemplified as φ .

⇔ Afterward, the angle is also updated according to the variables' lower and upper bounds to maintain the feasible and optimal search space by using the base rule. Then, the base rule is elaborated by the following equation,

$$\log_{\Xi_{low}} \left[\Xi_{upp} \right] \cdot \log_{\Xi_{upp}} \left[\Xi_{low} \right] = 1 \tag{3.60}$$

Here, the lower and upper bounds of the variables are signified as Ξ_{low} and Ξ_{upp} , respectively.

⇔ Also, the lower and upper bounds have a set of variables, and the set of variables is illustrated by the following expressions,

$$\Xi_{low}^{nl} = \left\{ \Xi_{low}^{1} , \Xi_{low}^{2} , \Xi_{low}^{3} , \cdots , \Xi_{low}^{NL} \right\} \tag{3.61}$$

$$\Xi_{upp}^{mu} = \left\{ \Xi_{upp}^{1} , \Xi_{upp}^{2} , \Xi_{upp}^{3} , \cdots , \Xi_{upp}^{MU} \right\} \tag{3.62}$$

Where, $nl = 1, 2, 3, \cdots, NL$; $mu = 1, 2, 3, \cdots, MU$, the maximum number of low variables and upper-bound variables are illustrated as $NL$and MU, respectively.

⇔ Now, to select the greater lower bound, the infimum is applied. Then, the chosen lower bound, which is higher than any other element in the set of lower bound variables, is depicted in the following formulation,

$$^{s}\Xi_{low} \geq \Xi_{low}^{NL} \tag{3.63}$$

Here, the selected lower bound from the set of variables is indicated as $^{s}\Xi_{low}$.

⇔ Moreover, for the selection of the least upper bound, the supremum is employed. Then, the chosen upper bound, which is lower than any other element in the upper bound variables, is represented in the following mathematical depiction,

$$^{s}\Xi_{upp} \leq \Xi_{upp}^{MU} \tag{3.64}$$

Where, the selected upper bound variable from the set of upper bound variables by using the supremum is notated as $^{s}\Xi_{upp}$.

⇔ Next, the angle is updated based on the selected lower bound and upper bound variables to select the optimal features. This can be explained by the following mathematical equation,

$$\varphi_{+1} = \varphi + \left\{ ^{s}\Xi_{low} ;\ ^{s}\Xi_{upp} \right\} \tag{3.65}$$

Here, the updated position of the angle is signified as φ_{+1}.

⇔ Then, the above-mentioned process is recurrent till the maximal number of iterations is reached; thus, the optimal features are chosen. Also, the chosen optimal features are represented by the following mathematical depiction,

$$\xi_{\Psi}^{b^f} = \left(\xi_{\Psi}^{1}, \xi_{\Psi}^{2}, \xi_{\Psi}^{3}, \cdots, \xi_{\Psi}^{B^F} \right) \tag{3.66}$$

Where, $b^f = 1, 2, 3, \cdots, B^F$, the selected or extracted best features are displayed as ξ_{Ψ}, and the maximum number of extracted features for the accurate classification of

AD is represented as B^F. Figure 3.3 illustrates the pseudo-code for the proposed BSRISRHSO technique.

Input: Feature patches λ_{FP}
Output: Extracted features ξ_{Ψ}
Begin
Initialize $P_O|\lambda_{FP}|$, Ψ^{FF}, Ξ_{itrr}, Ξ_{itrr}, iteration (itr), and maximum iteration (itr_{max})
Set $(itr = 1)$
While $(itr_{max} \leq itr)$
For each λ_{FP} do
Initialize the population
$$P_O|\lambda_{FP}| = \left\{\lambda^1_{FP}, \lambda^2_{FP}, \lambda^3_{FP}, \cdots, \lambda^{F_f}_{FP}\right\}$$
Calculate the fitness value
$$\Psi^{FF}[\tau_{CA}] = \frac{1}{O^{MF}} \cdot \sum_{\tau_{CA}=0}^{O^{MF}} error(\tau_{CA})$$
Update the position of the leader
$$\tilde{\lambda}_N = ran \times \tau_{CA}|\tilde{\lambda}_{N-1} ; f_j|$$
Update the position of the each member
$$\tau^{mem+1}_{CA} = \left|\tau^{mem}_{CA} - \Delta^{CM}\right| \times \left|\tau^{mem}_{CA} + \tilde{\lambda}_{\infty}\right|$$
Estimate the new fitness
Update the angle
If $(new\,fitness \neq previous fitness)$
{
$itr+1$
}
Else
{
Terminate
}
End If
End For
End While
Return: $\xi^{b^f}_{\Psi} = \left(\xi^1_{\Psi}, \xi^2_{\Psi}, \xi^3_{\Psi}, \cdots, \xi^{\theta^F}_{\Psi}\right)$
End

Figure 3.3: Pseudo-code for the proposed BSRISRHSO technique

Subsequently, to accurately classify AD, MCI, and CN disease, the extracted best features are processed.

3.2.8 Classification

Here, to classify AD, MCI, and CN, the extracted optimal features ξ_{Ψ} are given to the GS-RBFN classifier. The conventional RBFNs are known for their flexibility in handling AD classification. However, they face several challenges, such as gradient vanishing and exploding problems, thus affecting the performance of long data sequences. Therefore, to overcome these limitations, GELU and SWISH Activation Functions (AFs) named GS-RBFN are used by the proposed framework, improving

the gradient flow and enhancing the ability of the network to process complex sequences. The proposed GS-RBFN network is designed into 3 layers, namely the input layer, the hidden layer, and the output layer. Figure 3.4 exemplifies the structural diagram for the proposed GS-RBFN approach.

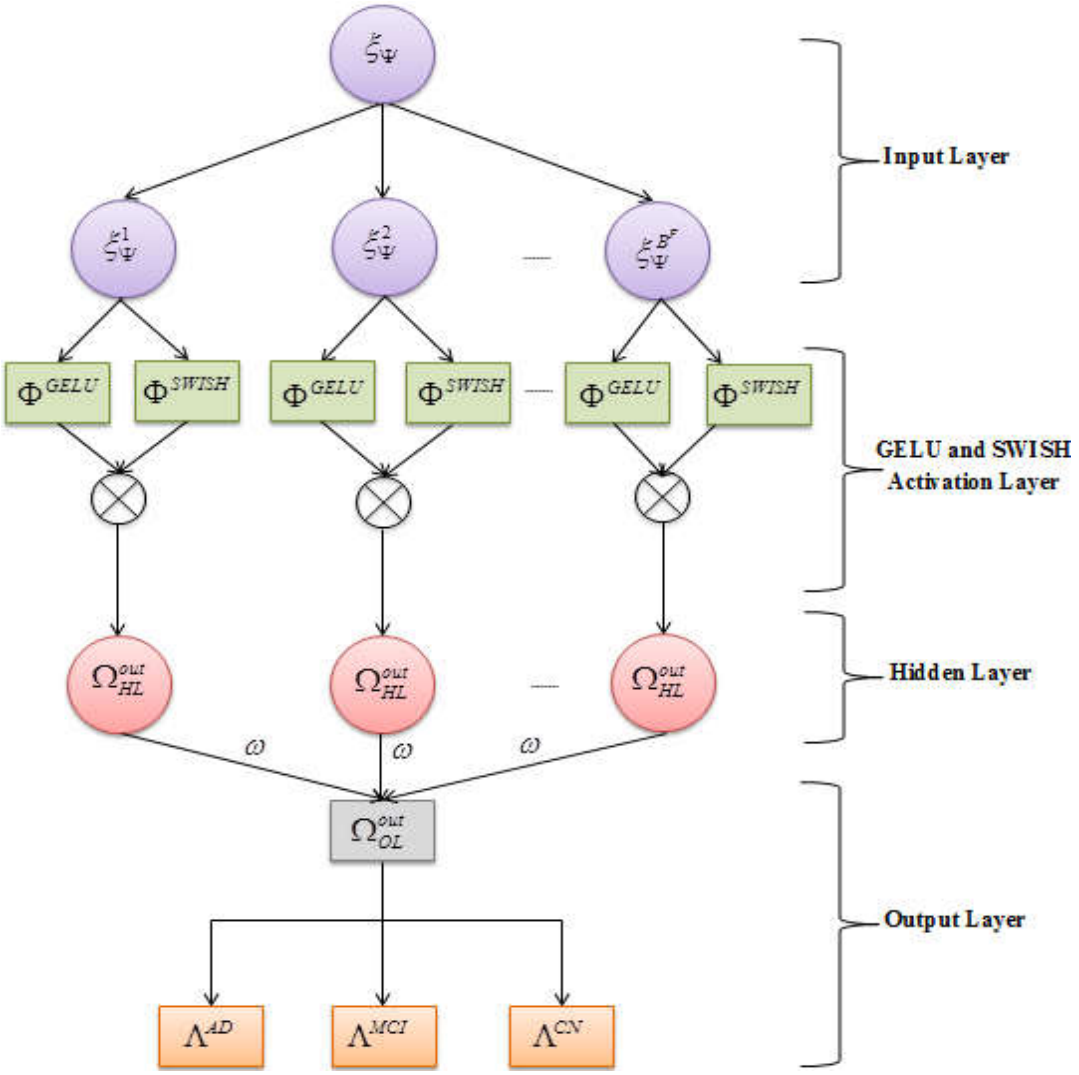

Figure 3.4: Structural diagram for the proposed GS-RBFN technique

Input Layer: Here, the extracted features ξ_{Ψ} are provided to this layer, which receives and passes the data to the hidden layer. This can be illustrated by using the following mathematical formulation,

$$\xi_{\Psi} \rightarrow \Omega_{IL} \xrightarrow{\xi_{\Psi}} \Omega_{HL} \tag{3.67}$$

Where, the input layer is signified as Ω_{IL} and the hidden layer is depicted as Ω_{HL}.

Hidden Layer: The hidden layer accepts the features from the input layer for the accurate classification of AD. The hidden layer encompasses various numbers of neurons, and every neuron is associated with the center point and the radial bias functions.

Now, to improve the gradient flow and enhance the ability of the network in terms of processing complex sequences, the GELU and SWISH AFs are applied. Then, the GELU AF is articulated by using the following mathematical equation,

$$\Phi^{GELU}\left[\xi_{\Psi}\right] = \frac{\xi_{\Psi}}{2} + \frac{\xi_{\Psi}}{2\sqrt{2}}\left|\frac{2}{\sqrt{\pi}}\int_{0}^{\xi_{\Psi}} e^{-t^2} dt\right| \tag{3.68}$$

Here, the GELU AF is indicated as Φ^{GELU}. Thereafter, the SWISH AF is applied for the extraction of best features, which is illustrated by using the following expression,

$$\Phi^{SWISH}\left[\xi_{\Psi}\right] = \xi_{\Psi} \times sigmoid\left[\mathrm{K}\right] \tag{3.69}$$

Where, the SWISH AF is notated as Φ^{SWISH} and the learnable parameter is depicted as K. After the utilization of GELU and SWISH AFs, the hidden layer's output is obtained by computing both GELU and SWISH AFs, which can be explained by the following expression,

$$\Omega_{HL}^{out} = \Phi^{GELU}\left[\xi_{\Psi}\right] * \Phi^{SWISH}\left[\xi_{\Psi}\right] \tag{3.70}$$

Here, the obtained output from the hidden layer is demonstrated as Ω_{HL}^{out}.

Output Layer: Finally, the disease is categorized by the output layer centered on the output value. The output values are obtained by the multiplication of weight values with the AFs, which is elaborated by the following mathematical representation,

$$\mathrm{O}_{values} = \omega \cdot \Omega_{HL}^{out} \tag{3.71}$$

Where, the weight values are indicated as ω and the output values are depicted as O_{values}. Then, based on the obtained output values, the AD is characterized into 3 types, such as AD, MCI, and CN, which is illustrated by the following depiction,

$$\Omega_{OL}^{out} = \begin{cases} \Lambda^{AD} & ; AD \\ \Lambda^{MCI} & ; MCI \\ \Lambda^{CN} & ; CN \end{cases} \tag{3.72}$$

Here, the classified output of the output layer is exemplified as Ω_{OL}^{out}. In Figure 3.5, the pseudo-code for the proposed GS-RBFN technique is depicted.

Input: Extracted features ξ_Ψ
Output: Classified output Ω_{OL}^{out}

Begin
Initialize Ω_{IL}, Ω_{HL}, O_{values}, iteration $(\propto)$, and maximum iteration $(\propto_{max})$
Set $(\propto = 1)$
While $(\propto_{max} \leq \propto)$
For each ξ_Ψ do
Accept the input from the input layer
Apply GELU activation function

$$\Phi^{GELU}\left[\xi_\Psi\right] = \frac{\xi_\Psi}{2} + \frac{\xi_\Psi}{2\sqrt{2}}\left|\frac{2}{\sqrt{\pi}}\int_0^{\frac{\xi_\Psi}{\sqrt{2}}} e^{-t^2}\,dt\right|$$

Utilized SWISH activation function

$$\Phi^{SWISH}\left[\xi_\Psi\right] = \xi_\Psi \times sigmoid[K]$$

Calculate the output from the hidden layer

$$\Omega_{HL}^{out} = \Phi^{GELU}\left[\xi_\Psi\right] * \Phi^{SWISH}\left[\xi_\Psi\right]$$

Evaluate the output values

$$O_{values} = \omega \cdot \Omega_{HL}^{out}$$

Predict the output
End For
End While

Return: $\Omega_{OL}^{out} = \begin{cases} \Lambda^{AD} & ; AD \\ \Lambda^{MCI} & ; MCI \\ \Lambda^{CN} & ; CN \end{cases}$

End

Figure 3.5: Pseudo-code for the proposed GS-RBFN technique

Thus, the proposed model assists in classifying the AD, MCI, and CN accurately by applying appropriate techniques.

3.3 Summary of the Proposed Methodology

In this proposed framework, an efficient technique is implemented to early predict and classify AD using GS-RBFN. Primarily, this methodology begins by collecting the ADNI brain images to early predict and classify AD. After that, centered on intensity normalization, skull stripping, together with spatial smoothing, the collected data are effectively pre-processed. Then, the images are partitioned into WM, GM, and CSF by the proposed BLSAOWS technique. Further, the morphological operations, namely dilation, erosion, opening, and closing operations effectively processed the input images based on the shapes and created the same-sized output image. Next, under several data augmentation techniques like deformation, flipping, scaling, cropping, and rotation of images, the reconstructed images are processed. Through applying these techniques, new transformed versions of images are generated by the proposed approach while providing more important information for the accurate classification of AD. Thereafter, by patch segmentation, feature patch selection, and patch concatenation, the proposed framework efficiently extracted the image representation. The proposed BSRISRHSO technique accurately extracted the features based on the extracted image representations to classify AD, MCI, and CN disease. Lastly, based on utilizing the proposed GELU and SWISH AFs, the proposed GS-RBFN technique successfully detected and classified AD. Hence, by providing appropriate approaches and techniques, the proposed framework offers effective and accurate prediction and classification of AD.

Ethical, Clinical, and Interpretability Considerations: The study uses anonymized data from the ADNI repository following ethical data-use policies. Clinically, the models are intended as decision-support tools to assist physicians rather than replace diagnostic judgment. Interpretability is ensured through saliency and SHAP visualizations that highlight critical brain regions influencing model predictions. These measures promote clinical trust and responsible use of AI in healthcare.

CHAPTER 4

A DOMINANT AD STAGE AND RISK PREDICTION FRAMEWORK USING A TADPOLE DATASET BASED ON TT SELF-WEIGHTED DEEP-AD_3^- NET

4.1 Introduction

Aging relates to cognitive changes characterized by phenotypic diversity in both severity and pace. This diversity is due to numerous biological and lifestyle factors that influence an individual throughout their lifespan (Marinescu et al., 2020). Among these, certain individuals preserve their CF in old age termed super agers, whereas others face a reduction at a younger age owing to ND (Kapoor et al., 2021). In this broad dimension of CF, there will be difficulty in describing the fine line betwixt normal and pathological aging. Furthermore, aging commonly results in cognitive decline, particularly in memory function. Also, it is often related to NDs, such as AD (Mehdipour Ghazi et al., 2021). The most general sort of dementia is AD, which is a progressive disease beginning with mild memory loss and probably causes a decline in the potential to perform conversation and respond to the environment (Ho et al., 2022). In 2020, 5.8 million Americans are living with AD, and the number of individuals living with AD doubles every five years beyond age sixty-five. AD eventually affects brain functions, namely movement, memory, language, behavior, judgment, and abstract thinking (Hernandez et al., 2022).

AD is categorized by 2 abnormalities in the brain, such as APs and Neurofibrillary Tangles (NFTs). APs are found in the tissues betwixt the nerve cells, which are unusual clumps of a protein known as beta-amyloid as well as degenerating bits of neurons and other cells. A bundle of twisted filaments found within neurons is referred to as NFTs (Baytas, 2024). The tangles are mainly made up of a protein named tau. In healthy neurons, these proteins help the microtubules' functioning, while in AD, tau changes the way that causes it to twist into pairs of helical filaments that gather into tangles (Zhao et al., 2023). This failure of the neurons' transport system might impair communication betwixt nerve cells, leading them to die. Hence, enormous effort has been made to identify and develop treatment options, which can terminate this degenerative process at an earlier stage (Song et

al., 2021). Firstly, the cognitive symptoms can be minor, and the conditions are termed MCI, which represents a borderline between normal aging and very early dementia. Nevertheless, not every patient with MCI develops AD (Jung et al., 2021). Even though studies show that a patient with MCI has a tenfold augmented risk of developing AD, a subset of people with MCI remain stable or return to normal functioning. Furthermore, many environmental and genetic risk factors are related to the strongest genetic risk factor for an allele of apolipoprotein. This prediction is made by assessing the AD dataset (Lin et al., 2021).

Identifying the data, features, and methods that are best predictive of the future progression of subjects at risk of AD is the aim of the TADPOLE (Irfan et al., 2024). Accurate prediction of the onset of AD and the longitudinal progression is significant for patient selection and care planning in clinical trials (Muhammed & Thiyagarajan, 2022). Early detection is vital to successfully administrate disease-modifying treatments during the disease's pre-symptomatic phases before extensive brain damage. Several approaches are demonstrated for the prediction of AD-related target variables, leveraging multimodal biomarker data available in AD (Muhammed & Thiyagarajan, 2021). Yet, none of the prevailing works performed variable selection for the calculation of RS as it was impossible to manage; therefore, potential bias on FS was created [(Qu et al., 2021). In addition, the conventional longitudinal techniques centered on statistical regression models that perform target variables' interaction with other known factors, namely cognitive test scores, clinical diagnosis, or time for conversion betwixt diagnoses, which cannot predict the RS, remains unexplored (Prakash et al., 2021). Likewise, in this proposed framework, an AD stage and risk prediction framework by using the TADPOLE dataset and performing the risk assessment based on cognitive test scores and its clinical trials using ADAS-Cogs-13 and its tasks is implemented.

4.2 Proposed Methodology For TT Self-Weighted DEEP-AD_3-NET-BASED AD Stage and Risk Prediction Using Tadpole Dataset

AD is an ND that has the key symptoms of chronic primary memory loss and cognitive impairment. For the prevention of AD, the at-risk states' characterization and AD's timely detection are important. Thus, a dominant AD stage as well as risk

prediction using the TADPOLE dataset is implemented in the proposed framework. Initially, the ADNI TADOLE dataset is examined for computing the RSs, and some variables are extracted by alleviating the noise. After that, to select the crucial variables, the RHCA is applied. Subsequently, they are ranked through the tailored metric ranking approach. Further, the risk prediction score is computed using the TT-SWM and the ventricle volume weight assignment process by employing the relevant variables obtained from the original AD Assessment Scale Cognitive Subscale (ADAS-Cog-13). Then, by using the QBCS methodology, the brain's volume and hippocampus area of an AD-affected person and the rate of shrinkage in the brain are measured. Next, the resting-state functional MRI (rs-fMRI) is employed for the entire brain with the bilateral hippocampus by using the Phylogenetic Method (PM). Here, the bilateral hippocampus features are acquired by creating one GLCM. Then, by using the GA, the features are extracted. Finally, for the classification of AD stages, the features from ranking, risk predicted scores, and the bilateral hippocampus features are fed into the Deep-AD_3-Net classifier, which classified the AD stages into normal, AD-mild, AD-moderate, and AD-severity. Figure 4.1 depicts the structural block diagram for the proposed framework.

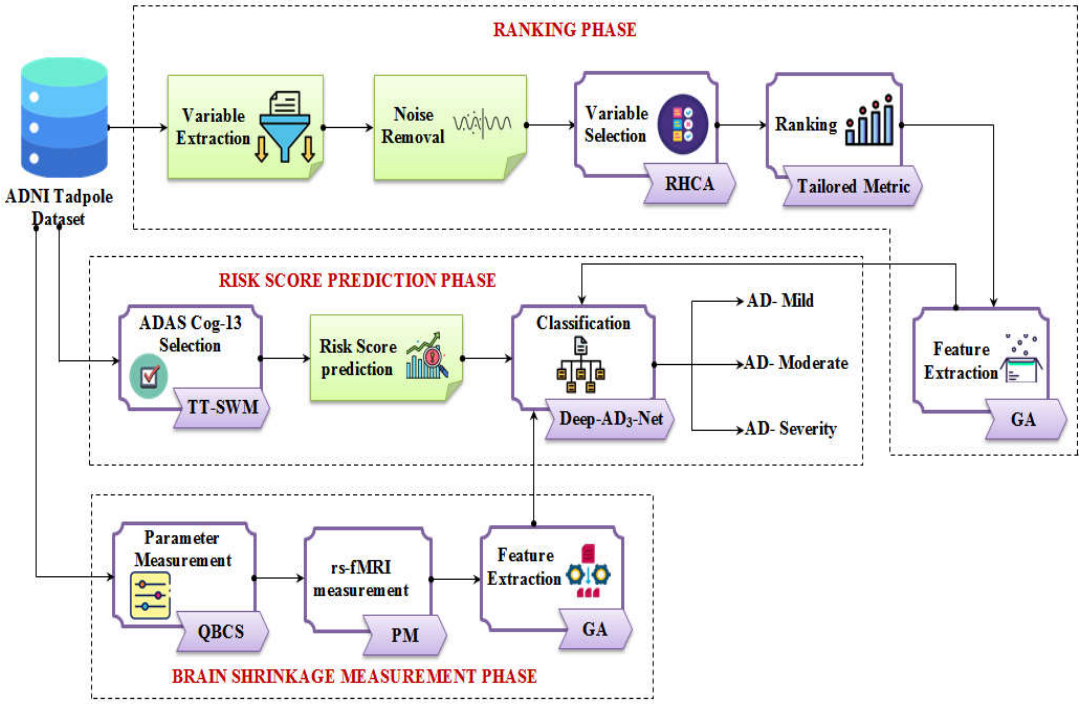

Figure 4.1: Block diagram for the proposed framework

4.2.1 Data Acquisition

Initially, for accurate AD stage classification and AD risk prediction, the ADNI TADPOLE dataset is analyzed with the ADAS-Cog 13 results. The TADPOLE's essence is very simple. It provides a list of individuals recruited priorly to the ADNI. This dataset comprises numerous variables, namely age, gender, education, Intracranial Volume (ICV), whole brain, Hippocampus, Mid-temp, Mid-left, Mid-right, and so on. All these individuals provide data to earlier ADNI studies and have accepted for rendering follow-up data in ADNI 3. Additionally, the TADPOLE challenge participants to use any data freely to inform their predictions. For convenience, TADPOLE provides 3 standard datasets, namely D1, D2, and D3, which are derived from the ADNI study. D1 specifies the comprehensive longitudinal dataset for training, D2 demonstrates the comprehensive longitudinal dataset on rollover subjects to forecast, and finally, D3 depicts the limited forecasting dataset on similar rollover subjects as D2. Further, the data from the given dataset is illustrated in the following expression,

$$\partial_a^{ATD} = \left\{\partial_1^{ATD}, \partial_2^{ATD}, \partial_3^{ATD}, \cdots, \partial_A^{ATD}\right\} \tag{4.1}$$

Where, $a = 1, 2, 3, \cdots, A$, the data from the given ADNI TADPOLE dataset is indicated as ∂^{ATD}, and the maximum number of data is illustrated as A. Now, the collected data from the given ADNI TADPOLE dataset is processed to accurately classify AD stages through three phases, namely ranking, RS prediction, and brain shrinkage measurement.

4.2.2 Ranking Phase

Here, to accurately classify AD stages and risk prediction, some variables are extracted from the rendered ADNI dataset. In this phase, variable extraction, noise removal, variable selection, ranking, and FE are included. A multisite study that uses biomarkers, such as chemicals in the blood, and clinical measures, such as cognitive and neuropsychological tests to evaluate brain functions and structure is termed ADNI. The ADNI clinical dataset comprises clinical information regarding each

subject, containing demographics, cognitive evaluation data, recruitment, and physical examinations. Furthermore, for observing variations in the brain, the ADNI uses neuroimaging techniques like MRI and PET scans. The comprehensive explanation of the ranking phase is given below,

4.2.2.1 Variable Extraction

Here, the variables illustrating the AD's characteristics from the given dataset are extracted. Some of the relevant extracted characteristics for effective AD classification are characteristics like gender, age, brain volume, hippocampus, ICV, mid-temp, mid-right, mid-left, and so on. For the accurate calculation of RSs, this variable extraction is also important. Further, the extracted variables are illustrated by the following representation,

$$\ell_{\text{var}}^{b} = \left[\ell_{\text{var}}^{1}, \ell_{\text{var}}^{2}, \ell_{\text{var}}^{3}, \cdots, \ell_{\text{var}}^{B}\right] \tag{4.2}$$

Where, $b = 1, 2, 3, \cdots, B$, the extracted variable is depicted as ℓ_{var}, and the maximum number of extracted variables is exemplified as B. Now, for the effective classification of AD stages, the extracted variables ℓ_{var} are inputted to the noise removal step.

4.2.2.2 Noise Removal

The unwanted artifacts are removed from the extracted variables for the calculation of the RS and the preservation of information present in the variables. This noise removal process aids in removing all the unwanted noise present in the extracted variables and finding the high-risk areas. Further, the noise-removed variables are represented by using the following mathematical equation,

$$\wp_{c}^{\ell_{\text{var}}} = \left|\wp_{1}^{\ell_{\text{var}}}, \wp_{2}^{\ell_{\text{var}}}, \wp_{3}^{\ell_{\text{var}}}, \cdots, \wp_{C}^{\ell_{\text{var}}}\right| \tag{4.3}$$

Here, $c = 1, 2, 3, \cdots, C$, the variables that are noise-removed to accurately evaluate RSs are notated as $\wp^{\ell_{\text{var}}}$, and the maximum number of noise-removed variables is

signified as C . Now, $\wp^{\ell_{\text{var}}}$ are processed to evaluate an extrapolation of the affected hippocampus as well as mid-cortex areas and the selection of more robust and positive variables by utilizing the RHCA.

4.2.2.3 Variable Selection

After removing the noise from the extracted variables, the variables that are more robust and positive in the affected hippocampus and mid-cortex areas are selected to accurately predict RS. For this purpose, the RHCA technique, which is effective for variable selection, is utilized by the proposed framework. In general, for the selection of strong attributes, the prevailing Correlation Coefficient (CC) technique is applied. Also, by using the CC technique, the strength of relations betwixt data variables is assessed. Here, a CC of +1 indicates the 2 variables that are perfectly connected positively. In addition, the CC of -1 illustrates the 2 variables that are perfectly connected negatively, whereas the CC of 0 signifies that there is no linear relation. Here, only in certain predefined criteria, the CC is acquired. Thus, this technique failed to determine the causality between the 'two' strong attributes. Hence, in the prevailing correlation analysis, the hypothesis testing method is recursively introduced for ascertaining the strong attributes. The hypothesis testing aims to test whether the null hypothesis could be approved or rejected. Further, the modified technique is referred to as RHCA, which effectively selects the respective variables and creates a correlation matrix by leaving the one out of cross-validation. The proposed RHCA method's step-by-step process is demonstrated below,

$\Rightarrow$ Primarily, the variables having stronger attributes are chosen by using the Pearson product-moment CC, which gauges the strength of the linear relation betwixt 2 variables. Also, the collinear relation between the two variables is determined by the covariance and standard deviation determination. Then, the formula for the CC is demonstrated by using the following mathematical equation,

$$\vartheta^{cc}\left[\text{var}_1,\ \text{var}_2\right] = \frac{1}{\sigma^{\text{cov}}\left[\text{var}_1,\ \text{var}_2\right]}\left\{\omega^{sd}\left[\text{var}_1\right]\cdot\omega^{sd}\left[\text{var}_2\right]\right\} \tag{4.4}$$

Where, the CC of two variables var_1 and var_2 is depicted as ϑ^{cc}, the covariance of two variables is indicated as σ^{cov}, and the standard deviation of two variables is notated as ω^{sd}.

$\Rightarrow$ Now, the state of the hypothesis is determined either as a hull or alternated for the strong attribute selection processes. Here, the relationship between the variables is denoted as alternated, and the correlation between the essential attributes is demonstrated as null. This can also be stated by using the following representations.

$$\ell^{re}\left|\text{var}_1, \text{var}_2\right| = \text{H}^{\propto} \tag{4.5}$$

$$\ell^{re}\left|atr_1, atr_2\right| = \text{H}^{0} \tag{4.6}$$

Here, the calculated relationships are illustrated as ℓ^{re}, the required strong attributes are depicted as atr_1 and atr_2, and the null and alternative hypotheses indicating the state of the hypothesis are exemplified as H^0 and $\text{H}^{\propto}$, respectively.

$\Rightarrow$ Next, sampling is performed for obtaining the difference between the two variables. After that, for an efficient testing process, the data needed for the robust attribute selection is also collected. Furthermore, by using the statistical test, the within-group and between-group variances are determined. Further, the statistical test is defined by the following mathematical equation,

$$\zeta_{PV} = \begin{Bmatrix} \sigma^{VAR}(wg) > \sigma^{VAR}(bg) & ;\zeta_{low}^{PV} \\ \sigma^{VAR}(bg) > \sigma^{VAR}(wg) & ;\zeta_{hgh}^{PV} \end{Bmatrix} \tag{4.7}$$

Here, the within-group variance is indicated as $\sigma^{VAR}(wg)$, the between-group variance is depicted as $\sigma^{VAR}(bg)$, the prediction value using a statistical test is illustrated as ζ_{PV}, the low prediction value is signified as ζ_{low}^{PV}, and the high prediction value is demonstrated as ζ_{high}^{PV}.

⇒ Based on the prediction values, the decision is made whether the null hypothesis is selected or rejected. Also, features, such as APs and Cerebral Amyloid Angiopathy (CAA), NFTs, glial responses, ICV, Weighted Error Score (WES), Mean Absolute Error (MAE), and Coverage Probability Accuracy (CPA) are acquired through the correlation matrix, which can be illustrated by using the following mathematical equation,

$$\zeta^{PV} \xrightarrow{\zeta^{CM}} \left\{ f^{apca}, f^{nft}, f^{gr}, f^{icv}, f^{mae}, f^{wes}, f^{cpa} \right\} \tag{4.7}$$

Here, the features like APs and CAA, NFTs, glial response, IC, MAE, WES, and CPA are indicated as $f^{apca}, f^{nft}, f^{gr}, f^{icv}, f^{mae}, f^{wes}$, and f^{cpa}, respectively. The correlation matrix is illustrated as ζ^{CM}, which also indicates the relationship among all the possible pairs of values generated as of the chosen robust variables.

⇒ Furthermore, the CPA is a scheme for the computation of confidence intervals. The confidence intervals are the proportion of the time that the interval comprises the true value of interest. After that, the process is repeated till the causality between the variables is not determined. Further, the selected variables are demonstrated by utilizing the following mathematical equation,

$$\hbar_{SV}^{d} = \left(\hbar_{SV}^{1}, \hbar_{SV}^{2}, \hbar_{SV}^{3}, \cdots, \hbar_{SV}^{D} \right) \tag{4.8}$$

Where, $d = 1, 2, 3, \cdots, D$, the selected variables are demonstrated as $\hbar_{SV}$, and the maximum number of selected variables is signified as D. Now, to accurately classify AD stages and risk prediction of AD, the selected variables are provided for the ranking phase.

4.2.2.4 Ranking

In this phase, the selected variables $\hbar_{SV}$, including the neuropathological hallmarks, such as APs and CAA, NFTs, glial responses, ICV, MAE, WES, and CPA are obtained. By using the tailored metric ranging algorithm, these neuropathological hallmarks are ranked. To rank those neuropathological hallmarks, the Markov Chain technique is applied, which creates samples of continuous random variables, with probability density proportional to a known function. These samples could be utilized for assessing an integral over those variables as its anticipated value or variance. Commonly, a stochastic discrete-time process is also referred to as a random sequence. The assumed values are called the stochastic process's states. The stochastic process's state space is created by the set of all probable values. It is utilized for ranking the specific features extracted as of the dataset at a time called the Markov chain. Then, the steps for the procedure of ranking the neuropathological hallmarks are illustrated as follows,

⇔ Initially, through a transition probability matrix, the Markov chain is determined. A Markov chain's state transition probability matrix offers the probabilities of transitioning from one state to another in a single time unit. It is beneficial for extending to long time intervals. Then, the Markov chain is represented by using the following matrix equation,

$$\mathrm{M}^{mc} = \begin{vmatrix} P_{11} & \cdots & P_{1j} & \cdots & P_{1J} \\ \vdots & \ddots & \vdots & \iddots & \vdots \\ P_{i1} & \cdots & P_{ij} & \cdots & P_{iJ} \\ \vdots & \iddots & \vdots & \ddots & \vdots \\ P_{I1} & \cdots & P_{Ij} & \cdots & P_{IJ} \end{vmatrix} \tag{4.9}$$

Here, $I = 1, 2, 3, \cdots, i$, $J = 1, 2, 3, \cdots, j$, the Markov chain is indicated as M^{mc}, the probability of choosing the ranked features is specified as P, and the maximum number of selected ranked features is illustrated as i and j.

⇔ Once the Markov chain is determined, the probability of the occurrence of the feature at a time t is computed based on the initial probability

distribution and is evaluated using the following mathematical representation,

$$P\left[\hbar_{SV}\right] = P_{INI} \prod_{t_1=1}^{t} \begin{vmatrix} P_{11} & \cdots & P_{1j} & \cdots & P_{1J} \\ \vdots & \ddots & \vdots & \iddots & \vdots \\ P_{i1} & \cdots & P_{ij} & \cdots & P_{iJ} \\ \vdots & \iddots & \vdots & \ddots & \vdots \\ P_{I1} & \cdots & P_{Ij} & \cdots & P_{IJ} \end{vmatrix} \hbar_{SV}^{\,t_1} \tag{4.10}$$

Here, P_{INI} demonstrates the initial probability distribution matrix, which is formulated by using the following mathematical expression,

$$P_{INT} = \left| P_{INT}^{1} \quad P_{INT}^{2} \quad \cdots \quad P_{INT}^{\text{int}} \right| \tag{4.11}$$

Where, the maximum number of probability distribution elements is illustrated as int.

$\Leftrightarrow$ Now, for the accurate classification of AD stages, the Markov chain approach is applied to calculating the ranked variables. This can be illustrated by using the following depiction,

$$\hbar_{SV} \xrightarrow{\text{M}^{mc}} \lambda^{RV} \tag{4.12}$$

Here, the ranked variables are represented as λ^{RV}.

$\Leftrightarrow$ Further, the obtained ranked variables are explained by using the following mathematical equation,

$$\lambda_e^{RV} = \left\langle \lambda_1^{RV}, \lambda_2^{RV}, \lambda_3^{RV}, \cdots, \lambda_E^{RV} \right\rangle \tag{4.13}$$

Here, $e = 1, 2, 3, \cdots, E$, the maximum number of ranked variables is demonstrated as E. During this ranking, the ICV always ranked first. Hence, size variation is examined by correcting for making an approximate differentiation between CN and MCI patients. Thereafter, for the accurate risk prediction and classification of AD stages, the ranked variables are processed.

4.2.2.5 Feature Extraction

The features responsible for effectively classifying AD stages are extracted from the ranked variables λ^{RV}, namely APs and CAA, NFTs, glial responses, ICV, MAE, WES, and CPA. Here, by using the GA technique, the features having 3D dynamic form factor features are extracted. The objective function is directly taken by GA as the fitness function is only used by the search information for evaluating the individual devoid of other complicated derivation and extra information. Furthermore, based on this, the genetic operation is carried out by GA for realizing the information exchange betwixt individuals in the populace. Therefore, GA can extract large volumes of features with good flexibility. Additionally, this technique adopts a multi-point parallel approach to collect features from multipoint. Moreover, the population-based optimization method is applied to evolve the optimized functions or objectives via cooperative and competitive interaction among individuals inspired by the fittest survival behavior. A new populace is generated centered on the genes present in an individual. Then, the proposed GA's comprehensive explanation is discussed below,

↔ Initially, the number of chromosomes or λ^{RV} is integrated with the initial populace. These chromosomes in the d-dimensional search space are randomly initialized. Then, the random initialization of these chromosomes is depicted by using the following equation,

$$\lambda^{RV} = \left\{ g\left(\lambda_1^{RV}, \lambda_2^{RV}, \lambda_3^{RV}, \cdots, \lambda_E^{RV} \right) \right\} \tag{4.14}$$

Where, the number of chromosomes or λ^{RV} is indicated as g. The fitness of every chromosome in the populace is determined based on the fitness calculation.

↔ Now, the prediction accuracy or fitness of every chromosome in the populace is calculated; from the populace, the fittest chromosomes are chosen for further processing. Then, the fitness assessment is formulated by using the following equation,

$$\Gamma_{fit}\left[\lambda^{RV}\right] = \Gamma_{fit} \cdot \lambda_1^{RV}, \Gamma_{fit} \cdot \lambda_2^{RV}, \Gamma_{fit} \cdot \lambda_3^{RV}, \cdots, \Gamma_{fit} \cdot \lambda_E^{RV} \tag{4.15}$$

Here, the fitness function is specified as Γ_{fit} .

↔ Afterward, the selection operation is carried out through the selection of chromosome pairs. Based on the weight factor and the calculated fitness values, probability is evaluated in the selection. Then, the selection probability is assessed by the following mathematical representation,

$$\mathrm{P}^{s}\left\{g^{g}\right\}=\omega_{wf}\cdot\left\langle\Gamma_{fit}\cdot\lambda_{1}^{RV},\Gamma_{fit}\cdot\lambda_{2}^{RV},\Gamma_{fit}\cdot\lambda_{3}^{RV},\cdots,\Gamma_{fit}\cdot\lambda_{E}^{RV}\right\rangle \tag{4.16}$$

Where, the selection probability is represented as P^{s} , the weight factor is notated as ω_{wf} , and the chromosome pair is indicated as g^{g} .

↔ After that, based on the selection probability and the minimum probability of selection, the selection process is carried out by using the following expression.

$$\xi\left(\lambda^{RV}\right)=\frac{\min\left|\Gamma_{fit}\left(\lambda^{RV}\right)\right|\left[\dfrac{\mathrm{P}^{s}\left(g^{g}\right)}{\min\left|\Gamma_{fit}\left(\lambda^{RV}\right)\right|}-1\right]}{\sum_{g^{g}\in\lambda^{RV}}\left|\min\left|\Gamma_{fit}\left(\lambda^{RV}\right)\right|\left[\dfrac{\mathrm{P}^{s}\left(g^{g}\right)}{\min\left|\Gamma_{fit}\left(\lambda^{RV}\right)\right|}-1\right]\right|} \tag{4.17}$$

Here, the selection process is shown as ξ , and the minimum probability of selection is exemplified as $\min\left|\Gamma_{fit}\left(\lambda^{RV}\right)\right|$, which is calculated based on the minimum probability selection of the paired chromosomes. This can be elaborated by using the following mathematical equation,

$$\min\left|\Gamma_{fit}\left(\lambda^{RV}\right)\right|=\min\left(\mathrm{P}^{s}\left(g^{g}\right);\ g^{g}\in\lambda^{RV}\right) \tag{4.18}$$

↔ Once the selection process is estimated, several chromosomes are selected for producing the new strings. Then, the selected chromosomes are depicted by the following depiction,

$$g_{sle}^{G}=g_{sle}^{1},g_{sle}^{2},g_{sle}^{3},\cdots,g_{sle}^{G^{G}} \tag{4.19}$$

Here, $G = 1, 2, 3, \cdots, G^G$, the selected chromosomes are signified as g_{sle}, and the maximum number of selected chromosomes is denoted as G^G.

↔ The new strings are produced based on the chromosomes selected by the selection process. Here, based on the selected chromosomes, the new string is produced by using the crossover operation. Crossover is a genetic operator, which is utilized to vary the programming of chromosomes from one generation to another. This technique is also called recombination and is used for combining the genetic information of two chromosomes to generate new strings. Then, the new strings are formulated by using the following mathematical equation,

$$\xi^{new}\left[\lambda^{RV}\right] = \varsigma_{CO} \cdot g_{sle} \tag{4.20}$$

Where, the new string is represented as ξ^{new}, and the crossover operator is notated as ς_{CO}.

↔ Now, for effective AD stage classification, the new string is examined for the calculation of the optimal solution. The mutation procedure is carried out to evaluate the optimal solutions, which is elaborated by the following equation,

$$\xi^{new}\left[\lambda^{RV}\right] \xrightarrow[\varsigma_{Mop}]{} \vartheta_{EF} \tag{4.21}$$

Here, the mutation producer is indicated as ς_{Mop}, and the set of optimal solutions is demonstrated as ϑ_{EF}. These optimal solutions are regarded as the extracted features. Then, the extracted features to accurately and effectively classify AD stages are elaborated by the following mathematical depiction,

$$\vartheta_{EF}^{h} = \vartheta_{EF}^{1}, \vartheta_{EF}^{2}, \vartheta_{EF}^{3}, \cdots, \vartheta_{EF}^{H} \tag{4.22}$$

Here, the maximum number of extracted features is notated as H. Thereafter, these extracted features are inputted to the classifier for the accurate and effective classification of AD stages. The pseudo-code for the proposed GA is represented in Figure 4.2,

Input: Ranked variables $\grave{\lambda}^{RV}$

Output: Extracted features ϑ_{EF}

Begin

Initialize g, Γ_{fit}, P^{s}, ς_{CO}, ξ^{new}, iteration (itr), and maximum iteration (itr_{max})

Set $(itr = 1)$

While $(itr_{max} \le itr)$

For each $\grave{\lambda}^{RV}$ do

Evaluate fitness function

$$\Gamma_{fit}\left[\grave{\lambda}^{RV}\right] = \Gamma_{fit}\cdot\grave{\lambda}_1^{RV}, \Gamma_{fit}\cdot\grave{\lambda}_2^{RV}, \Gamma_{fit}\cdot\grave{\lambda}_3^{RV}, \cdots, \Gamma_{fit}\cdot\grave{\lambda}_E^{RV}$$

Perform selection probability

$$\mathrm{P}^{s}\left\{g^{\pi}\right\} = \omega_{wf}\cdot\left\langle\Gamma_{fit}\cdot\grave{\lambda}_1^{RV}, \Gamma_{fit}\cdot\grave{\lambda}_2^{RV}, \Gamma_{fit}\cdot\grave{\lambda}_3^{RV}, \cdots, \Gamma_{fit}\cdot\grave{\lambda}_E^{RV}\right\rangle$$

If $\left(\mathrm{P}^{s}\left\{g^{\pi}\right\} = \min\right)$

{

Apply selection process formula

$$\xi\left(\grave{\lambda}^{RV}\right) = \frac{\min\left|\Gamma_{fit}\left(\grave{\lambda}^{RV}\right)\right|\left[\dfrac{\mathrm{P}^{s}\left(g^{\pi}\right)}{\min\left|\Gamma_{fit}\left(\grave{\lambda}^{RV}\right)\right|} - 1\right]}{\sum_{g^{\pi}\in ex^{RV}}\left|\min\left|\Gamma_{fit}\left(\grave{\lambda}^{RV}\right)\right|\left[\dfrac{\mathrm{P}^{s}\left(g^{\pi}\right)}{\min\left|\Gamma_{fit}\left(\grave{\lambda}^{RV}\right)\right|} - 1\right]\right|}$$

}

Else

{

$\xi\left(\grave{\lambda}^{RV}\right) = 0$

}

End If

Construct new string

$$\xi^{new}\left[\grave{\lambda}^{RV}\right] = \varsigma_{CO}\cdot g_{xle}$$

Estimate the mutation procedure

$$\xi^{new}\left[\grave{\lambda}^{RV}\right] \xrightarrow[\varsigma_{Mov}]{} \vartheta_{EF}$$

End For

End While

Return: $\vartheta_{EF}^{h} = \vartheta_{EF}^{1}, \vartheta_{EF}^{2}, \vartheta_{EF}^{3}, \cdots, \vartheta_{EF}^{H}$

End

Figure 4.2: Pseudo-code for the proposed GA technique

Then, for the effective and efficient classification of various stages of AD, the proposed framework evaluates the RS prediction.

4.2.3 RISK SCORE PREDICTION PHASE

In this phase, for the prediction of RS, the ADAS-Cog 13 set of pertinent variables is chosen from the given data set. Here, to quantitatively measure the status of the subject disease, the ADAS-Cog-13 scale results are collected. Based on these values, the RS prediction is computed for the accurate and effective classification of AD stages. In this phase, ADAS-Cog-13 selection and RS prediction are included, which are elaborated further.

4.2.3.1 ADAS-Cog-13 Selection

Here, for the efficient risk prediction process, the most relevant variables are selected from the ADAS-Cog-13. This selection process is carried out by using the TT-SWM technique, where the SWM is applied to incorporate 13 features with predetermined weight values. In the conventional SWM, the features are analyzed and their respective global and local weight values are built, which are then used for weighted mean determination. However, it experiences a loss of significant features or information due to the changeability of the information that is available in the dataset. Therefore, to tackle the limitation of the conventional SWM, the TT techniques are applied to weight assignment for offering improved risk prediction. Hence, the proposed technique is known as TT-SWM. Then, the steps involved in the process of ADAS-Cog-13 selection are given below,

❖ Primarily, through the z-score, the features in the ADAS-Cog-13 are investigated with the weight values. The particular feature is chosen if both the features present in the dataset and the weight values are true. Further, the necessary weights are allocated. This can be illustrated by using the following mathematical equation,

$$\omega^{WAF_I} = \begin{cases} if\left(\omega_{WV}, F_I == True\right) & ; F_I = \omega^{WAF_I} \\ else & ; 0 \end{cases} \tag{4.23}$$

Here, the weight-assigned features are denoted as ω^{WAF_I}, the weight values are exemplified as ω_{WV}, and the maximum number of features from the given dataset is indicated as F_I.

❖ Furthermore, the z-score is formulated by utilizing the following mathematical equation.

$$\wp^{Z-S} = \sigma^{SD} \cdot \left(F_I\right)^{-\frac{1}{2}} \left\{ \mu_{mean} - \gamma\left(F_I^K,\, F_I^k\right) \right\} \tag{4.24}$$

Where, the z-score is represented as $\wp^{Z-S}$, the standard deviation is denoted as σ^{SD}, the weighted mean value is shown as μ_{mean}, the correlation between K_{th} and k_{th} feature is expressed as $\gamma\left(F_I^K,\, F_I^k\right)$. By using $\wp^{Z-S}$, the features in the ADAS-Cog-13 dataset are investigated with their weight values.

❖ The relation between the features is determined based on the z-score equation for the accurate selection of ADAS-Cog 13. It is illustrated by the following mathematical equation,

$$\gamma = \varpi^{cv}\left|K, k\right| \times \left\{ \upsilon^{mm}\left[K\right] \cdot \upsilon^{mm}\left[k\right] \right\}^{-1} \tag{4.25}$$

Here, the covariance between K_{th} and k_{th} feature is denoted as $\varpi^{cv}\left|K, k\right|$, and the moment of K_{th} and k_{th} feature is notated as $\upsilon^{mm}\left[K\right]$ and $\upsilon^{mm}\left[k\right]$, respectively.

❖ In addition, the weight mean value is computed according to the z-score equation by multiplying features with their corresponding weight values. Then, the multiplied feature with weight values is determined by using the following mathematical equation,

$$\omega_{WV} F_I = \omega_{WV} \left\langle F_I^1, F_I^2,\, F_I^3, \cdots,\, F_I^m \right\rangle \tag{4.26}$$

Where, m illustrates the maximum number of the features from the given dataset. The summation is carried out on both sides once the features are multiplied with

their respective weight values. This can be illustrated by using the following mathematical expression,

$$\sum_{m^m=1}^{m}\left|\omega_{WV}\right|^k\left|F_I\right|^k=\sum_{1}^{m}\left|\omega_{WV}\right|^k\cdot\left\{F_I^1,F_I^2,F_I^3,\cdots,F_I^m\right\} \tag{4.27}$$

- From the above equation 4.27, the weighted mean value is assessed by the ratio of the summation of multiplied features with weight values to the individual weight values. This is formulated by the following mathematical depiction,

$$\mu_{mean}\left(\left|\omega_{WV}\right|^k,k\right)=\left\{\sum_{1}^{m}\left|\omega_{WV}\right|^k\cdot\left|F_1\right|^k\times\left\langle\sum_{1}^{m}\left|\omega_{WV}\right|^k\right\rangle^{-1}\right\}^{1/k} \tag{4.28}$$

- Finally, the number of features selected is determined based on the weighted mean values and is elaborated as,

$$\mu_{mean}\left(\left|\omega_{WV}\right|^k,k\right)\Rightarrow\eta_{AS} \tag{4.29}$$

Where, the selected features are illustrated as η_{AS} and are regarded as the selected ADAS-Cog 13 from the given dataset. Further, the comprehensive explanation of the selected ADAS-Cog 13 is given below,

$$\eta_{AS}^n=\eta_{AS}^1,\eta_{AS}^2,\eta_{AS}^3,\cdots,\eta_{AS}^N \tag{4.30}$$

Here, $n=1,2,3,\cdots,N$, the maximum number of features selected for the accurate RS prediction of AD is exemplified as N. After that, the selected features are given to the next phase of accurate and effective classification of AD stages known as the RS prediction. Figure 4.3 depicts the pseudo-code for the proposed TT-SWM technique.

Input: Features in the ADAS-Cog-13 F_I

Output: Selected features η_{AS}

Begin

Initialize $\omega_{WV}, \omega^{WAF_I}, \wp^{Z-S}, \mu_{mean}, \varpi^{CV}|K,k|$, iteration (itr), and maximum iteration $(itr_{\max})$

Set $(itr = 1)$

While $(itr_{\max} \le itr)$

For each F_I **do**

If $(\omega_{WV}, F_I == True)$

{

$F_I = \omega^{WAF_I}$

}

Else

{

$\omega^{WAF_I} = 0$

}

End If

Estimate correlation

$$\gamma = \varpi^{CV}|K,k| \times \left\{\upsilon^{min}[K] \cdot \upsilon^{min}[k]\right\}^{-1}$$

Evaluate the weighted mean values

$$\mu_{mean}\left(|\omega_{WV}|^k, k\right) = \left\{\sum_{1}^{m}|\omega_{WV}|^k \cdot |F_1|^k \times \left\langle \sum_{1}^{m}|\omega_{WV}|^k \right\rangle^{-1}\right\}^{1/k}$$

Calculate z-score

$$\wp^{Z-S} = \sigma^{SD} \cdot (F_I)^{-\frac{1}{2}}\left\{\mu_{mean} - \gamma\left(F_I^K, F_I^k\right)\right\}$$

Select thefeatures

$$\mu_{mean}\left(|\omega_{WV}|^k, k\right) \Rightarrow \eta_{AS}$$

End For

End While

Return: $\eta_{AS}^n = \eta_{AS}^1, \eta_{AS}^2, \eta_{AS}^3, \cdots, \eta_{AS}^N$

End

Figure 4.3: Pseudo-code for the proposed TT-SWM approach

Now, the selected features are fed as input to classify AD stages through the prediction of RSs.

4.2.3.2 Risk Score Prediction

The RS is examined in this step for assessing the stages of AD, which is carried out after the assignment of weight to the features. Based on the different time points, the

weights are assigned. This process is repeatedly carried out until the maximum iterations are reached. The ventricle volume weights have to be assigned for the RS prediction. These ventricle volume weights are assigned likewise the weight assignments based on the different time points. Then, the assigned ventricle volume weights are indicated by the following mathematical depiction,

$$\mathrm{Y}_{VWV} = \omega_{WV} F_I \tag{4.31}$$

Where, the assigned ventricle volume weight is exemplified as Y_{VWV} .

The RS is computed based on the ventricle volume's weight for the accurate and effective prediction of AD stages. Here, if the ventricle volume weight is high when compared to the other weight, then the patient is considered to be at risk; otherwise, the patient is considered to be at low risk. This is comprehensively explained by the following mathematical equation,

$$\Re^{PR} = \begin{cases} RISK & ;if\left(\mathrm{Y}_{VWV} > \omega^{other}\right) \\ No-RISK & ;else \end{cases} \tag{4.32}$$

Where, the predicted score is indicated as $\Re^{PR}$, and the other weight values are notated as ω^{other} . The AD's severity level is assessed from the predicted score. Even after the prediction of RS, the severity of AD can't be predicted for lower-risk patients. Thus, to accurately classify AD stages, the output from the RS prediction is provided as input to the classifier.

4.2.4 Brain Shrinkage Measurement Phase

Measurement of brain shrinkage is carried out in this phase by analyzing the given dataset for the accurate and efficient classification of AD stages. Brain shrinkage is also referred to as BA or cerebral atrophy. It is a gradual reduction in brain size and volume after reaching maturity. Furthermore, BA is a loss of neurons and correlations betwixt neurons. BA is caused by various conditions, such as dementia, cerebral palsy, and infectious diseases. Therefore, since diagnosing the stage of AD patients and serving them with corresponding therapy are significant, the brain

shrinkage measurement is computed to investigate the relationship betwixt hippocampus MRI radiomen features and intra-hippocampal functional connectivity in AD. So, the QBCS technique is applied to determine the volume of the hippocampus area, the whole brain, and the brain shrinkage factor affected by AD. The whole brain volume is another measure utilized for correcting the head size variation across subjects. The hippocampus area is affected by AD, stress, depression, and epilepsy, and the brain shrinkage factors are stroke and traumatic brain injury.

4.2.4.1 Parameter Measurement

Here, by utilizing the QBCS technique, the parameters responsible for the measurement of brain shrinkage are evaluated. In QBCS methodology, a 2-dimensional stretching sheet is taken into account for the measurement of hippocampus volume and brain shrinkage. By using this theorem, minimal and maximal values are taken. Further, a detailed explanation of the QBCS technique is given as,

- ✓ Initially, the constant magnetic field of strength is applied to measure the hippocampus volume measurement. When it is applied on the constant surface or the human brain, the temperature and heat transfer coefficient are changed. This is described by utilizing the following mathematical equation.

$$x\frac{\partial x}{\partial X}+y\frac{\partial x}{\partial Y}=-\frac{1}{den}\left|\frac{\partial f^{pre}}{\partial X}-\lambda^{wl}\left[\frac{\partial^2 x}{\partial X^2}-\frac{\partial^2 x}{\partial Y^2}\right]+\upsilon^{qbc}\cdot S^2\cdot x\right| \quad (4.33)$$

Where, the velocity components in X and Y directions at the time t are indicated as x and y, respectively, the density is illustrated as den, the strength is displayed as S, the fluid pressure is investigated as f^{pre}, the queue absorption coefficient is specified as υ^{qbc}, and the wavelength is signified as λ^{wl}.

- ✓ Subsequently, for measuring the flux measurement, the Rosseland diffusion approximation is applied. A method for approximating the heat transfer by

radiating in a participating medium is termed the Rosseland approximation. It is a variation of ration diffusion approximations, which is primarily applicable for optically thick media. The approximation considers that the photons' mean free path is much smaller when compared to the material thickness, allowing the transportation of radiative heat to be approximated as a diffusion process. The radiative heat flux term is introduced in the energy equation by the Rosseland approximation. Further, the Rosseland diffusion approximation is formulated by using the following mathematical expression,

$$\mathrm{E}_{RDE} = -4\upsilon^{qbc} \cdot \left(3\mathrm{B}_{con}\right)^{-1} \cdot \frac{\partial t^4}{\partial Y} \tag{4.34}$$

Here, the Rosseland diffusion approximation is notated as E_{RDE}, and the Boltzmann constant is indicated as B_{con}.

- ✓ In addition, the local skin friction coefficient, nusselt, and Sherwood number are reduced and are expressed in the following mathematical equations.

$$\beta^{FC} = \sqrt{\aleph_{RN}}\beta^{FC} \tag{4.35}$$

$$\beta^{NUS} = \frac{1}{\sqrt{\aleph_{RN}}}\beta^{NUS} \tag{4.36}$$

$$\beta^{SHE} = \frac{1}{\sqrt{\aleph_{RN}}}\beta^{SHE} \tag{4.37}$$

Where, the local skin friction coefficient is notated as β^{FC}, the Nusselt is signified as β^{NUS}, the Sherwood number is specified as β^{SHE}, and the Reynolds number is exemplified as $\aleph_{RN}$.

- ✓ The Reynolds number can be expanded centered on the ratio of the shear factor to the strength, which can be expressed by utilizing the following mathematical expression,

$$\aleph_{RN} = \Re_{SF} \cdot S^{-1} \tag{4.38}$$

Here, the shear factor is exemplified as $\Re_{SF}$.

- ✓ Based on the Reynolds number, the brain shrinkage factor is evaluated regarding the estimation of internal and external shrinkages. This can be illustrated by the following mathematical expression,

$$\Re^{BSF} = \frac{100}{T}\left(\tau_{\text{int}} + \tau_{ext}\right) \tag{4.39}$$

Where, the calculated brain shrinkage is explained as $\Re^{BSF}$, the total hours of internal and external shrinkages are indicated as τ_{int} and τ_{ext}, respectively, and the available hours are illustrated as T. After that, for the accurate and efficient classification of AD stages, the measured parameters are applied for the measurement of rs-fMRI.

4.2.4.2rs-MRI measurement

Once the parameters are measured, certain radiomic features, such as functional connectivity values of the bilateral hippocampus, rs-fMRI, and the entire brain functional connectivity are extracted to effectively classify AD stages. Here, those features are measured by utilizing the PM technique. The PM technique is primarily used to determine the evolutionary relations betwixt the organisms via their tree structure. Further, the steps involved in the process of measuring the resting state fMRI are illustrated below,

- ❋ Primarily, for the measurement of rs-fMRI, the pairwise distance between the neurons present in the brain is evaluated, which is elaborated by using the following mathematical equation,

$$\chi^{PWD}\left(\propto_k, \propto_K\right) = \propto_k - \propto_K \tag{4.40}$$

Here, the pairwise distance between the neurons is signified as χ^{PWD}, and the neurons present in the brain are displayed as $\propto$.

❋ Subsequently, to effectively classify AD stages, the distance matrix has been constructed. By using the pairwise distance, the distance matrix is constructed and is elaborated by the following mathematical equation,

$$\mathrm{M}_{dist} = \begin{vmatrix} \chi_{11}^{PWD} & \cdots & \chi_{1K}^{PWD} & \cdots & \chi_{1J}^{PWD} \\ \vdots & \ddots & \vdots & \iddots & \vdots \\ \chi_{k1}^{PWD} & \cdots & \chi_{kK}^{PWD} & \cdots & \chi_{kJ}^{PWD} \\ \vdots & \iddots & \vdots & \ddots & \vdots \\ \chi_{I1}^{PWD} & \cdots & \chi_{IK}^{PWD} & \cdots & \chi_{IJ}^{PWD} \end{vmatrix}^{I\times J} \tag{4.41}$$

$$k = 1,\ 2,\ 3,\ 4,\ \cdots,\ I;\ K = 1,\ 2,\ 3,\ 4,\ \cdots,\ J \tag{4.42}$$

Here, the distance matrix is given as M_{dist}.

❋ Lastly, the tree is constructed based on the distance matrix to evaluate radiomic features. Therefore, for effectively classifying AD stages, the radiomic feature measurements are evaluated. This can be illustrated by the following mathematical equation,

$$\mathrm{M}_{dist} \xrightarrow[tree]{} \varepsilon_{RFM} \tag{4.43}$$

Where, the radiomic feature measurement is exemplified as ε_{RFM}, and the constructed tree is described as *tree*. Then, the comprehensive explanation of assessed radiomic feature measurement to accurately and efficiently classify AD stages is demonstrated by the following mathematical expression,

$$\varepsilon_{RFM}^{p} = \varepsilon_{RFM}^{1},\ \varepsilon_{RFM}^{2},\ \varepsilon_{RFM}^{3},\ \varepsilon_{RFM}^{4},\ \cdots,\ \varepsilon_{RFM}^{p_p} \tag{4.44}$$

Here, $p = 1,\ 2,\ 3,\ \cdots,\ p_p$, the maximum number of evaluated radiomic feature measurements is exemplified as p_p.

The bilateral hippocampus features are obtained from these radiomic feature measurements. For the accurate and effective classification of AD stages, these features are responsible. Also, through the construction of GLCM, these bilateral hippocampus features are obtained. A statistical method that analyzes the spatial

relationships between the radiomic feature measurements to produce the features responsible for the efficient diagnosis of AD stages is known as GLCM. Thereafter, based on the evaluated radiomic feature measurement, these features are obtained by using the GLCM, which is elaborately explained in the following mathematical equation,

$$GLCM\left[\varepsilon_{RFM}\right]=\Im_{obf} \tag{4.45}$$

Where, the construction of GLCM to obtain features is indicated as $\Im_{obf}$. Further, the detailed estimation of obtained features for the accurate and significant prediction and classification of various stages of AD is illustrated by using the following expression,

$$\Im_{obj}^{q}=\Im_{obj}^{1},\ \Im_{obj}^{2},\ \Im_{obj}^{3},\cdots,\ \Im_{obj}^{Q} \tag{4.46}$$

Here, $q=1,\ 2,\ 3,\cdots,\ Q$, the maximum number of bilateral hippocampus features obtained through the construction of GLCM is demonstrated as Q. Then, these features are inputted to the next stage known as FE, which is significant for the effective classification of various stages of AD.

4.2.4.3 Feature Extraction

The features responsible for classifying the AD stages effectively are extracted from the obtained bilateral hippocampus features $\Im_{obf}$ by using the GA technique. Section 4.2.6 already explains the steps involved in the process of extracting the features by using the GA technique. The features from the obtained bilateral hippocampus features are extracted centered on those steps. Then, the extracted features are expressed in the following mathematical equation,

$$\partial_{r}^{BFE}=\partial_{1}^{BFE},\ \partial_{2}^{BFE},\ \partial_{3}^{BFE},\cdots,\partial_{R}^{BFE} \tag{4.47}$$

Where, $r=1,\ 2,\ 3,\cdots,R$, the extracted features are demonstrated as ∂^{BFE}, and the maximum number of extracted features is represented as R. Then, for the accurate and effective classification of AD stages, ∂^{BFE} are provided to the final stage of the proposed framework.

4.2.5 Classification

The features from the ranking phase ϑ_{EF} , the brain shrinkage measurement phase ∂^{BFE}, and the predicted RS of AD $\Re^{PR}$ are provided as input in this phase for the effective classification of various stages of AD. For this purpose, the Deep-AD$_3$-Net classifier is used in the proposed framework, which is based on the common NN called CNN. The ReLU layer element-wise AF is applied in every layer of the traditional CNN. In addition, the pooling layer has been included for performing the down-sampling operation, which assists in enabling the possibility of decreasing the feature map's spatial resolution. Furthermore, based on the sampling frequency, the number of pixels in the provided image is reduced. In addition, for the computation of class scores and the generation of output, the Fully Connected Layer (FCL) is employed. Nevertheless, the conventional CNN had over-fitting issues owing to the presence of unwanted noise in the input values, affecting the classification of various AD stages. Moreover, the weight and bias values were generated randomly by the neurons present in the traditional CNN, causing more training time and a decrease in classification accuracy. Thus, to overcome these limitations, in the proposed framework, the three-layer technique is integrated with the traditional CNN and the deep layer at the end, preventing the proposed framework from overfitting issues. So, the proposed technique is called Deep-AD$_3$-Net. Figure 4.4 shows the classifier diagram for the proposed Deep-AD$_3$-Net technique.

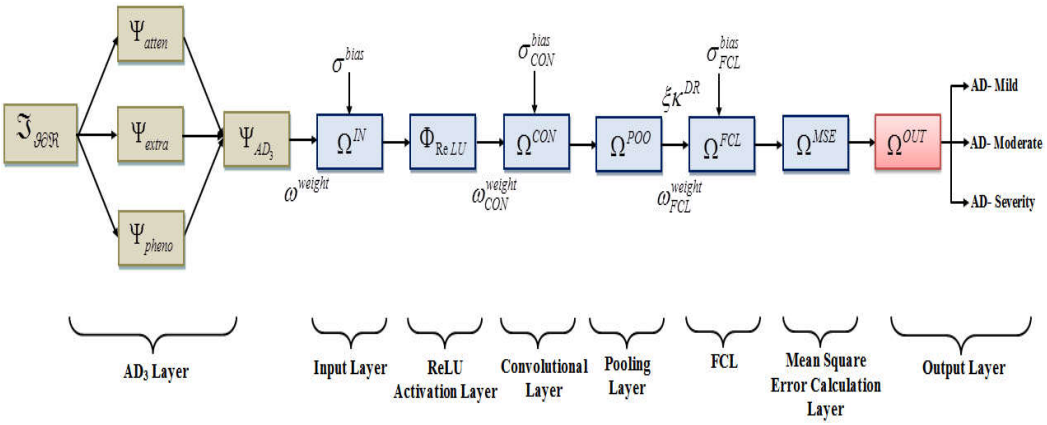

Figure 4.4: Classifier diagram for the proposed Deep-AD$_3$-Net

Primarily, the features from the ranking phase, RS prediction phase, and brain shrinkage measurement phase are gathered and integrated. Then, the combined features are elaborately expressed in the following mathematical equation,

$$\left.\begin{matrix} \vartheta_{EF} \\ \partial^{BFE} \\ \Re^{PR} \end{matrix}\right\} \rightarrow \Im_{\vartheta\partial\Re} \tag{4.48}$$

Here, the features, which are the combination of features from the ranking phase, RS prediction phase, and the brain shrinkage measurement phase, are notated as $\Im_{\vartheta\partial\Re}$. Then, these features are provided as input to the first layer termed the AD_3 layer.

❁ AD_3 Layer

In this AD_3 layer, the mean, accuracy, and computation time for each incoming feature $\Im_{\vartheta\partial\Re}$ are acquired in the attention layer. Further, the attention layer's output is indicated by the following expression,

$$\Psi_{atten} = \left[\mu\left|\Im_{\vartheta\partial\Re}\right|,\ \theta^{acc}\left|\Im_{\vartheta\partial\Re}\right|,\ \varphi_{Ct}\left|\Im_{\vartheta\partial\Re}\right|\right] \tag{4.49}$$

Where, the attention layer is indicated as Ψ_{atten}, the mean value of the feature is rendered as $\mu\left|\Im_{\vartheta\partial\Re}\right|$, the accuracy is demonstrated as θ^{acc}, and the computation time of each feature is implied as φ_{Ct}.

Then, in the extraction layer, the area-correlated features are assessed. The evaluated area-correlated features for the accurate classification of various stages of AD are demonstrated by using the following mathematical equation,

$$\Psi_{extra} = \delta^{ARF} \tag{4.50}$$

Here, the extraction layer is shown as Ψ_{extra}, and the extracted area-related features are given as δ^{ARF}.

The phenotype-assistant layer is the final layer of the AD_3 layer, which comprises the volume of data with its microstructure-oriented results, and is demonstrated by using the following mathematical depiction,

$$\Psi_{Pheno} = \left\langle \infty^{VD} \right\rangle \tag{4.51}$$

Where, the phenotype-assistant layer is notated as Ψ_{Pheno}, and the volume of data with microstructure-oriented results is illustrated as ∞^{VD}. Now, the output from every single layer is fed as input to the input layer.

❁ **Input Layer**

The output of the attention layer, extraction layer, and phenotype-assistance layer from the AD_3 layer is multiplied by the weights and biases of neurons present in the input layer. Further, the input layer effect is indicated by utilizing the following mathematical depiction,

$$\Omega^{IN} = \omega^{weight} \cdot \Psi_{AD_3} + \sigma^{bias} \tag{4.52}$$

Here, the input layer is indicated as Ω^{IN}, the weights are depicted as ω^{weight}, and the biases of the neurons in the input layer are demonstrated as σ^{bias}, and the output of the AD_3 layer, which includes the results of attention, extraction, and the phenotype-assistance layers, is signified as Ψ_{AD_3}. This can be elaborated as follows,

$$\Psi_{AD_3} = \left| \Psi_{atten}, \Psi_{extra}, \Psi_{pheno} \right| \tag{4.53}$$

The input layer's output is given to the ReLU activation layer after multiplying the weights and biases.

❁ **ReLU activation layer**

Once the input layer is performed, the ReLU AF is applied. Here, ReLU AF is referred to as the piecewise linear function triggering the neurons for producing the

output. Then, the ReLU activation layer's output is demonstrated by using the following mathematical equation,

$$\Omega^{\mathrm{Re}LU} = \Phi_{\mathrm{Re}LU}\left[\Omega^{IN}\right] \tag{4.54}$$

Where, the ReLU AF layer's output is depicted as $\Omega^{\mathrm{Re}LU}$, and the ReLU AF is demonstrated as $\Phi_{\mathrm{Re}LU}$. Then, the ReLU AF's detailed explanation is illustrated by using the following mathematical expression,

$$\Phi_{\mathrm{Re}LU}\left[\Omega^{IN}\right] = \max\left(0,\ \Omega^{IN}\right) \tag{4,55}$$

Now, the output from the ReLU activation layer is collected and provided as input to the next layer termed the Convolutional Layer (CL).

❁ Convolutional Layer

The proposed Deep-AD_3-Net technique's CL performs convolution operation. This layer performs convolution operations by utilizing the weights and bias values of the CL with filters, which can be explained by the following mathematical depiction,

$$\Omega^{CON} = \Phi_{\mathrm{Re}LU}\left(\Omega^{IN} \oplus \omega_{CON}^{weight} \cdot \mathrm{X}_{fil}\right) + \Phi_{\mathrm{Re}LU}\left(\sigma_{CON}^{bias}\right) \tag{4.56}$$

Here, the output of the CL is represented as Ω^{CON}, the weight values of the CL are exemplified as ω_{CON}^{weight}, the bias values of the CL are shown as σ_{CON}^{bias}, and the filters are displayed as X_{fil}.

❁ Pooling Layer

The pooling layer is performed from the output of the CL to decrease the computational complexity by applying the down-sampling, diminishing the computational power required for processing the data. Also, the input data's dimension is reduced by integrating the outputs of the neurons at one layer with a single neuron in the next layer. Subsequently, the dimensionality-reduced data is depicted by using the following mathematical depiction,

$$\Omega^{POO} = \xi\kappa^{DR} \tag{4.57}$$

Where, the pooling layer's output is exemplified as Ω^{POO}, and the dimensionality-reduced data is indicated as $\xi\kappa^{DR}$. Then, for the accurate classification of AD stages, these dimensionality-reduced data are given to the FCL.

❁ **Fully Connected Layer**

The dimensionality-reduced data is given as input for this layer to generate classification results. The classification results are generated in this layer based on the incorporation of the weights and biases of the FCL of each neuron. This can be explained by using the following mathematical equation,

$$\Omega^{FCL} = \Phi_{\mathrm{Re}LU}\left(\xi\kappa^{DR} \cdot \omega_{FCL}^{weight}\right) + \Phi_{\mathrm{Re}LU}\left(\sigma_{FCL}^{bias}\right) \tag{4.58}$$

Here, the output of the FCL is depicted as Ω^{FCL}, and the weight as well as bias values of the FCL are signified as ω_{FCL}^{weight} and σ_{FCL}^{bias}, respectively.

❁ **Mean Square Error Calculation Layer**

The results from the FCL are analyzed in this layer for the computation of error values. Based on the predicted outcomes and the actual results of the FCL, the calculation of error values is carried out. This can be illustrated by using the following mathematical equation,

$$\Omega^{MSE} = \frac{1}{2}\sum\left\langle \Xi^{AO} - \Omega^{FCL} \right\rangle^2 \tag{4.59}$$

Where, the mean square error and actual output are shown as Ω^{MSE} and Ξ^{AO}, respectively.

❁ **Output Layer**

Once the mean square error is computed, the output layer of the proposed technique gives the detected and classified AD stages, namely mild, moderate, and severe. This can be explained by using the following mathematical depiction,

$$\Omega^{OUT} = \begin{cases} AD-mild \\ AD-\text{mod}erate \\ AD-severity \end{cases} \quad (4.60)$$

Here, the output layer is indicated as Ω^{OUT}. Thus, the various stages of AD are effectively detected and classified by the proposed Deep-AD_3-Net technique. The pseudo-code for the proposed Deep-AD_3-Net technique is exemplified in Figure 4.5,

Input: Features from $\vartheta_{LF}, \partial^{RFE}, \Re^{PR}$
Output: Classified output Ω^{OUT}
Begin
Initialize $\Psi_{atten}, \Psi_{extra}, \Psi_{pheno}, \mathrm{X}_{fil}, \Phi_{ReLU}$, iteration (itr), and maximum iteration (itr_{max})
Set $(itr = 1)$
While $(itr_{max} \le itr)$
For each $\Im_{\mathcal{RR}}$ do
Perform AD_3 layer
$\Psi_{AD_3} = \left|\Psi_{atten}, \Psi_{extra}, \Psi_{pheno}\right|$
Multiply the weights and bias of the input layer
$\Omega^{IN} = \omega^{weight} \cdot \Psi_{AD_3} + \sigma^{bias}$
ApplyReLU activation function
$\Phi_{ReLU}\left[\Omega^{IN}\right] = \max\left(0, \Omega^{IN}\right)$
Achieve convolution operation
$\Omega^{CON} = \Phi_{ReLU}\left(\Omega^{IN} \oplus \omega^{weight}_{CON} \cdot \mathrm{X}_{fil}\right) + \Phi_{ReLU}\left(\sigma^{bias}_{CO}\right.$
Calculate the dimensionality reduced data
If $\left(\Omega^{POO} = \xi\kappa^{DR}\right)$
{
$\xi\kappa^{DR} \rightarrow \Omega^{FCL}$
}
Else
{
$\Omega^{FCL} = 0$
}
End If
Evaluate the mean square error
$\Omega^{MSE} = \frac{1}{2}\sum\left\langle \Xi^{AO} - \Omega^{FCL} \right\rangle^2$
EndFor
EndWhile
Return: $\Omega^{OUT} = \begin{cases} AD-mild \\ AD-\text{mod}erate \\ AD-severity \end{cases}$
End

Figure 4.5: Pseudo-code for the proposed TT-SWM approach

Thus, the proposed framework aids in accurately classifying the AD stages by effectively predicting the RS.

4.3 Summary of the Proposed Framework

This framework implemented a dominant AD stage and risk prediction framework using the TADPOLE dataset based on the TT Self-Weighted Deep-AD_3-Net. Three phases, namely ranking, RS prediction, and brain shrinkage measurement are mainly included in this framework. Here, this approach begins with a ranking phase in which variables like gender, age, ICV, brain volume, hippocampus, mild temp, mid-left, and mid-right are successfully extracted from the given ADNI tadpole dataset. After that, by using the RHCA technique, the variables responsible for accurately classifying AD stages are selected via the removal of unwanted noise. Later, by applying the tailored metric, the chosen variables, namely the neuropathological hallmarks, such as APs and CAA, NFTs, glial responses, ICV, MAE, WES, and CPA are ranked. In the tailored metric ranging algorithm, the Markov chain technique generates samples of continuous random variables with probability density proportional to a known function for ranking the variables. By employing the GA technique, the features are successfully extracted from the ranked variables. By adopting the multi-point parallel approach and population-based optimization method, this technique extracts the features. Likewise, an RS prediction phase is performed in the proposed framework. In this phase, the ADAS-Cog-13 features are successfully selected by the proposed TT-SWM technique by applying the TT technique. This technique effectively assigns the weight to offer ameliorated risk predictions. Centered on the ventricle volume weights, the RS has been successfully predicted centered on these features. Lastly, the QBCS approach is employed for measuring the parameters in the brain shrinkage measurement phase in which the volume and hippocampus area of the brain and the rate of shrinkage are evaluated. After that, the rs-fMRI for the whole brain with the bilateral hippocampus is effectively measured by the PM technique. Later, the GLCM, which helps to obtain the features for the classification of AD, is successfully created by the proposed framework. By using the GA, the obtained features are extracted. Lastly, by

considering the features from the ranking phase, RS prediction phase, and brain shrinkage measurement phase, the classifier Deep-AD_3-Net successfully classifies the various stages of AD, namely AD-mild, AD-moderate, and AD-severity. Therefore, in terms of accurate RS prediction and classification of AD stages, the proposed framework outperformed the other prevailing approaches based on the utilization of the TADPOLE dataset. In addition, the proposed framework outperformed the other conventional techniques by proposing appropriate techniques for RS prediction and the classification of AD stages.

Experimental Analysis

Cross-Dataset Validation: Although the experiments used the TADPOLE dataset, future validation using other public datasets such as OASIS and AIBL is planned to evaluate the model's generalizability across populations.

Comparison with Transformer-Based Models: Recent transformer and Vision Transformer (ViT) models have shown strong performance in medical imaging. The proposed GS-RBFN and Deep-AD3Net methods complement these approaches by offering faster convergence and higher interpretability, while maintaining competitive accuracy.

CHAPTER 5
RESULT AND DISCUSSIONS

5.1 INTRODUCTION

AD is a progressive brain disorder and is the most general type of dementia affecting memory, thought, and language. AD has resulted from complex changes in the brain, which started years prior to symptoms appearing, causing brain cell loss and disconnections. Thus, early prediction and diagnosis of AD are significant. For the prediction and classification of AD, various approaches are implemented. Yet, inaccurate results of AD classification are produced by most of the approaches. Therefore, two frameworks are implemented in this proposed work to accurately predict and classify AD. The proposed framework introduced the early prediction and classification architecture based on considering the ADNI brain images utilizing the GS-RBFNs classifier in the first implementation. Furthermore, in the second implementation, the most popular TADPOLE dataset is employed for the risk prediction and classification of AD utilizing the TT-self-weighted Deep-AD_3-Net. Also, this chapter assesses the proposed two implementations' performance. In this chapter, the results of the proposed works are discussed based on comparing the performance of the conventional works. Also, the supremacy and effectiveness of the proposed frameworks are provided in this chapter.

5.2 Hardware Requirements

In this section, the machine configurations of the proposed 1^{st}, and $2^{nd,}$ implementations are explained.

- **Processor** : Intel i5/core i7
- **CPU Speed** : 3.20 GHz
- **OS** : Windows
- **RAM** : 4GB

5.3 Software Requirement

The 1st and 2nd, implementations of the proposed framework are simulated on the working platform of PYTHON, which is a broadly wielded general-purpose, high-level programming language. It is chiefly established for highlighting code readability. The syntax of Python permits programmers to express concepts in fewer lines of code. It is a programming language, which lets programmers work rapidly and incorporate schemes more effectually. An isolated Python environment (in the form of a directory), which is completely separate from the system-wide Python environment, is created by the virtual environment tool.

5.4 Dataset Description

This section elaborately explains the description of the datasets that are used for the 1st and 2nd implementations of the proposed model.

5.4.1 Dataset description for the 1st implementation

To effectively predict and classify AD, the first implementation of the proposed framework utilized the ADNI dataset. ADNI represents a clinical dataset, comprising in-depth subject details, comprising demographics, physical examinations, and cognitive evaluations. The ADNI's primary objective revolves around validating AD biomarkers for clinical trials. Regarding this, 80% and 20% of the data are reserved for training and testing purposes, correspondingly. Moreover, Table 5.1 illustrates the image outcomes for the proposed 1st implementation.

Table 5.1: Image results for the proposed 1st implementation framework

Input image	Intensity normalization	Skull stripping	Spatial smoothing	Brain segmentation
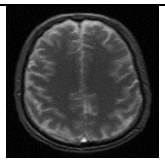	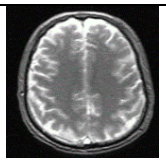	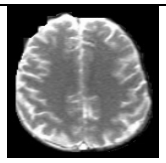	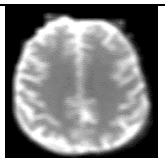	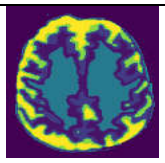
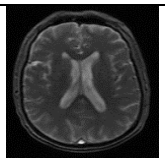	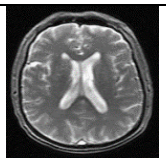	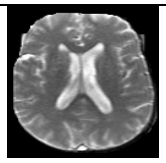	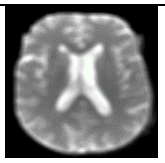	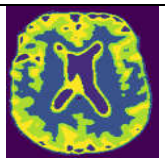
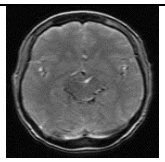	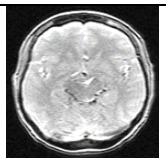	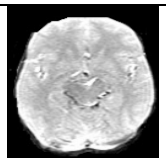	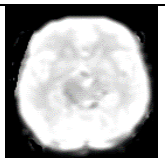	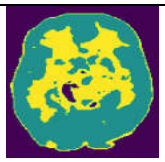
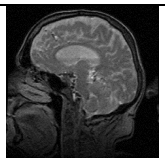	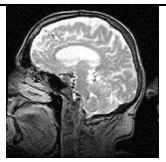	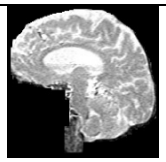	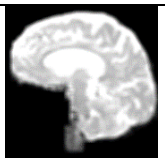	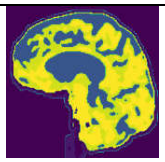

5.4.2 Dataset description for the 2nd implementation

The proposed framework's second implementation applied a publicly available dataset called the ADNI tadpole dataset. This dataset encompasses different variables, namely age, gender, education, ICV, whole brain, Hippocampus, Mid-temp, Mid-left, Mid-right, and so on. Moreover, TADPOLE offers three standard datasets, including D1, D2, and D3, which are derived from the ADNI study. D1, D2, and D3 illustrate the comprehensive longitudinal dataset for training, the comprehensive longitudinal dataset on rollover subjects to forecast, and the limited forecasting dataset on similar rollover subjects as D2, respectively.

5.5 Simulation Parameters

Table 5.2 and Table 5.3 depict the simulation parameters for the 1st and 2nd implementations of the proposed framework, respectively.

Table 5.2: Simulation parameters for the 1st implementation

Parameters	**Values**
Batch-size	32
Epochs	20
Optimizer	rmsprop
Activation	GELU and SWISH
Learning rate	0.01
Beta	1
Kernels	2

Table 5.3: Simulation parameters for the 2nd implementation

Parameters	**Values**
Learning rate	0.005
Activation	RELU
Momentum	0.5
Decay	0.0004
Batch-size	512
Optimizer	Adam
Beta	0.9
Epochs	20

5.6 Performance Metrics

For assessing the quality of the proposed methodology, performance metrics, comprising accuracy, precision, sensitivity, f-measure, specificity, True Positive Rate (TPR), False Negative Rate (FNR), and False Positive Rate (FPR) are considered. Further, each performance metric's comprehensive explanation is illustrated as follows,

Accuracy: It is the proportion of appropriately predicted values to the total number of values. Also, it is referred to as the degree to which the value being measured is

close to the actual measurements of the object. Then, the accuracy metric can be articulated further,

$$Accuracy = \frac{\sigma^{tn} + \sigma^{tp}}{\sigma^{tn} + \sigma^{tp} + \sigma^{fn} + \sigma^{fp}} \tag{5.1}$$

Precision: It gauges the ratio of accurately classified occurrences or samples among those classed as positive. The formula for precision is calculated by using the following mathematical expression,

$$\Pr ecision = \frac{1}{1 + \frac{\sigma^{fp}}{\sigma^{tp}}} \tag{5.2}$$

Recall: It is the ratio of the proportion of true positive prediction to the total number of actual positive instances. An evaluation metric for the calculation problem that quantifies the ability of the model for the identification of relevant instances is represented by the recall. The recall is computed as,

$$\mathrm{Re}\, call = \left[\frac{\sigma^{tp} + \sigma^{fn}}{\sigma^{tp}} \right]^{-1} \tag{5.3}$$

Specificity: It evaluates the ratio of actual negative cases, which are appropriately identified by the proposed framework, out of the total number of actual negative cases. The formula to represent the specificity is illustrated by the following equation,

$$Specificity = \left[\frac{\sigma^{tn} + \sigma^{fp}}{\sigma^{tn}} \right]^{-1} \tag{5.4}$$

Sensitivity: It is also referred to as TPR. It gauges the proportion of actual positive cases appropriately recognized by the mode. Furthermore, the avoidance of false negatives is quantified by the sensitivity. The formula for the representation of sensitivity values is expressed as,

$$Sensitivity = \sigma^{tp} \left[\frac{1}{\sigma^{tp} + \sigma^{fn}} \right] \tag{5.5}$$

F-measure: It is also called as the F1-score or F-score. It is a metric applied to assess the ML model's performance. It is the combination of precision and recall into a score. Then, the formula to find the F-score value is indicated in the following expression,

$$F-measure = 2 * \left|\Pr ecision \times \mathrm{Re} call\right| \cdot \left|\Pr ecision + \mathrm{Re} call\right|^{-1} \tag{5.6}$$

FNR: It is the proportion of measuring the actual positive samples inaccurately predicted as negative to the total number of actual positive cases. In addition, using the FNR, the capability and consistency of the model are also measured. The following equation indicates the formula of FNR.

$$FNR = \frac{\sum\left|\sigma^{fn}\right|}{\sum\left|\sigma^{tp} + \sigma^{fn}\right|} \tag{5.7}$$

TPR: It is the ratio of actual positive cases that are correctly identified or categorized as positive by the framework. Also, TPR is expressed as recall, sensitivity, or hit rate, where the positive instances are measured and detected accurately as positive by the model. The TPR is computed as,

$$TPR = \frac{\sum\left|\sigma^{tp}\right|}{\sum\left|\sigma^{tp} + \sigma^{fn}\right|} \tag{5.8}$$

FPR: It is the possibility of falsely rejecting the null hypothesis, which is also called a fall-out or false alarm ratio. The FPR is computed as the proportion betwixt the number of negative events, which are inaccurately characterized as positive, and the total number of actual negative events. The formula for FPR is illustrated as,

$$FPR = \frac{\sum\left|\sigma^{fp}\right|}{\sum\left|\sigma^{tn} + \sigma^{fp}\right|} \tag{5.9}$$

Here, the true negative and positive are indicated as σ^{tn} and σ^{tp}, correspondingly, and the false negative and positive are illustrated as σ^{fn} and σ^{fp}, respectively.

5.7 PERFORMANCE ANALYSIS FOR THE EFFECTIVE EARLY PREDICTION AND CLASSIFICATION OF AD

Here, the proposed 1st implementation work's performance analysis is implemented. Here, the proposed early prediction and classification of the AD framework's performance is validated centered on the results obtained by comparing it with the prevailing works and techniques. Based on the performance of the proposed GS-RBFN, BLSAOWS, and BSRISRHSO techniques, this performance analysis is performed. Additionally, the comparative investigation is made to examine the proposed framework's effectiveness based on validating it with conventional works.

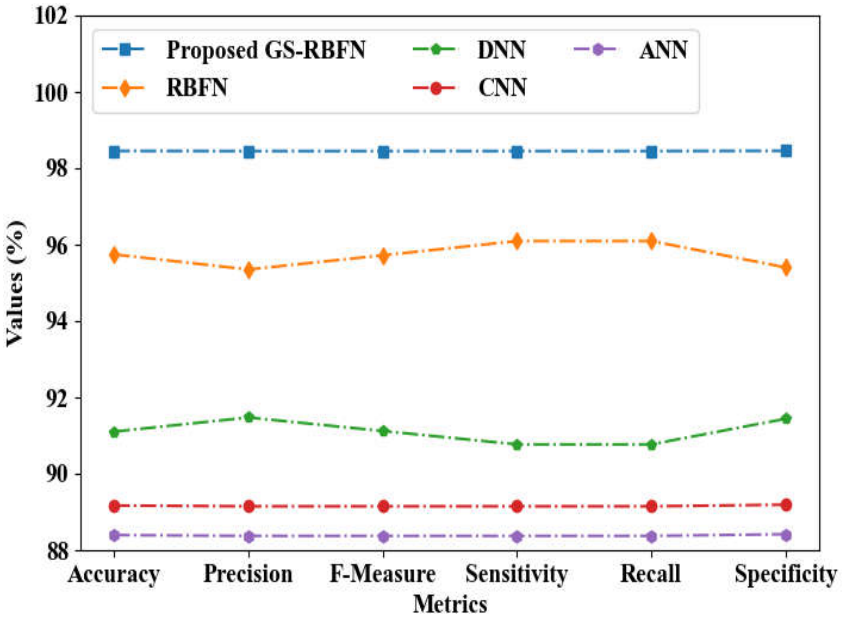

Figure 5.1: Performance validation of the proposed GS-RBFN technique

In Figure 5.1, the proposed GS-RBFN approach's performance validation is illustrated by analogizing it with various prevailing approaches like RBFN, DNN, CNN, as well as Artificial NN (ANN). The proposed GS-RBFN attained accuracy, precision, f-measure, sensitivity, recall, and specificity of 98.45%, 98.44%, 98.44%, 98.44%, 98.44%, and 98.45%, correspondingly. The conventional RBFN attained an accuracy of 95.74%, a precision of 95.34%, a sensitivity of 96.09%, an f-measure of 95.71%, a recall of 96.09%, and a specificity of 95.40%. Hence, as per these results, the proposed GS-RBFN attained better accuracy, recall, precision, f-measure, specificity, and sensitivity than the other conventional techniques. Also, when

contrasted with the other top-notch approaches, the proposed system's performance is increased due to the integration of GELU and SWISH AFs.

Table 5.4: Training time for the proposed GS-RBFN technique

Technique	**Training Time (ms)**
Proposed GS-RBFN	29539
RBFN	32841
DNN	37250
CNN	46216
ANN	59135

In Table 5.4, the proposed technique's training time is estimated. This table shows that the proposed GS-RBFN technique took 29539ms training time, which is much less than other conventional techniques. The lesser training time of the proposed GS-RBFN technique is due to the incorporation of GELU and SWISH AFs, thus increasing the capability of the proposed framework with respect to handling complex sequences. Hence, this indicates that the proposed framework had very little training time. Also, the conventional RBFN, DNN, CNN, and ANN took 32841ms, 37250ms, 46216ms, and 59135ms training time, respectively.

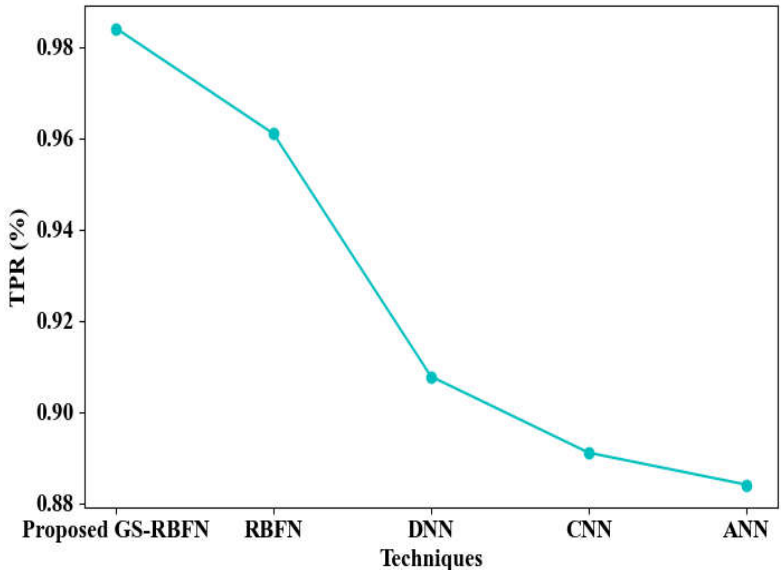

Figure 5.2: TPR evaluation of the proposed GS-RBFN

The GS-RBFN technique's performance concerning the calculated TPR value is indicated in Figure 5.2. This figure shows that the proposed GS-RBFN technique attained a TPR of 0.984, while the conventional RBFN, DNN, CNN, and ANN attained 0.96, 0.90, 0.81, and 0.88 TPR, respectively. Therefore, these results illustrate that the proposed GS-RBFN had higher TPR when compared to other conventional techniques. This high TPR increases the proposed framework's performance in the precise AD diagnosis. This is owing to the incorporation of the SWISH AF with the conventional RBFN technique.

Table 5.5: Evaluation of computation time for the proposed GS-RBFN technique

Algorithms	**Computation Time (ms)**
Proposed GS-RBFN	14876
RBFN	17454
DNN	21456
CNN	25353
ANN	27654

Table 5.5 illustrates the evaluation of computation time for the proposed GS-RBFN technique. As per this table, the proposed GS-RBFN technique required much less time compared to the other traditional approaches. Additionally, this tabulation expresses that the proposed GS-RBFN technique's computation time is 14876ms. The traditional RBFN, DNN, CNN, and ANN had 17454ms, 21456ms, 25353ms, and 27654ms computation time, respectively. Hence, as per this experimental result, the proposed framework's performance increased in AD classification with low time complexity due to the integration of GELU and SWISH AFs into the RBFN technique.

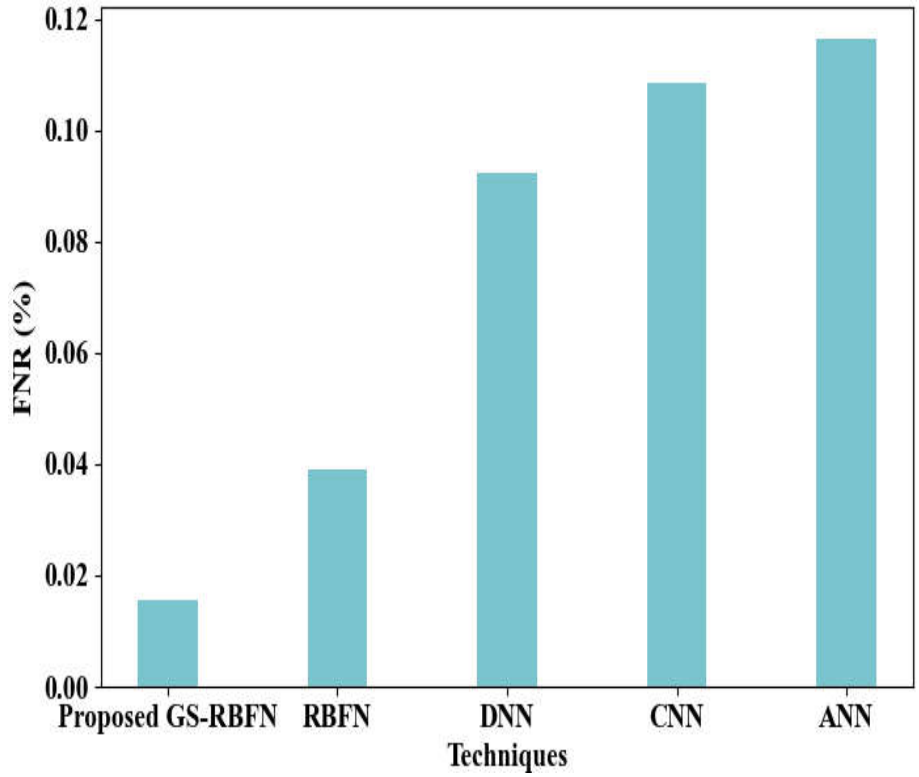

Figure 5.3: FNR validation for the proposed framework

Figure 5.3 indicates the FNR validation for the proposed GS-RBFN technique. The proposed GS-RBFN method attained an FNR value of 0.0155. Likewise, the FNR values of the conventional RBFN, DNN, CNN, and ANN are 0.0390, 0.0923, 0.1085, and 0.1162, correspondingly. Thus, it is indicated that the proposed GS-RBFN attains much less FNR than the other prevailing approaches. Hence, the performance of the proposed framework is increased concerning accurate prediction and classification of AD. Also, regarding low FNR, the proposed approach outperforms other top-notch works.

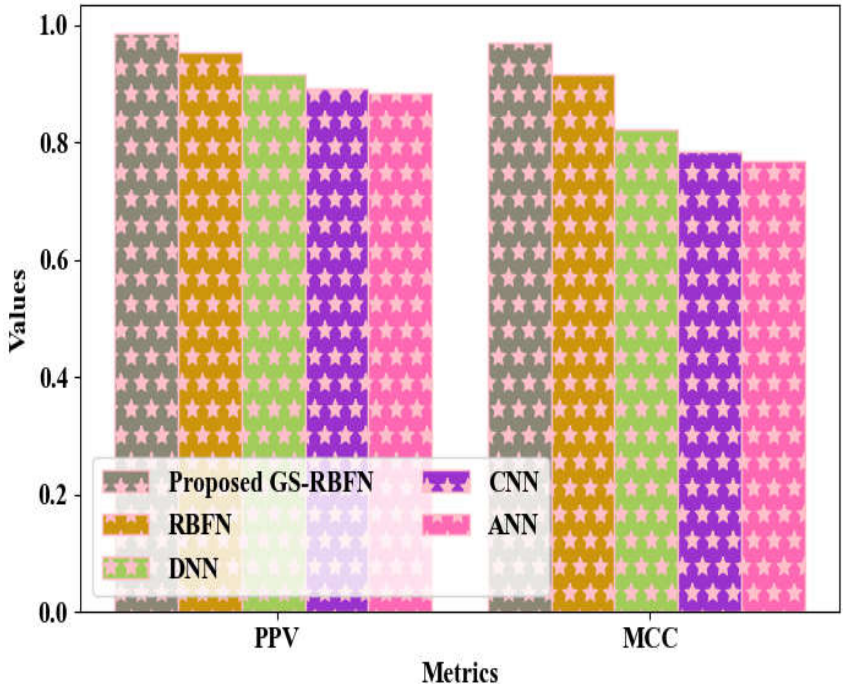

Figure 5.4: PPV and MCC estimation

In Figure 5.4, the estimation of the Positive Predictive Value (PPV) and Matthews CC (MCC) for the proposed GS-RBFN technique is carried out. The proposed GS-RBFN technique's PPV and MCC values are 0.98 and 0.96, correspondingly. Additionally, the conventional RBFN, DNN, CNN, and ANN methods obtained PPV values of 0.95, 0.91,0.89, and 0.88 and MCC values of 0.91, 0.82, 0.78, and 0.76, correspondingly. Therefore, these outcomes proved that the proposed framework had higher PPV and MCC compared to other conventional approaches. This high PPV and MCC indicate the higher performance of the proposed approach concerning the effective AD classification.

Table 5.6: Efficiency validation of the proposed GS-RBFN method

Technique	**Efficiency (%)**
Proposed BLSAOWS	98
WSA	95
OT	93
RGS	91
AC	87

Table 5.6 indicates the proposed BLSAOWS's efficiency by comparing it with several prevailing techniques like Active Contour (AC), Watershed Segmentation Algorithm (WSA), Region Growing Segmentation (RGS), and Otsu Threshold (OT). The segmentation process of the proposed framework is enhanced due to the integration of the WT approach. This integration also augments the efficiency of the proposed framework by attaining 98% efficiency compared to other conventional approaches. Also, the conventional WSA, OT, RGS, and AC achieved an efficiency of 95%, 93%, 91%, and 87%, respectively. So, as per these results, the proposed framework exhibited better segmentation techniques with high efficiency than the other traditional techniques.

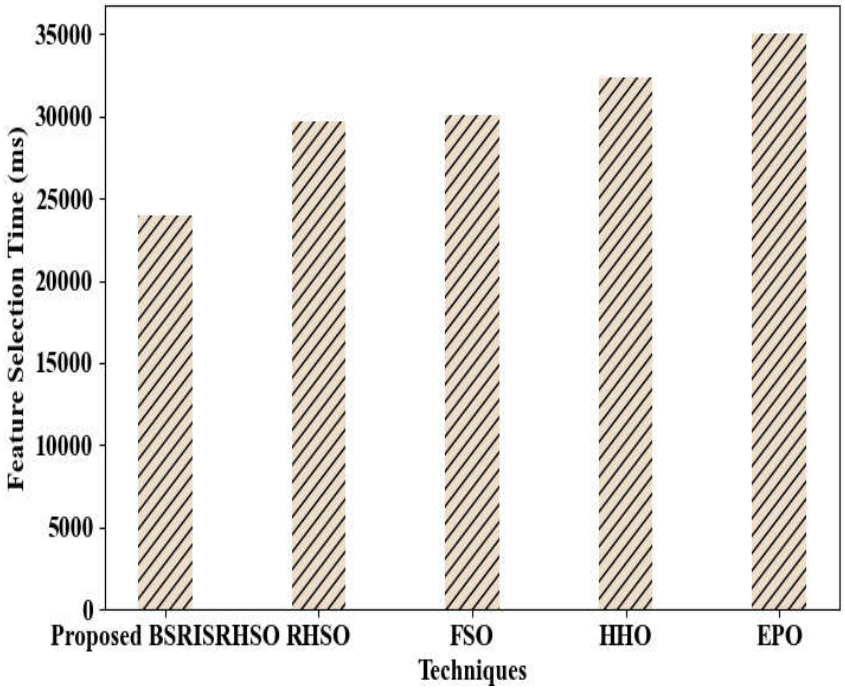

Figure 5.5: Feature selection time analysis for the proposed technique

In Figure 5.5, the FS time of the proposed BSRISRHSO technique and the conventional methods like Firebug Swarm Optimization (FSO), Rock Hyrax Swarm Optimization (RHSO), Harris Hawks Optimization (HHO), along with Emperor Penguin Optimizer (EPO) is demonstrated. The proposed BSRISRHSO technique takes 24012ms to select features, which is much less than the other existing approaches. Additionally, the proposed approach took much less time for selecting

features due to the incorporation of BSRIS. Thus, the selection of optimum boundary values increases the proposed framework's performance for the accurate classification of AD when compared to other top-notch techniques.

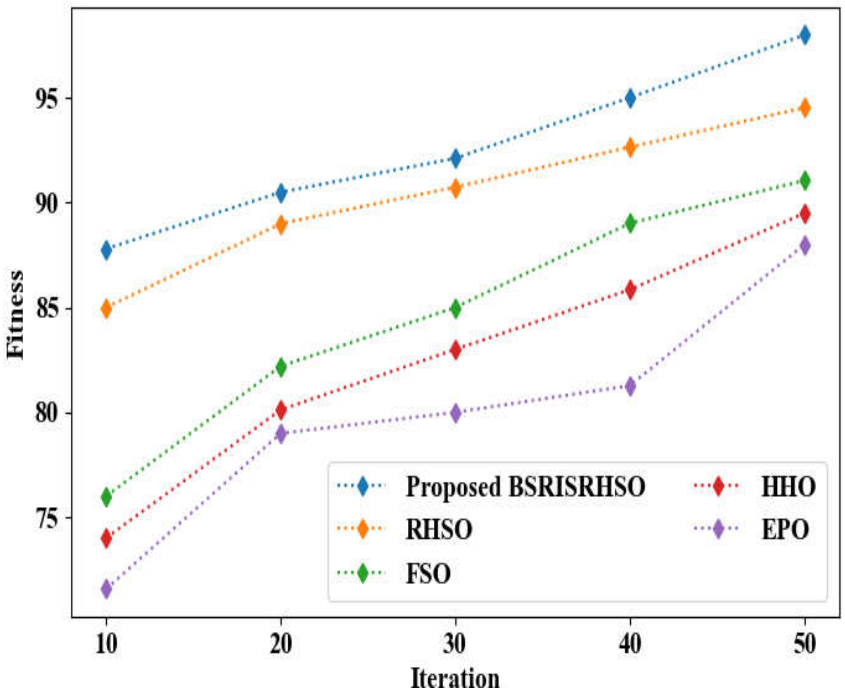

Figure 5.6: Fitness calculation for the proposed method

In Figure 5.6, the fitness calculation of the proposed BSRISRHSO approach and several conventional approaches is illustrated. Here, by effectively addressing the convergence challenge, the proposed BSRISRHSO technique attained very high fitness values. Moreover, the proposed technique's fitness values increase as the iteration count increases owing to the selection of optimum boundary values. Furthermore, over 50 iterations, the fitness value of the proposed BSRISRHSO technique is 98%, whereas the fitness value of the conventional RHSO, FSO, HHO, and EPO are 94.53%, 91.06%, 89.5%, and 88%, respectively. Hence, as per these experiential outcomes, the proposed framework's performance increases in terms of high fitness values in selecting optimal features for the accurate classification of AD.

5.8 Effectiveness Evaluation for the Dominant AD Stage and Risk Prediction Framework Using Tadpole Dataset

Here, the effectiveness of the 2nd implementation work is assessed centered on the results analysis of the proposed techniques and several prevailing approaches. Here, the proposed work's performance analysis is made by comparing it with some conventional techniques. The proposed framework encompasses the ranking phase, RS prediction phase, and brain shrinkage measurement phase. Additionally, the efficacy is assessed for the proposed Deep-AD$_3$-Net technique based on the classification of three stages of AD.

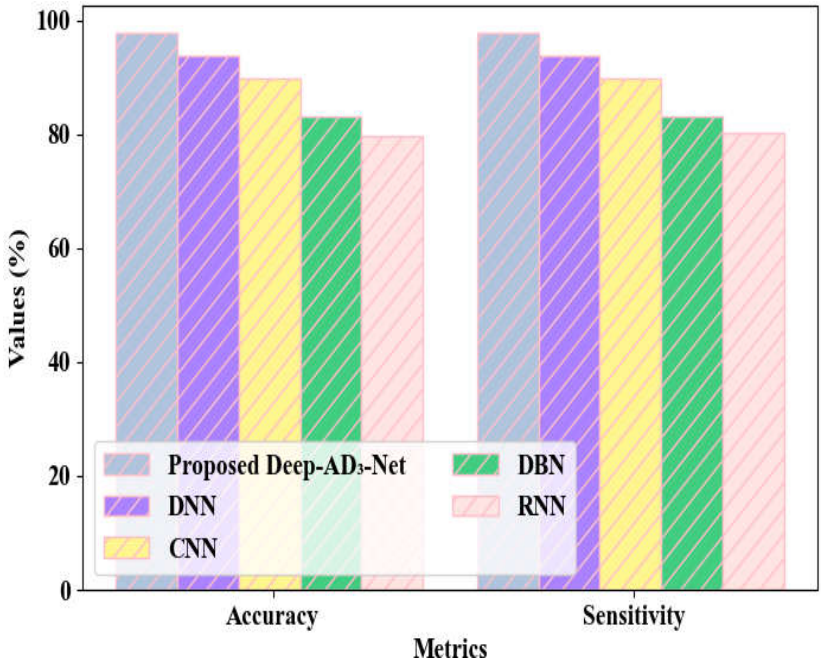

Figure 5.7: Accuracy and Sensitivity analysis for the proposed Deep-AD$_3$-Net model

Figure 5.7 indicates the accuracy and sensitivity of the proposed Deep-AD$_3$-Net. This figure indicates that the proposed Deep-AD$_3$-Net framework achieves an accuracy of 97.65% and a sensitivity of 97.66%. The existing DNN, CNN, Deep Belief Network (DBN), and RNN achieved an accuracy of 93.80%, 89.71%, 83.12%, and 79.67% and sensitivity of 93.77%, 89.64%, 83.01%, and 80.10%, correspondingly. Therefore, as per these results, the proposed framework had better performance in the classification of numerous stages of AD with higher accuracy and sensitivity. This high accuracy and sensitivity augmented the proposed

framework's effectiveness by reducing the number of false negatives and missed cases of disease.

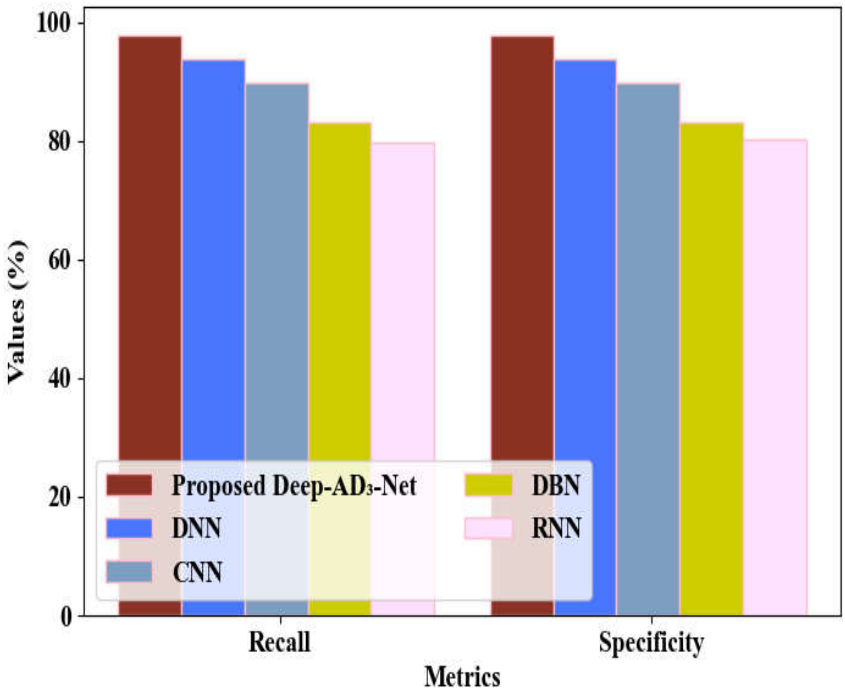

Figure 5.8: Recall and Specificity Evaluation

The recall and specificity value of the proposed Deep-AD$_3$-Net and various conventional approaches are signified in Figure 5.8. According to this figure, the proposed Deep-AD$_3$-Net technique had a much higher recall and specificity than the other prevailing techniques. These high recall and specificity increase the proposed framework's classification performance by producing low false positives. Hence, the recall values of the proposed Deep-AD$_3$-Net, DNN, CNN, DBN, and RNN are 97.66%, 93.77%, 89.64%, 83.01%, and 80.10%, respectively. Therefore, the proposed Deep-AD$_3$-Net performs better than other conventional techniques with high recall and specificity.

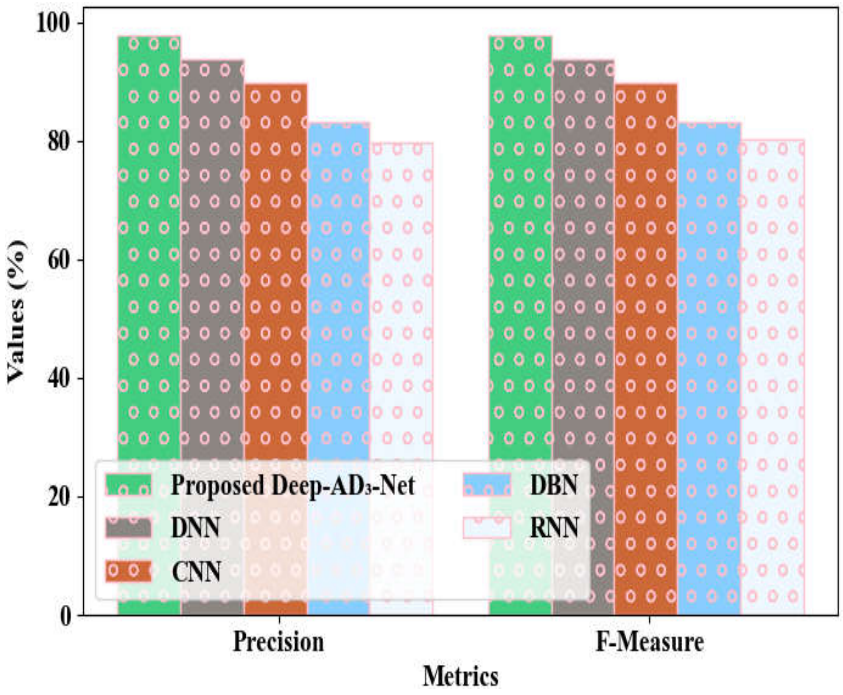

Figure 5.9: Precision and f-measure analysis

In Figure 5.9, the performance investigation of the Deep-AD$_3$-Net approach with the prevailing approaches regarding f-measure and precision is depicted. The Deep-AD$_3$-Net technique has high precision, i.e., 4%, 8%, 17%, and 21% higher than DNN, CNN, DBN, together with RNN, respectively. As per the outcome, RNN achieves a very low precision value. Hence, the Deep-AD$_3$-Net attains a higher precision value. Furthermore, the proposed Deep-AD-Net model achieves a precision of 97.63% and an f-measure of 97.52%. F-measure is a measure merging precision and recall for obtaining the average rate of such measures. The Deep-AD$_3$-Net approach has a higher average f-measure (97%) than the conventional approaches.

Table 5.7: Computation time and training time calculation

Methods	Computation Time (ms)	Training time (ms)
Proposed Deep-AD$_3$-Net	9012	36348
DNN	11003	39528
CNN	12017	49013
DBN	13012	55051
RNN	15013	60012

In Table 5.7, the Deep-AD$_3$-Net technique's performance analysis with the existing approaches, such as DNN, CNN, DBN, along with RNN grounded on the computation time as well as training time is illustrated. The proposed approach obtains a computation time of 9012 ms, which is 1991 and 4000 ms lower compared to the DNN and DBN, respectively. From the overall outcome, RNN displays higher computation and training time, proving that the Deep-AD$_3$-Net approach consumes lower computation time than other methods. The Deep-AD$_3$-Net method has a 36348 ms training time, which is 23664 and 12665 ms lower when contrasted to the RNN and conventional CNN techniques, respectively. Therefore, the proposed framework attains good training time.

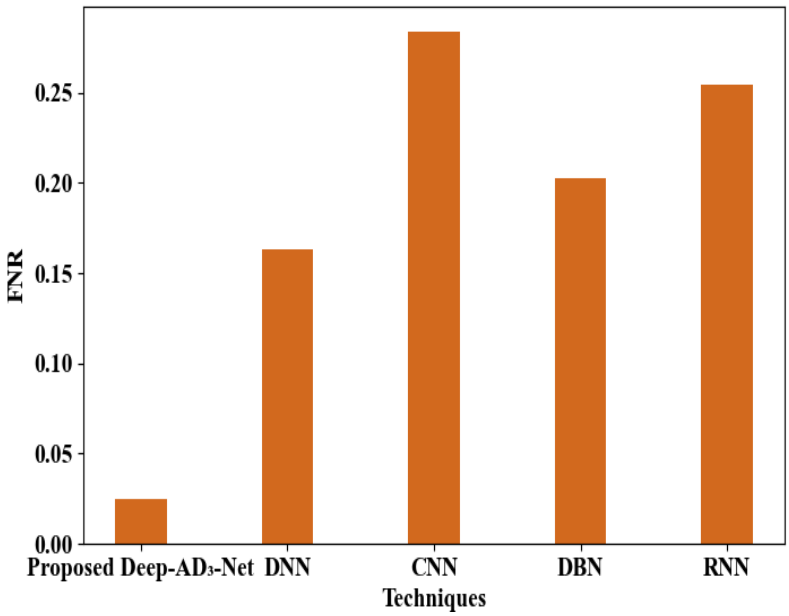

Figure 5.10: FNR estimation

Figure 5.10 indicates the proposed Deep-AD$_3$-Net's FNR estimation. According to this figure, the FNR value of the proposed Deep-AD$_3$-Net is 0.0246, whereas the DNN, CNN, DBN, and RNN had an FNR value of 0.1629, 0.2836, 0.2029, and 0.2543, respectively. Thus, this result depicted that the proposed method attained a very low FNR when analogized to the other conventional techniques. Thus, the proposed framework's increased performance regarding the prediction and

classification of AD is proven. Also, the low FNR can aid in ensuring that fewer cases of AD are missed, and the low FNR is considered as highly sensitive.

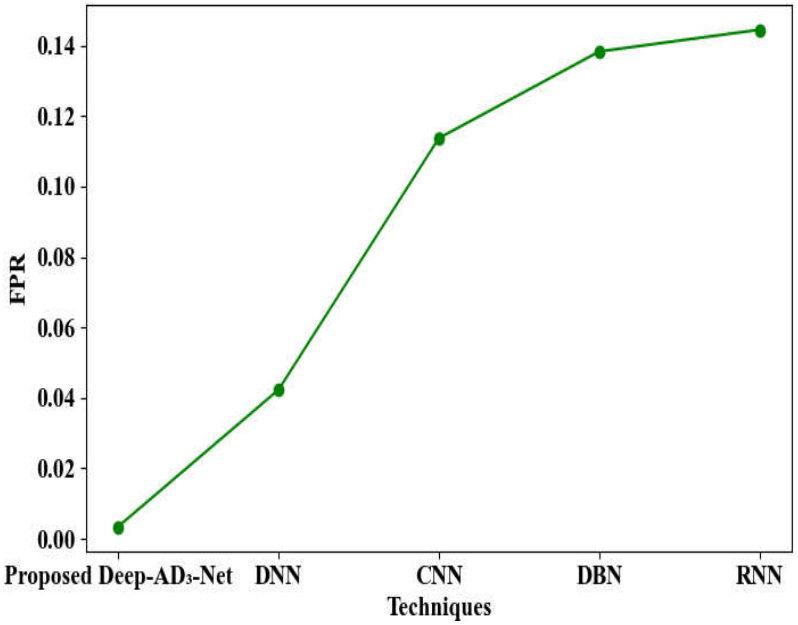

Figure 5.11: FPR evaluation of the proposed Deep-AD_3-Net

In Figure 5.11, the proposed Deep-AD_3-Net's FPR value is illustrated. The figure illustrates the FPR value of the proposed technique and the other conventional techniques in terms of AD classification. Also, when compared to the other conventional techniques, namely CNN, DNN, DBN, as well as RNN, the proposed technique had a very low FPR. The proposed framework attained good performance results in the classification of AD stages owing to the layer technique's integration. Also, the proposed framework attained higher accuracy and trustworthiness due to the low FPR, which can lead to better diagnoses. In contrast, the FPR values of the proposed Deep-AD_3-Net, and the existing DNN, CNN, DBN, along with RNN are 0.0034 and 0.0423, 0.1137, 0.1383, and 0.1444, respectively. Thus, the proposed Deep-AD_3-Net performs superior to other conventional techniques.

5.9 Comparative Evaluation of the Proposed Works

This section shows a comparative analysis of the 1st and 2nd implementations of the proposed framework with the other prevailing approaches. Here, the performance

comparison is carried out for the proposed works and the conventional techniques concerning objective, technique, accuracy, precision, and f-measure.

Table 5.8: Comprehensive analysis of the proposed works with several conventional techniques

Reference	Objective	Technique	Accuracy (%)	Precision (%)	F-measure (%)
Proposed work 1	Early prediction and classification of AD using ADNI brain MRI images	GS-RBFN	98.45	98.44	98.44
Proposed work 2	AD stage and risk prediction framework using the TADPOLE	Deep-AD_3-Net	97.65	97.63	97.52
(Ashtari-Majlan et al., 2022)	Classification of progressive MCI in AD utilizing structural MRI images	Multi-stream CNN	97	-	97.66
(Buvaneswari & Gayathri, 2021)	DL-centric segmentation in the AD classification	Residual Network-101 (ResNet-101)	96.3	-	-
(Fathi et al., 2024)	Early diagnosis of AD utilizing MRI images	Weighted Probability-Based Ensemble Method (WPBEM).	98.57	-	-
(Lin et al., 2021)	Multiclass diagnosis of AD stages utilizing the scoring approach for multimodal data	Linear Discriminant Analysis (LDA)-based scoring strategy	66.7	-	64.9
(Irfan et al., 2024)	AD time series analysis	Multivariate Long Short-Term Memory (M-LSTM)	82	85.50	82.66
(Sethuraman et al., 2023)	Predicting AD using resting-state fMRI	Deep Neuro-Functional Networks	96.61	-	-

Table 5.8 exhibits the comparative investigation of the proposed works and numerous conventional techniques. Regarding the objective, technique, accuracy, precision, and f-measure, the proposed works' 1st and 2nd implementations are compared with some conventional techniques. The Mona (Ashtari-Majlan et al., 2022) attains 97% accuracy and 97.66% f-measure, which utilizes the multistream CNN technique to classify progressive MCI in AD. Moreover, this table illustrates the performance of (Buvaneswari & Gayathri, 2021), which utilized Residual Network-101 for the classification of AD. But, it attained very low accuracy (96.3). Also, to early predict and diagnose AD, (Fathi et al., 2024) and (Sethuraman et al., 2023) utilized WPBEM and Deep Neuro-Functional Networks techniques, respectively. When compared to the proposed approach, both works attained a very low accuracy, such as 98.57% and 96.61%, respectively. Furthermore, for the multiclass diagnosis of AD stages, 66.7% and 64.9% of accuracy and f-measure are attained by (Lin et al., 2021). This outcome is very low than the proposed and other prevailing works. Additionally, for AD time series analysis, the MLSTM technique attained 82% accuracy, 85.50% precision, and 82.66% f-measure. Hence, as per the above outcome, the proposed framework had high accuracy, precision, and f-measure for the early prediction, classification, and RS prediction of AD. Likewise, to accurately predict and classify AD, the proposed frameworks outperform the other prevailing methodologies.

5.10 Findings

The performance of the 1st and 2nd implementations of the proposed framework is assessed in this chapter by contrasting it with the traditional methods for validating the performance in AD prediction and classification. As per the performance of the 1st implementation of the proposed framework, the proposed work performs superior to the other prevailing techniques. Here, the performance evaluation is made by evaluating the proposed GS-RBFN, BLSAOWS, and BSRISRHSO techniques regarding classification, segmentation, and FS. According to this evaluation, the proposed GS-RBFN outperforms the other prevailing techniques by achieving accuracy, precision, training time, and computation time of 98.45%, 98.44%,

29539ms, and 14876ms, respectively. In addition, the proposed BLSAOWS technique attains 98% efficiency, proving that the proposed work is more efficient in segmenting brain images than the other existing techniques. Lastly, the proposed BSRISRHSO technique's performance is assessed for choosing the features to classify AD. For this assessment, the BSRISRHSO technique is analogized with some conventional techniques regarding time consumed for selecting features and fitness calculation. Here, the proposed BSRISRHSO technique attained 24012ms FS time and 98% fitness, which are superior to other top-notch works.

Now, the efficiency of the 2nd implementation of the proposed model is estimated regarding the classification of numerous stages of AD. Here, centered on analyzing the proposed Deep-AD_3-Net technique's performance, the proposed framework's performance is validated. This technique proved that the proposed model outperformed other prevailing methodologies concerning the accurate classification of AD stages, namely AD-mild, AD-moderate, and AD-severity. Also, this Deep-AD_3-Net had an accuracy, computation time, and training time of 97.65%, 9012ms, and 36348ms, respectively. As per these results, the proposed work had superior results in the accurate classification of AD stages compared to other conventional approaches. Also, the 1st and 2nd implementations of the proposed framework perform better than other prevailing approaches, which is also proven by the comparative evaluation.

CHAPTER 6
CONCLUSION AND FUTURE SCOPE

AD results in brain shrinkage and brain cells eventually die. AD is the major common reason for dementia, which is a progressive decline in thinking, memory, social skills, and behavior, thus affecting the person's capability of functioning. Thus, it is significant to early predict and diagnose AD. To effectively predict and classify AD, various prevailing works were developed. Nevertheless, due to overfitting issues, vulnerability issues, spoofing effects, and generalization ability in small datasets, conventional works produced inaccurate classification results. Thus, in this thesis, two frameworks were implemented to effectively predict and classify AD.

An efficient GS-RBFN model was employed in the first implementation to predict and classify AD in the early stage. Here, by using the proposed BLSAWSA approach, the pre-processed images were partitioned into WM, GM, and CSF with 98% efficiency. Then, to effectively learn the images' patterns, the segmented images were continued with the morphological operation as well as the augmentation process. The image representation extraction was performed after a data augmentation process based on patch segmentation, feature patch selection, and concatenation. Then, to accurately classify AD, the proposed BSRISRHSO technique was implemented for selecting the optimal features, which selected optimal features within 24012ms time and attained 98% fitness. Lastly, the classification operation was obtained using the proposed GS-RBFN technique, which accurately classified features into MCI, CN, and AD. In addition, this technique effectively classified AD with attaining 98.45% accuracy and 98.44% precision. Hence, as per the experimental outcomes, the research method obtained higher supremacy in AD prediction and classification when contrasted with the other top-notch works.

Likewise, using the Deep-AD$_3$-Net, an effective AD stage and risk prediction model was presented for the 2nd implementation. Here, the given dataset was investigated

and some variables were extracted. After that, the proposed framework carried out the ranking, RS prediction, and brain shrinkage measurement phases effectively. After achieving those phases, the proposed Deep-AD_3-Net technique was employed for classifying AD stages. Also, based on accuracy, specificity, sensitivity, recall, precision, and f-measure, the proposed model's performance was investigated and compared with the existing techniques. This technique effectively classified AD stages with accuracy, sensitivity, specificity, and f-measure of 97.65%, 97.66%, 97.65%, and 97.52%, correspondingly. Moreover, when analogized to the other conventional techniques, the proposed methodology had a higher FNR (0.00246) and FPR (0.00346) value. Also, the proposed technique took much less time for training (36348ms) and computation (9012ms). As per these validated outcomes, the proposed framework performed superior to other prevailing works in accurate RS prediction and classification of AD. In addition, the proposed mechanisms offered significant insight into predicting as well as classifying AD in the early stage.

6.1 Limitation and Future Scope

In this thesis, the methodologies developed for predicting and classifying AD have demonstrated significant improvements in accuracy and efficiency. Yet, there is potential for further advancements in this field. Future research can investigate the application of these models to larger, more different datasets to enhance their generalizability and robustness across different populations. Furthermore, a more in-depth understanding of AD progression and risk factors can be provided by integrating other data modalities, such as genomic data or lifestyle factors. Another promising area is developing real-time, adaptive models, which can be employed in clinical settings for early intervention. Also, for practically deploying these models in HC environments, continuous improvement of ML and DL methods, particularly in interpretability and computational efficiency, will be crucial. In addition, a new training strategy can be developed in which a model can be trained in parallel with different datasets simultaneously.

The study's main limitations include reliance on publicly available datasets with limited demographic diversity and restricted validation across clinical centres. Future work will focus on expanding dataset diversity, external validation using OASIS and AIBL cohorts, and improving model explainability for clinical integration.

The study will be enhanced in the future by segmenting the most significant tissues for the efficient classification of multiple stages of AD. Furthermore, this work will be enhanced by integrating the more advanced DL approaches to further increase the model's reliability. Then, the tree structure and graphical forms will be concentrated to demonstrate the brain regions, ensuring the model supremacy. Conversely, a rule-based treatment plan recommendation system will be introduced to ensure the patient's lifetime.

Similarly, the efficient network layers and activation functions are also introduced to upgrade the learning process of the neuron. Likewise, more number of samples and features related to brain MRI is also considered to elevate the classifier's accuracy. Collectively, the proposed model will be improved in the future by considering the aforementioned future enhancement strategies. This technique may assist a model in adopting collective features from various sources.

REFERENCES

AbdulAzeem, Y., Bahgat, W. M., & Badawy, M. (2021). A CNN based framework for classification of Alzheimer's disease. *Neural Computing and Applications*, *33*, 10415-10428. https://doi.org/10.1007/s00521-021-05799-w

Aggarwal, H., Chaware, S., & Aggarwal, H. (2022). A critical study on the impact of dementia on older people undergoing treatment in care homes. *Cureus*, *14*(10). https://doi.org/10.7759/cureus.30056

Altaf, T., Anwar, S. M., Gul, N., Majeed, M. N., & Majid, M. (2018). Multi-class alzheimer's disease classification using image and clinical features. *Biomedical Signal Processing and Control*, *43*, 64–74. https://doi.org/10.1016/j.bspc.2018.02.019

An, N., Ding, H., Yang, J., Au, R., & Ang, T. F. A. (2020). Deep ensemble learning for alzheimer's disease classification. *Journal of Biomedical Informatics*, *105*, 1–11. https://doi.org/10.1016/j.jbi.2020.103411

Anantapur, M., & Patil, V. C. (2021). PUSR: Position Update Secure Routing protocol for MANET. *International Journal of Intelligent Engineering and Systems*, *14*(1), 93–102. https://doi.org/10.22266/IJIES2021.0228.10

Ashtari-Majlan, M., Seifi, A., & Dehshibi, M. M. (2022). A Multi-Stream Convolutional Neural Network for Classification of Progressive MCI in Alzheimer's Disease Using Structural MRI Images. *IEEE Journal of Biomedical and Health Informatics*, *26*(8), 3918–3926. https://doi.org/10.1109/JBHI.2022.3155705

Basaia, S., Agosta, F., Wagner, L., Canu, E., Magnani, G., Santangelo, R., & Filippi, M. (2019). Automated classification of Alzheimer's disease and mild cognitive impairment using a single MRI and deep neural networks. *NeuroImage: Clinical*, *21*, 1–8. https://doi.org/10.1016/j.nicl.2018.101645

Basheer, S., Bhatia, S., & Sakri, S. B. (2021). Computational Modeling of Dementia Prediction Using Deep Neural Network: Analysis on OASIS Dataset. *IEEE Access*, *9*, 42449–42462. https://doi.org/10.1109/ACCESS.2021.3066213

Baytas, I. M. (2024). Predicting Progression from Mild Cognitive Impairment to Alzheimer's Dementia with Adversarial Attacks. IEEE Journal of Biomedical and Health Informatics, 28(6), 3750–3761. https://doi.org/10.1109/JBHI.2024.3373703

Beheshti, I., Demirel, H., & Matsuda, H. (2017). Classification of Alzheimer's disease and prediction of mild cognitive impairment-to-Alzheimer's conversion from structural magnetic resource imaging using feature ranking and a genetic algorithm. *Computers in Biology and Medicine*, *83*, 1–53. https://doi.org/10.1016/j.compbiomed.2017.02.011

Bhagwat, N., Viviano, J. D., Voineskos, A. N., & Chakravarty, M. M. (2018). Modeling and prediction of clinical symptom trajectories in Alzheimer's disease using longitudinal data. *PLoS Computational Biology*, *14*(9), 1–25. https://doi.org/10.1371/journal.pcbi.1006376

Bi, X., Li, S., Xiao, B., Li, Y., Wang, G., & Ma, X. (2020). Computer aided Alzheimer's disease diagnosis by an unsupervised deep learning technology. *Neurocomputing*, *392*(1–27), 296–304. https://doi.org/10.1016/j.neucom.2018.11.111

Bohle, M., Eitel, F., Weygandt, M., & Ritter, K. (2019). Layer-wise relevance propagation for explaining deep neural network decisions in MRI-based Alzheimer's disease classification. *Frontiers in Aging Neuroscience*, *10*, 1–17. https://doi.org/10.3389/fnagi.2019.00194

Bondada, P., Samanta, D., Chaudhry, S. A., Zikria, Y. Bin, & Ishmanov, F. (2021). Efficient neighbour feedback based trusted multi authenticated node routing model for secure data transmission. *Sustainability (Switzerland)*, *13*(23), 1–14. https://doi.org/10.3390/su132313296

Breijyeh, Z., & Karaman, R. (2020). Comprehensive review on Alzheimer's disease: causes and treatment. *Molecules*, *25*(24), 5789. http://dx.doi.org/10.3390/ molecules 25245789

Bringas, S., Salomon, S., Duque, R., Lage, C., & Montana, J. L. (2020). Alzheimer's Disease stage identification using deep learning models. *Journal of Biomedical Informatics*, *109*, 1–9. https://doi.org/10.1016/j.jbi.2020.103514

Buvaneswari, P. R., & Gayathri, R. (2021). Deep Learning-Based Segmentation in Classification of Alzheimer's Disease. *Arabian Journal for Science and Engineering*, *46*(6), 5373–5383. https://doi.org/10.1007/s13369-020-05193-z

Chaddad, A., Desrosiers, C., & Niazi, T. (2018). Deep radiomic analysis of MRI related to alzheimer's disease. *IEEE Access*, *6*, 58213–58221. https://doi.org/10.1109/ ACCESS.2018.2871977

Chui, K. T., Gupta, B. B., Alhalabi, W., & Alzahrani, F. S. (2022). An MRI Scans-Based Alzheimer's Disease Detection via Convolutional Neural Network and Transfer Learning. *Diagnostics*, *12*(7), 1–14. https://doi.org/10.3390/diagnostics12071531

Cui, W., Ma, Y., Ren, J., Liu, J., Ma, G., Liu, H., & Li, Y. (2023). Personalized Functional Connectivity Based Spatio-Temporal Aggregated Attention Network for MCI Identification. IEEE Transactions on Neural Systems and Rehabilitation Engineering, 31, 2257–2267. https://doi.org/10.1109/TNSRE.2023.3271062

Cummings, J. (2021). New approaches to symptomatic treatments for Alzheimer's disease. *Molecular Neurodegeneration*, *16*, 1-13. https://doi.org/10.1186/s13024-021-00424-9

Dhende, S., & Shirbahadurkar, S. (2022). MACO-DHKE Based Secure Data Transmission in MANETs. *International Journal of Electrical and Computer Engineering Systems*, *13*(4), 245–252. https://doi.org/10.32985/IJECES.13.4.1

Divya, R., & Kumari, R. S. S. (2021). Genetic algorithm with logistic regression feature selection for alzheimer's disease classification. *Neural Computing and Applications*, *33*(14), 8435–8444. https://doi.org/10.1007/s00521-020-05596-x

Dubois, B., Villain, N., Frisoni, G. B., Rabinovici, G. D., Sabbagh, M., Cappa, S., ... & Feldman, H. H. (2021). Clinical diagnosis of Alzheimer's disease: recommendations

of the International Working Group. *The Lancet Neurology*, *20*(6), 484-496. https://doi.org/10.1016/S1474-4422(21)00066-1 .

Duc, N. T., Ryu, S., Qureshi, M. N. I., Choi, M., Lee, K. H., & Lee, B. (2020). 3D-deep learning based automatic diagnosis of alzheimer's disease with Joint MMSE prediction using resting-state fMRI. *Neuroinformatics*, *18*(1), 71–86. https://doi.org/10.1007/s12021-019-09419-w

Ebrahimi, A., & Luo, S. (2021). Convolutional neural networks for alzheimer's disease detection on MRI images. *Journal of Medical Imaging*, *8*(2), 1–18. https://doi.org/10.1117/1.jmi.8.2.024503

Ebrahimi, A., Luo, S., & Chiong, R. (2021). Deep sequence modelling for alzheimer's disease detection using MRI. *Computers in Biology and Medicine*, *134*, 1–26. https://doi.org/10.1016/j.compbiomed.2021.104537

EL-Geneedy, M., Moustafa, H. E. D., Khalifa, F., Khater, H., & AbdElhalim, E. (2023). An MRI-based deep learning approach for accurate detection of alzheimer's disease. *Alexandria Engineering Journal*, *63*, 211–221. https://doi.org/10.1016/j.aej.2022.07.062

El-Sappagh, S., Abuhmed, T., Islam, S. M. R., & Kwak, K. S. (2020). Multimodal multitask deep learning model for alzheimer's disease progression detection based on time series data. *Neurocomputing*, *412*, 197–215. https://doi.org/10.1016/j.neucom.2020.05.087

El-Sappagh, S., Alonso, J. M., Islam, S. M. R., Sultan, A. M., & Kwak, K. S. (2021). A multilayer multimodal detection and prediction model based on explainable artificial intelligence for Alzheimer's disease. *Scientific Reports*, *11*(1), 1–26. https://doi.org/10.1038/s41598-021-82098-3

Fan, Z., Xu, F., Qi, X., Li, C., & Yao, L. (2020). Classification of Alzheimer's disease based on brain MRI and machine learning. *Neural Computing and Applications*, *32*(7), 1–10. https://doi.org/10.1007/s00521-019-04495-0

Fathi, S., Ahmadi, A., Dehnad, A., Almasi-Dooghaee, M., & Sadegh, M. (2024). A Deep Learning-Based Ensemble Method for Early Diagnosis of Alzheimer's Disease using MRI Images. *Neuroinformatics*, *22*(1), 89–105. https://doi.org/10.1007/s12021-023-09646-2

Fuchs, T. (2020). Embodiment and personal identity in dementia. *Medicine, Health Care and Philosophy*, *23*(4), 665-676. https://doi.org/10.1007/s11019-020-09973-0

Gao, X. R., Chiariglione, M., Qin, K., Nuytemans, K., Scharre, D. W., Li, Y. J., & Martin, E. R. (2023). Explainable machine learning aggregates polygenic risk scores and electronic health records for Alzheimer's disease prediction. *Scientific Reports*, *13*(1), 1–12. https://doi.org/10.1038/s41598-023-27551-1

Ghazal, T. M., Abbas, S., Munir, S., Khan, M. A., Ahmad, M., Issa, G. F., Zahra, S. B., Khan, M. A., & Hasan, M. K. (2022). Alzheimer disease detection empowered with transfer learning. *Computers, Materials and Continua*, *70*(3), 5005–5019. https://doi.org/10.32604/cmc.2022.020866

Guan, H., Wang, C., & Tao, D. (2021). MRI-based alzheimer's disease prediction via

distilling the knowledge in multi-modal data. *NeuroImage*, *244*, 1–14. https://doi.org/10.1016/j.neuroimage.2021.118586

Gupta, Y., Lama, R. K., & Kwon, G. R. (2019). Prediction and classification of alzheimer's disease based on combined features from apolipoprotein-E genotype, cerebrospinal fluid, MR, and FDG-PET imaging biomarkers. *Frontiers in Computational Neuroscience*, *13*, 1–18. https://doi.org/10.3389/fncom.2019.00072

Hai, T., Zhou, J., Lu, Y., Jawawi, D., Wang, D., Onyema, E. M., & Biamba, C. (2023). Enhanced security using multiple paths routine scheme in cloud-MANETs. *Journal of Cloud Computing*, *12*(1), 1–23. https://doi.org/10.1186/s13677-023-00443-5

Hajamohideen, F., Shaffi, N., Mahmud, M., Subramanian, K., Al Sariri, A., Vimbi, V., & Abdesselam, A. (2023). Four-way classification of Alzheimer's disease using deep Siamese convolutional neural network with triplet-loss function. *Brain Informatics*, *10*(1), 1–13. https://doi.org/10.1186/s40708-023-00184-w

Hameed, S., Fuh, J. L., Senanarong, V., Ebenezer, E. G. M., Looi, I., Dominguez, J. C., ... & Simon, O. (2020). Role of fluid biomarkers and PET imaging in early diagnosis and its clinical implication in the management of Alzheimer's disease. *Journal of Alzheimer's disease reports*, *4*(1), 21-37. https://doi.org/10.3233/ADR-190143

Hernandez, M., Ramon-Julvez, U., & Ferraz, F. (2022). Explainable AI toward understanding the performance of the top three TADPOLE Challenge methods in the forecast of Alzheimer's disease diagnosis. In PLoS ONE (Vol. 17). https://doi.org/10.1371/journal.pone.0264695

Hernandez-Lorenzo, L., Hoffmann, M., Scheibling, E., List, M., Matias-Guiu, J. A., & Ayala, J. L. (2022). On the limits of graph neural networks for the early diagnosis of Alzheimer's disease. *Scientific Reports*, *12*(1), 1–13. https://doi.org/10.1038/s41598-022-21491-y

Ho, N. H., Yang, H. J., Kim, J., Dao, D. P., Park, H. R., & Pant, S. (2022). Predicting progression of Alzheimer's disease using forward-to-backward bi-directional network with integrative imputation. Neural Networks, 150, 422–439. https://doi.org/10.1016/j.neunet.2022.03.016

Hojjati, S. H., Ebrahimzadeh, A., & Babajani-Feremi, A. (2019). Identification of the early stage of alzheimer's disease using structural mri and resting-state fmri. *Frontiers in Neurology*, *10*, 1–12. https://doi.org/10.3389/fneur.2019.00904

Hong, X., Lin, R., Yang, C., Cai, C., & Clawson, K. (2020). ADPM: An alzheimer's disease prediction model for time series neuroimage analysis. *IEEE Access*, *8*, 62601–62609. https://doi.org/10.1109/ACCESS.2020.2979969

Hong, X., Lin, R., Yang, C., Zeng, N., Cai, C., Gou, J., & Yang, J. (2019). Predicting alzheimer's disease using LSTM. *IEEE Access*, *7*, 80893–80901. https://doi.org/10.1109/ACCESS.2019.2919385

Horie, K., Barthélemy, N. R., Sato, C., & Bateman, R. J. (2021). CSF tau microtubule binding region identifies tau tangle and clinical stages of Alzheimer's disease. *Brain*, *144*(2), 515-527. https://doi.org/10.1093/brain/awaa373

Iddi, S., Li, D., Aisen, P. S., Rafii, M. S., Thompson, W. K., & Donohue, M. C. (2019).

Predicting the course of Alzheimer's progression. *Brain Informatics*, *6*(1), 1–18. https://doi.org/10.1186/s40708-019-0099-0

Irfan, M., Shahrestani, S., & Elkhodr, M. (2024). Machine learning in neurological disorders: A multivariate LSTM and AdaBoost approach to Alzheimer's disease time series analysis. Health Care Science, 3(1), 41–52. https://doi.org/10.1002/hcs2.84

Islam, J., & Zhang, Y. (2018). Brain MRI analysis for alzheimer's disease diagnosis using an ensemble system of deep convolutional neural networks. *Brain Informatics*, *5*(2), 1–14. https://doi.org/10.1186/s40708-018-0080-3

Iulita, M. F., Chavez, D. G., Christensen, M. K., Tamayo, N. V., Plana-Ripoll, O., Rasmussen, S. A., ... & Fortea, J. (2022). Association of Alzheimer disease with life expectancy in people with Down syndrome. *JAMA network open*, *5*(5), e2212910-e2212910. https://doi.org/10.1001/jamanetworkopen.2022.12910

Jain, R., Jain, N., Aggarwal, A., & Hemanth, D. J. (2019). Convolutional neural network based alzheimer's disease classification from magnetic resonance brain images. *Cognitive Systems Research*, *57*, 147–159. https://doi.org/10.1016/j.cogsys.2018.12.015

Jin, M., & Deng, W. (2018). Predication of different stages of alzheimer's disease using neighborhood component analysis and ensemble decision tree. *Journal of Neuroscience Methods*, *302*, 1–32. https://doi.org/10.1016/j.jneumeth.2018.02.014

Jung, W., Jun, E., Suk, H. Il, & Alzheimer's Disease Neuroimaging Initiative. (2021). Deep recurrent model for individualized prediction of Alzheimer's disease progression. NeuroImage, 237, 1–20. https://doi.org/10.1016/j.neuroimage.2021.118143

Kang, H., & Kang, D. Y. (2023). Alzheimer's Disease Prediction Using Attention Mechanism with Dual-Phase 18F-Florbetaben Images. *Nuclear Medicine and Molecular Imaging*, *57*(2), 61–72. https://doi.org/10.1007/s13139-022-00767-1

Kapoor, M., Kapoor, M., Shukla, R., & Raj Singh, T. (2021). Early diagnosis of alzheimer's disease using machine learning based methods. ACM International Conference Proceeding Series, 70–76. https://doi.org/10.1145/3474124.3474134

Kavitha, C., Mani, V., Srividhya, S. R., Khalaf, O. I., & Romero, C. A. T. (2022). Early-Stage Alzheimer's Disease Prediction Using Machine Learning Models. *Frontiers in Public Health*, *10*, 1–13. https://doi.org/10.3389/fpubh.2022.853294

Khan, N. M., Abraham, N., & Hon, M. (2019). Transfer Learning with Intelligent Training Data Selection for Prediction of Alzheimer's Disease. *IEEE Access*, *7*, 72726–72735. https://doi.org/10.1109/ACCESS.2019.2920448

Khan, R. U., Tanveer, M., & Pachori, R. B. (2021). A novel method for the classification of alzheimer's disease from normal controls using magnetic resonance imaging. *Expert Systems*, *38*(1), 1–22. https://doi.org/10.1111/exsy.12566

Khan, Y. F., Kaushik, B., Rahmani, M. K. I., & Ahmed, M. E. (2022). Stacked Deep Dense Neural Network Model to Predict Alzheimer's Dementia Using Audio Transcript Data. IEEE Access, 10, 32750–32765. https://doi.org/10.1109/ACCESS.2022.3161749

Kumar, S., Oh, I., Schindler, S., Lai, A. M., Payne, P. R., & Gupta, A. (2021). Machine learning for modeling the progression of Alzheimer disease dementia using clinical data: a systematic literature review. *JAMIA open*, *4*(3), ooab052. https://doi.org/10.1093/jamiaopen/ooab052

Lee, G., Nho, K., Kang, B., Sohn, K. A., & Kim, D. (2019). Predicting Alzheimer's disease progression using multi-modal deep learning approach. *Scientific Reports*, *9*(1), 1–12. https://doi.org/10.1038/s41598-018-37769-z

Lei, B., Yang, M., Yang, P., Zhou, F., Hou, W., Zou, W., Li, X., Wang, T., Xiao, X., & Wang, S. (2020). Deep and joint learning of longitudinal data for alzheimer's disease prediction. *Pattern Recognition*, *102*, 1–25. https://doi.org/10.1016/ j.patcog.2020.107247

Lella, E., Lombardi, A., Amoroso, N., Diacono, D., Maggipinto, T., Monaco, A., Bellotti, R., & Tangaro, S. (2020). Machine learning and DWI brain communicability networks for Alzheimer's disease detection. *Applied Sciences (Switzerland)*, *10*(3), 1–13. https://doi.org/10.3390/app10030934

Li, H., Habes, M., Wolk, D. A., & Fan, Y. (2019). A deep learning model for early prediction of Alzheimer's disease dementia based on hippocampal magnetic resonance imaging data. *Alzheimer's and Dementia*, *15*(8), 1–34. https://doi.org/10.1016/ j.jalz.2019.02.007

Li, W., Zhao, J., Shen, C., Zhang, J., Hu, J., Xiao, M., ... & Chen, M. (2022). Regional brain fusion: Graph convolutional network for alzheimer's disease prediction and analysis. *Frontiers in Neuroinformatics*, *16*, 1-12. https://doi.org/10.3389/ fninf.2022.886365

Lian, C., Liu, M., Zhang, J., & Shen, D. (2020). Hierarchical fully convolutional network for joint atrophy localization and alzheimer's disease diagnosis using structural MRI. *IEEE Transactions on Pattern Analysis and Machine Intelligence*, *42*(4), 880–893. https://doi.org/10.1109/TPAMI.2018.2889096

Lin, W., Gao, Q., Du, M., Chen, W., & Tong, T. (2021). Multiclass diagnosis of stages of Alzheimer's disease using linear discriminant analysis scoring for multimodal data. Computers in Biology and Medicine, 134, 1–8. https://doi.org/10.1016/ j.compbiomed.2021.104478

Liu, J., Li, M., Luo, Y., Yang, S., Li, W., & Bi, Y. (2021). Alzheimer's disease detection using depthwise separable convolutional neural networks. *Computer Methods and Programs in Biomedicine*, *203*, 1–10. https://doi.org/10.1016/j.cmpb.2021.106032

Liu, L., Zhao, S., Chen, H., & Wang, A. (2020). A new machine learning method for identifying Alzheimer's disease. *Simulation Modelling Practice and Theory*, *99*, 1–22. https://doi.org/10.1016/j.simpat.2019.102023

Liu, M., Cheng, D., & Yan, W. (2018). Classification of alzheimer's disease by combination of convolutional and recurrent neural networks using FDG-PET images. *Frontiers in Neuroinformatics*, *12*, 1–12. https://doi.org/10.3389/fninf.2018.00035

Liu, M., Li, F., Yan, H., Wang, K., Ma, Y., Shen, L., & Xu, M. (2020). A multi-model deep convolutional neural network for automatic hippocampus segmentation and classification in Alzheimer's disease. *NeuroImage*, *208*, 1–15.

https://doi.org/10.1016/j.neuroimage.2019.116459

Liu, W., Dong, Q., Sun, S., Shen, J., Qian, K., & Hu, B. (2023). Risk Prediction of Alzheimer's Disease Conversion in Mild Cognitive Impaired Population Based on Brain Age Estimation. *IEEE Transactions on Neural Systems and Rehabilitation Engineering*, *31*, 2468–2476. https://doi.org/10.1109/TNSRE.2023.3247590

Ljubic, B., Roychoudhury, S., Cao, X. H., Pavlovski, M., Obradovic, S., Nair, R., Glass, L., & Obradovic, Z. (2020). Influence of medical domain knowledge on deep learning for Alzheimer's disease prediction. *Computer Methods and Programs in Biomedicine*, *197*, 1–7. https://doi.org/10.1016/j.cmpb.2020.105765

Lorenzi, M., Filippone, M., Frisoni, G. B., Alexander, D. C., & Ourselin, S. (2019). Probabilistic disease progression modeling to characterize diagnostic uncertainty: Application to staging and prediction in alzheimer's disease. *NeuroImage*, *190*, 56–68. https://doi.org/10.1016/j.neuroimage.2017.08.059

Luo, Z., Xu, H., Liu, L., Ohulchanskyy, T. Y., & Qu, J. (2021). Optical imaging of beta-amyloid plaques in Alzheimer's disease. *Biosensors*, *11*(8), 255. https://doi.org/10.3390/bios11080255

Maqsood, M., Nazir, F., Khan, U., Aadil, F., Jamal, H., Mehmood, I., & Song, O. Y. (2019). Transfer learning assisted classification and detection of alzheimer's disease stages using 3D MRI scans. *Sensors*, *19*(11), 1–19. https://doi.org/10.3390/s19112645

Marinescu, R. V., Bron, E. E., Oxtoby, N. P., Young, A. L., Toga, A. W., Weiner, M. W., Barkhof, F., Fox, N. C., Golland, P., Klein, S., & Alexander, D. C. (2020). Predicting Alzheimer's disease progression: Results from the TADPOLE Challenge. Alzheimer's & Dementia, 16(4), 1–6. https://doi.org/10.1002/alz.039538

Mattsson-Carlgren, N., Janelidze, S., Palmqvist, S., Cullen, N., Svenningsson, A. L., Strandberg, O., ... & Hansson, O. (2020). Longitudinal plasma p-tau217 is increased in early stages of Alzheimer's disease. *Brain*, *143*(11), 3234-3241. https://doi.org/10.1093/brain/awaa329

McCartney, D. L., Stevenson, A. J., Walker, R. M., Gibson, J., Morris, S. W., Campbell, A., Murray, A. D., Whalley, H. C., Porteous, D. J., McIntosh, A. M., Evans, K. L., Deary, I. J., & Marioni, R. E. (2018). Investigating the relationship between DNA methylation age acceleration and risk factors for Alzheimer's disease. *Alzheimer's and Dementia: Diagnosis, Assessment and Disease Monitoring*, *10*, 429–437. https://doi.org/10.1016/j.dadm.2018.05.006

Mehdipour Ghazi, M., Nielsen, M., Pai, A., Modat, M., Jorge Cardoso, M., Ourselin, S., & Sørensen, L. (2021). Robust parametric modeling of Alzheimer's disease progression. NeuroImage, 225, 1–12. https://doi.org/10.1016 /j.neuroimage.2020 .117460

Mehmood, A., yang, S., feng, Z., wang, M., Ahmad, A. S., khan, R., Maqsood, M., & Yaqub, M. (2021). A transfer learning approach for early diagnosis of alzheimer's disease on MRI Images. *Neuroscience*, *460*, 43–52. https://doi.org/10.1016/j.neuroscience.2021.01.002

Mirzaei, S., El Yacoubi, M., Garcia-Salicetti, S., Boudy, J., Kahindo, C., Cristancho-Lacroix, V., Kerhervé, H., & Rigaud, A. S. (2018). Two-stage feature selection of

voice parameters for early alzheimer's disease prediction. *IRBM*, *39*(6), 1–6. https://doi.org/10.1016/j.irbm.2018.10.016

Muhammed, M. N., & Thiyagarajan, P. (2021). Alzheimer's classification using dynamic ensemble of classifiers selection algorithms: A performance analysis. Biomedical Signal Processing and Control, 68, 1–18. https://doi.org/10.1016/j.bspc.2021.102729

Muhammed, M. N., & Thiyagarajan, P. (2022). Feature selection using efficient fusion of Fisher Score and greedy searching for Alzheimer's classification. Journal of King Saud University - Computer and Information Sciences, 34(8), 4993–5006. https://doi.org/10.1016/j.jksuci.2020.12.009

Nakagawa, T., Ishida, M., Naito, J., Nagai, A., Yamaguchi, S., & Onoda, K. (2020). Prediction of conversion to alzheimer's disease using deep survival analysis of MRI images. *Brain Communications*, *2*(1), 1–10. https://doi.org/10.1093/braincomms/fcaa057

Nandi, A., Counts, N., Chen, S., Seligman, B., Tortorice, D., Vigo, D., & Bloom, D. E. (2022). Global and regional projections of the economic burden of Alzheimer's disease and related dementias from 2019 to 2050: A value of statistical life approach. *EClinicalMedicine*, *51*, 1-10. https://www.thelancet.com/journals/eclinm/article/PIIS2589-5370(22)00310-8/fulltext

Nguyen, M., He, T., An, L., Alexander, D. C., Feng, J., & Yeo, B. T. T. (2020). Predicting Alzheimer's disease progression using deep recurrent neural networks. *NeuroImage*, *222*, 1–15. https://doi.org/10.1016/j.neuroimage.2020.117203

Ni, Y. C., Tseng, F. P., Pai, M. C., Hsiao, I. T., Lin, K. J., Lin, Z. K., Lin, W. Bin, Chiu, P. Y., Hung, G. U., Chang, C. C., Chang, Y. T., & Chuang, K. (2021). Detection of Alzheimer's disease using ECD SPECT images by transfer learning from FDG PET. *Annals of Nuclear Medicine*, *35*(8), 1–11. https://doi.org/10.1007/s12149-021-01626-3

Noh, J. H., Kim, J. H., & Yang, H. D. (2023). Classification of Alzheimer's Progression Using fMRI Data. Sensors, 23(14), 1–14. https://doi.org/10.3390/s23146330

Oh, K., Chung, Y. C., Kim, K. W., Kim, W. S., & Oh, I. S. (2019). Classification and Visualization of Alzheimer's Disease using Volumetric Convolutional Neural Network and Transfer Learning. *Scientific Reports*, *9*(1), 1–16. https://doi.org/10.1038/s41598-019-54548-6

Pan, D., Zeng, A., Jia, L., Huang, Y., Frizzell, T., & Song, X. (2020). Early detection of alzheimer's disease using magnetic resonance imaging: a novel approach combining convolutional neural networks and ensemble learning. *Frontiers in Neuroscience*, *14*, 1–19. https://doi.org/10.3389/fnins.2020.00259

Panayides, A. S., Amini, A., Filipovic, N. D., Sharma, A., Tsaftaris, S. A., Young, A., ... & Pattichis, C. S. (2020). AI in medical imaging informatics: current challenges and future directions. *IEEE journal of biomedical and health informatics*, *24*(7), 1837-1857. https://ieeexplore.ieee.org/abstract/document/9103969/

Parisot, S., Ktena, S. I., Ferrante, E., Lee, M., Guerrero, R., Glocker, B., & Rueckert, D.

(2018). Disease prediction using graph convolutional networks: Application to autism spectrum disorder and alzheimer's disease. *Medical Image Analysis*, *48*, 117–130. https://doi.org/10.1016/j.media.2018.06.001

Park, C., Ha, J., & Park, S. (2020). Prediction of Alzheimer's disease based on deep neural network by integrating gene expression and DNA methylation dataset. *Expert Systems with Applications*, *140*, 1–10. https://doi.org/10.1016/j.eswa.2019.112873

Parmar, H., Nutter, B., Long, R., Antani, S., & Mitra, S. (2020). Spatiotemporal feature extraction and classification of alzheimer's disease using deep learning 3D-CNN for fMRI data. *Journal of Medical Imaging*, *7*(5), 1–14. https://doi.org/10.1117/1.jmi.7.5.056001

Patil, A. R., & Borkar, G. M. (2023). Node authentication and encrypted data transmission in mobile ad hoc network using the swarm intelligence-based secure ad-hoc on-demand distance vector algorithm. *IET Wireless Sensor Systems*, *13*(6), 201–215. https://doi.org/10.1049/wss2.12068

Penke, B., Szűcs, M., & Bogár, F. (2020). Oligomerization and conformational change turn monomeric β-amyloid and tau proteins toxic: Their role in Alzheimer's pathogenesis. *Molecules*, *25*(7), 1659. http://dx.doi.org/10.3390/molecules25071659

Prabha, C. C., & Sakkarapani, K. (2022). Four Stage Security Algorithm for Data Transfer To Improve Security in Manet. *ICTACT Journal on Communication Technology*, *13*(3), 2731–2736. https://doi.org/10.21917/ijct.2022.0404

Prakash, M., Abdelaziz, M., Zhang, L., Strange, B. A., & Tohka, J. (2021). Quantitative Longitudinal Predictions of Alzheimer's Disease by Multi-Modal Predictive Learning. Journal of Alzheimer's Disease, 79(4), 1533–1546. https://doi.org/10.3233/JAD-200906

Qu, Y., Wang, P., Liu, B., Song, C., Wang, D., Yang, H., Zhang, Z., Chen, P., Kang, X., Du, K., Yao, H., Zhou, B., Han, T., Zuo, N., Han, Y., Lu, J., Yu, C., Zhang, X., Jiang, T., … Liu, Y. (2021). AI4AD: Artificial intelligence analysis for Alzheimer's disease classification based on a multisite DTI database. Brain Disorders, 1, 1–7. https://doi.org/10.1016/j.dscb.2021.100005

Raja Rao, P. B. V., & Yesu Babu, A. (2020). Intellectual routing mechanism for improving QoS in manets for secure data transmission. *International Journal of Scientific and Technology Research*, *9*(3), 3281–3285.

Rani, P., Kavita, Verma, S., Kaur, N., Wozniak, M., Shafi, J., & Ijaz, M. F. (2022). Robust and secure data transmission using artificial intelligence techniques in ad-hoc networks. *Sensors*, *22*(1), 1–22. https://doi.org/10.3390/s22010251

Rashid, M., Singh, H., & Goyal, V. (2020). The use of machine learning and deep learning algorithms in functional magnetic resonance imaging—A systematic review. *Expert Systems*, *37*(6), e12644. https://doi.org/10.1111/exsy.12644

Rodriguez, S., Hug, C., Todorov, P., Moret, N., Boswell, S. A., Evans, K., Zhou, G., Johnson, N. T., Hyman, B. T., Sorger, P. K., Albers, M. W., & Sokolov, A. (2021). Machine learning identifies candidates for drug repurposing in Alzheimer's disease. *Nature Communications*, *12*(1), 1–13. https://doi.org/10.1038/s41467-021-21330-0

Roshanzamir, A., Aghajan, H., & Baghshah, M. S. (2021). Transformer-based deep neural network language models for Alzheimer's disease risk assessment from targeted speech. *BMC Medical Informatics and Decision Making*, *21*(1), 1–14. https://doi.org/10.1186/s12911-021-01456-3

Rossini, P. M., Di Iorio, R., Vecchio, F., Anfossi, M., Babiloni, C., Bozzali, M., ... & Dubois, B. (2020). Early diagnosis of Alzheimer's disease: the role of biomarkers including advanced EEG signal analysis. Report from the IFCN-sponsored panel of experts. *Clinical Neurophysiology*, *131*(6), 1287-1310. https://doi.org/10.1016/j.clinph.2020.03.003

Sadiq, A., Yahya, N., Tang, T. B., Hashim, H., & Naseem, I. (2022). Wavelet-Based Fractal Analysis of rs-fMRI for Classification of Alzheimer's Disease. Sensors, 22(9), 1–21. https://doi.org/10.3390/s22093102

Sahoo, N. K. (2021). Improved Routing and Secure Data Transmission in Mobile Adhoc Networks Using Trust Based Efficient Randomized Multicast Protocol. *Research Journal of Computer Systems and Engineering*, *02*(02), 6–11.

Salehi, A. W., Baglat, P., & Gupta, G. (2020). Alzheimer's disease diagnosis using deep learning techniques. *Int. J. Eng. Adv. Technol*, *9*(3), 874-880. https://doi.org/10.35940/ijeat.C5345.029320

Sangeetha, S., & Sathappan, S. (2023). Reputation based Symmetric Key Authentication for Secure Data Transmission in Mobile Ad Hoc Networks. *EAI Endorsed Transactions on Scalable Information Systems*, *10*(4), 1–10. https://doi.org/10.4108/eetsis.v10i3.1940

Saratxaga, C. L., Moya, I., Picon, A., Acosta, M., Moreno-Fernandez-de-leceta, A., Garrote, E., & Bereciartua-Perez, A. (2021). MRI deep learning-based solution for alzheimer's disease prediction. *Journal of Personalized Medicine*, *11*(9), 1–22. https://doi.org/10.3390/jpm11090902

Saratxaga, C. L., Moya, I., Picón, A., Acosta, M., Moreno-Fernandez-de-Leceta, A., Garrote, E., & Bereciartua-Perez, A. (2021). MRI deep learning-based solution for Alzheimer's disease prediction. *Journal of personalized medicine*, *11*(9), 902. https://doi.org/10.3390/jpm11090902

Sethuraman, S. K., Malaiyappan, N., Ramalingam, R., Basheer, S., Rashid, M., & Ahmad, N. (2023). Predicting Alzheimer's Disease Using Deep Neuro-Functional Networks with Resting-State fMRI. *Electronics (Switzerland)*, *12*(4), 1–19. https://doi.org/10.3390/electronics12041031

Shahbaz, M., Ali, S., Guergachi, A., Niazi, A., & Umer, A. (2019, July). Classification of Alzheimer's Disease using Machine Learning Techniques. In *Data* (pp. 296-303). https://orcid.org/0000-0002-0608-9515

Sharma, C., Kim, S., Nam, Y., Jung, U. J., & Kim, S. R. (2021). Mitochondrial dysfunction as a driver of cognitive impairment in Alzheimer's disease. *International Journal of Molecular Sciences*, *22*(9), 4850. https://doi.org/10.3390/ijms22094850

Shastry, K. A., Vijayakumar, V., V, M. K. M., BA, M., & BN, C. (2022, September). Deep learning techniques for the effective prediction of Alzheimer's disease: a

comprehensive review. In *Healthcare* (Vol. 10, No. 10, p. 1842). MDPI. https://doi.org/10.3390/healthcare10101842

Sheela, M. S., & Suganthi, R. (2024). Secure Routing and Reliable Packets Transmission In MANET Using Fast Recursive Transfer Algorithm. *Babylonian Journal of Networking*, *2024*, 78–87.

Song, X., Mao, M., & Qian, X. (2021). Auto-Metric Graph Neural Network Based on a Meta-Learning Strategy for the Diagnosis of Alzheimer's Disease. IEEE Journal of Biomedical and Health Informatics, 25(8), 3141–3152. https://doi.org/10.1109/JBHI.2021.3053568

Srilakshmi, U., Alghamdi, S. A., Vuyyuru, V. A., Veeraiah, N., & Alotaibi, Y. (2022). A Secure Optimization Routing Algorithm for Mobile Ad Hoc Networks. *IEEE Access*, *10*, 14260–14269. https://doi.org/10.1109/ACCESS.2022.3144679

Srilakshmi, U., Veeraiah, N., Alotaibi, Y., Alghamdi, S. A., Khalaf, O. I., & Subbayamma, B. V. (2021). An improved hybrid secure multipath routing protocol for MANET. *IEEE Access*, *9*, 163043–163053. https://doi.org/10.1109/ACCESS.2021.3133882

Tansey, K. E., Cameron, D., & Hill, M. J. (2018). Genetic risk for Alzheimer's disease is concentrated in specific macrophage and microglial transcriptional networks. *Genome Medicine*, *10*(1), 1–10. https://doi.org/10.1186/s13073-018-0523-8

Tian, J., Smith, G., Guo, H., Liu, B., Pan, Z., Wang, Z., ... & Fang, R. (2021). Modular machine learning for Alzheimer's disease classification from retinal vasculature. *Scientific Reports*, *11*(1), 1-11. https://doi.org/10.1038/s41598-020-80312-2

Trejo-Lopez, J. A., Yachnis, A. T., & Prokop, S. (2023). Neuropathology of Alzheimer's disease. *Neurotherapeutics*, *19*(1), 173-185. https://doi.org/10.1007/s13311-021-01146-y

Tu, J., Tian, D., & Wang, Y. (2021). An Active-Routing Authentication Scheme in MANET. *IEEE Access*, *9*, 34276–34286. https://doi.org/10.1109/ACCESS.2021.3054891

Varesi, A., Carrara, A., Pires, V. G., Floris, V., Pierella, E., Savioli, G., ... & Pascale, A. (2022). Blood-based biomarkers for Alzheimer's disease diagnosis and progression: an overview. *Cells*, *11*(8), 1367. https://doi.org/10.3390/cells11081367

Varoquaux, G., & Cheplygina, V. (2022). Machine learning for medical imaging: methodological failures and recommendations for the future. *NPJ digital medicine*, *5*(1), 48. https://www.nature.com/articles/s41746-022-00592-y

Veeraiah, N., Khalaf, O. I., Prasad, C. V. P. R., Alotaibi, Y., Alsufyani, A., Alghamdi, S. A., & Alsufyani, N. (2021). Trust aware secure energy efficient hybrid protocol for MANET. *IEEE Access*, *9*, 120996–121005. https://doi.org/10.1109/ACCESS.2021.3108807

Venkatasubramanian, S., Dwivedi, J. N., Raja, S., Rajeswari, N., Logeshwaran, J., & Kumar, A. P. (2023). Prediction of Alzheimer's Disease Using DHO-Based Pretrained CNN Model. *Mathematical Problems in Engineering*, *2023*, 1–11. https://doi.org/10.1155/2023/1110500

Wang, H., Bennett, D. A., De Jager, P. L., Zhang, Q. Y., & Zhang, H. Y. (2021). Genome-wide epistasis analysis for Alzheimer's disease and implications for genetic risk prediction. *Alzheimer's Research and Therapy*, *13*(1), 1–13. https://doi.org/10.1186/s13195-021-00794-8

Wang, T., Qiu, R. G., & Yu, M. (2018). Predictive modeling of the progression of alzheimer's disease with recurrent neural networks. *Scientific Reports*, *8*(1), 1–12. https://doi.org/10.1038/s41598-018-27337-w

Willemink, M. J., Koszek, W. A., Hardell, C., Wu, J., Fleischmann, D., Harvey, H., ... & Lungren, M. P. (2020). Preparing medical imaging data for machine learning. *Radiology*, *295*(1), 4-15. https://pubs.rsna.org/doi/abs/10.1148/radiol.2020192224

Xia, Z., Zhou, T., Mamoon, S., & Lu, J. (2021). Recognition of Dementia Biomarkers with Deep Finer-DBN. IEEE Transactions on Neural Systems and Rehabilitation Engineering, 29, 1926–1935. https://doi.org/10.1109/TNSRE.2021.3111989

Xu, L., Liang, G., Liao, C., Chen, G. Den, & Chang, C. C. (2018). An efficient classifier for alzheimer's disease genes identification. *Molecules*, *23*(12), 1–13. https://doi.org/10.3390/molecules23123140

Zhang, J., Zheng, B., Gao, A., Feng, X., Liang, D., & Long, X. (2021). A 3D densely connected convolution neural network with connection-wise attention mechanism for Alzheimer's disease classification. *Magnetic Resonance Imaging*, *78*, 119–126. https://doi.org/10.1016/j.mri.2021.02.001

Zhang, Q., Sidorenko, J., Couvy-Duchesne, B., Marioni, R. E., Wright, M. J., Goate, A. M., Marcora, E., Huang, K. lin, Porter, T., Laws, S. M., Masters, C. L., Bush, A. I., Fowler, C., Darby, D., Pertile, K., Restrepo, C., Roberts, B., Robertson, J., Rumble, R., … Visscher, P. M. (2020). Risk prediction of late-onset Alzheimer's disease implies an oligogenic architecture. *Nature Communications*, *11*(1), 1–11. https://doi.org/10.1038/s41467-020-18534-1

Zhang, Y., Liu, T., Lanfranchi, V., & Yang, P. (2023). Explainable Tensor Multi-Task Ensemble Learning Based on Brain Structure Variation for Alzheimer's Disease Dynamic Prediction. *IEEE Journal of Translational Engineering in Health and Medicine*, *11*, 1–12. https://doi.org/10.1109/JTEHM.2022.3219775

Zhang, Y., Wang, S., Xia, K., Jiang, Y., & Qian, P. (2021). Alzheimer's disease multiclass diagnosis via multimodal neuroimaging embedding feature selection and fusion. *Information Fusion*, *66*, 170–183. https://doi.org/10.1016/j.inffus.2020.09.002

Zhao, Y., Ma, B., Jiang, P., Zeng, D., Wang, X., & Li, S. (2021). Prediction of Alzheimer's Disease Progression with Multi-Information Generative Adversarial Network. *IEEE Journal of Biomedical and Health Informatics*, *25*(3), 1–8. https://doi.org/10.1109/JBHI.2020.3006925

Zhao, Y., Zhao, Y., Durongbhan, P., Chen, L., Liu, J., Billings, S. A., Zis, P., Unwin, Z. C., De Marco, M., Venneri, A., Blackburn, D. J., & Sarrigiannis, P. G. (2020). Imaging of Nonlinear and Dynamic Functional Brain Connectivity Based on EEG Recordings with the Application on the Diagnosis of Alzheimer's Disease. *IEEE Transactions on Medical Imaging*, *39*(5), 1–11. https://doi.org/10.1109/TMI.2019.2953584

Zhao, Z., Li, P., Dai, Y., Min, Z., & Chen, L. (2023). Multi-Task Deep Evidential Sequence Learning for Trustworthy Alzheimer's Disease Progression Prediction. Applied Sciences (Switzerland), 13(15), 1–15. https://doi.org/10.3390/app13158953

Zhou, K., He, W., Xu, Y., Xiong, G., & Cai, J. (2018). Feature selection and transfer learning for alzheimer's disease clinical diagnosis. *Applied Sciences (Switzerland)*, *8*(8), 1–15. https://doi.org/10.3390/app8081372

Zhou, X., Chen, Y., Ip, F. C. F., Jiang, Y., Cao, H., Lv, G., Zhong, H., Chen, J., Ye, T., Chen, Y., Zhang, Y., Ma, S., Lo, R. M. N., Tong, E. P. S., Weiner, M. W., Aisen, P., Petersen, R., Jack, C. R., … Ip, N. Y. (2023). Deep learning-based polygenic risk analysis for Alzheimer's disease prediction. *Communications Medicine*, *3*(1), 1–20. https://doi.org/10.1038/s43856-023-00269-x

Zhu, W., Sun, L., Huang, J., Han, L., & Zhang, D. (2021). Dual Attention Multi-Instance Deep Learning for Alzheimer's Disease Diagnosis with Structural MRI. *IEEE Transactions on Medical Imaging*, *40*(9), 2354–2366. https://doi.org/10.1109/TMI.2021.3077079